HAL
open science

De l'amidon de riz aux cristaux d'amylose : extraction alcaline de l'amidon de riz, propriétés de l'amylose en solution et structure de complexes d'inclusion de l'amylose V

Mateus Cardoso

To cite this version:

Mateus Cardoso. De l'amidon de riz aux cristaux d'amylose : extraction alcaline de l'amidon de riz, propriétés de l'amylose en solution et structure de complexes d'inclusion de l'amylose V. Autre. Université Joseph-Fourier - Grenoble I, 2007. Français. NNT : . tel-00166338

HAL Id: tel-00166338

https://theses.hal.science/tel-00166338v1

Submitted on 3 Aug 2007

HAL is a multi-disciplinary open access archive for the deposit and dissemination of scientific research documents, whether they are published or not. The documents may come from teaching and research institutions in France or abroad, or from public or private research centers.

L'archive ouverte pluridisciplinaire **HAL**, est destinée au dépôt et à la diffusion de documents scientifiques de niveau recherche, publiés ou non, émanant des établissements d'enseignement et de recherche français ou étrangers, des laboratoires publics ou privés.

UNIVERSIDADE FEDERAL DO RIO GRANDE DO SUL, BRÉSIL

ET

UNIVERSITÉ JOSEPH FOURIER – GRENOBLE I, FRANCE

THÈSE

Présentée par

Mateus Borba CARDOSO

Pour obtenir le grade de

DOCTEUR DE L'UNIVERSITÉ JOSEPH FOURIER

(Arrêtés ministériels du 5 Juillet 1984 et du 30 Mars 1992)

FROM RICE STARCH TO AMYLOSE CRYSTALS : ALKALINE EXTRACTION OF RICE STARCH, SOLUTION PROPERTIES OF AMYLOSE AND CRYSTAL STRUCTURE OF V-AMYLOSE INCLUSION COMPLEXES

Soutenue le 25 Avril 2007

Composition du jury :

César Liberato PETZHOLD	président
Nágila RICARDO	rapporteur
Petr STEPANEK	rapporteur
Stéphane GUILBERT	examinateur
Cyrille ROCHAS	examinateur
Nádya DA PESCE SILVEIRA	co-directrice de thèse
Dimitrios SAMIOS	co-directeur de thèse
Jean-Luc PUTAUX	co-directeur de thèse

Instituto de Química (Porto Alegre, Brésil)
Centre de Recherches sur les Macromolécules Végétales - CNRS (Grenoble)

ACKNOWLEDGMENTS

To God for the protection and force.

To my wife, Janaina, for the constant incentive, affection, love and inspiration.

To my parents, brother, sister and grandmother for the support and effort for the concretization of this project.

To Prof. Dr. Nádya Pesce da Silveira for the orientation, friendship and dedication in all moments.

To Dr. Jean-Luc Putaux for the reception in his laboratory, teachings and untiring support during the development of this work.

To Prof. Dr. Dimitrios Samios for the encouragement and opportunity in his workgroup.

To Dr. Henri Chanzy for the support and scientific example.

To Dr. Karim Mazeau for the modeling teaching.

To Dr. Yoshi Nishiyama for the syncrothoron measurements, crystallographic teaching and friendship.

To Daniele Dupeyre for the friendship and SEM teaching.

To Prof. Dr. Fabiano Rodembusch and Prof. Dr. Valter Stefani for the fluorescence teaching and measurements.

To Prof. Dr. Célia Carlini and Fernanda Stanisçuaski for the gel filtration chromatography assintance.

To Juliana Santos, Manuela Jaeger and Manuela Heineck for the experiments assistance.

To all my fellows of *LINDIM* for the friendship.

To my fellows of *Structure et propriétés des glycomatériaux* group for the excellent reception and principally to Elsa Lasseuguette, Aurélie Rattaz and Sophie Berlioz (*bureau 118*) for the help during my stay in France.

To Dr. Michelle de Souza for the untiring help in the translations of French documents.

To LNLS for the SAXS measurements.

To Phil Pattison for his help with the data acquisition at ESRF.

To Cooperativa Arrozeira Extremo Sul for the rice samples.

To the organizers of the first French-Brazilian Meeting on Polymers *(FBPOL 2005)*.

To CAPES and CNPq for the financial support.

To everybody who has contributed in some way for the development of this work.

TABLE OF CONTENT

FIGURE INDEX....3
TABLE INDEX....5
ANNEX INDEX....7
RÉSUMÉ....9
ABSTRACT....10
RESUMO....11

CHAPTER 1 - INTRODUCTION....13
INTRODUCTION (fr)....15
INTRODUCTION (gb)....17
INTRODUÇÃO....19

CHAPTER 2 - BIBLIOGRAPHIC REVIEW....21
2.1. Amylose....24
2.2. Amylopectin....27
2.3. Crystal structure....29
2.4. The alternating ultrastructure of starch....30
2.5. Macromolecular orientation....32
2.6. Thermal properties....33
2.7. Alkaline extraction of Brazilian rice starch....35
2.8. V-amylose crystals....36

CHAPTER 3 - MATERIALS AND METHODS....41
3.1. Starch isolation....43
3.1.1. Protein detection....43
3.1.1.1. Intrinsic fluorescence spectroscopy....43
3.1.1.2. Biuret colorimetric test....44
3.1.1.3. UV/Vis....44
3.1.1.4. General procedure for protein labelling using pyrene molecule (Py)....44
3.1.1.5. General procedure for protein labelling using isothiocyanate benzoxazole dye....45
3.1.2. Morphology and structure of starch granules....45
3.1.2.1. Wide-angle X-ray diffraction (WAXS)....45
3.1.2.2. Differential scanning calorimetry (DSC)....46
3.1.2.3. Scanning electron microscopy (SEM)....46
3.1.2.4. Small-angle X-ray scattering (SAXS)....46
3.1.2.5. Optical microscopy....47
3.1.2.6. Mie scattering....47
3.2. Light scattering of aqueous amylose solutions....47
3.2.1. Amylose extraction....47
3.2.2. Light scattering....48
3.3. V amylose single crystals....50
3.3.1. Preparation of the crystals....50
3.3.1.1. Visopropanol crystals....50
3.3.1.2. Vα-naphthol crystals....50
3.3.1.3. Density measurement....51

3.3.2. Transmission electron microscopy 51
3.3.2.1. Conventional imaging and electron diffraction 51
3.3.2.2. High resolution electron microscopy 52
3.3.3. Synchrotron X-ray diffraction 52
3.3.4. Molecular modeling 53
3.3.4.1. Conformational parameters 53
3.3.4.2. Model energy calculation 54
3.3.4.3. Molecular dynamics 54
3.3.4.4. Hydrogen bonds 55
3.3.4.5. Connolly surface area and accessibility of functional groups 55
3.3.4.6. Theoretical electron diffraction pattern 55
3.3.4.7. Model refinement 55

CHAPTER 4 - ALKALINE EXTRACTION OF BRAZILIAN RICE STARCH 57
4.1. Protein removal 59
4.2. Morphology and structure of starch granules 67
4.3. Morphological and structural analyses during the alkaline starch extraction 72
4.3.1. The ultrastructure of starch during the extraction 72
4.3.2. The morphology of supercritically dried treated starch 75

CHAPTER 5 - LIGHT SCATTERING OF AQUEOUS AMYLOSE SOLUTIONS 79

CHAPTER 6 - V AMYLOSE SINGLE CRYSTALS 93
6.1. Visopropanol crystals 95
6.2. V amylose / α-naphthol crystals 98
6.2.1. Morphology, unit cell dimensions and symmetry 98
6.2.2. Molecular lattice image 103
6.2.3. Molecular model 106
6.2.3.1. Generation and conformations of helical amylose chains 106
6.2.3.2. Packing of the helices 109
6.2.3.3. Addition of α-naphthol 112
6.2.3.4. Simulation of diffraction data 117
6.2.3.5. NPT molecular dynamics 120
6.2.3.6. Refinement of crystal structure 120
6.3. Discussion 123

CHAPTER 7 - CONCLUSION AND PERSPECTIVES 129

REFERENCES 135

ANNEXES 1-7 145
ANNEX 8 – SCIENTIFIC PRODUCTION 159

FIGURE INDEX

Figure 1. Scanning electron micrographs of starch granules from different origins 23
Figure 2. Chemical structure of amylose.....24
Figure 3. Chemical structure of amylopectin 27
Figure 4. Scheme of the clustered architecture of amylopectin 29
Figure 5. Projection of the crystal packing of double helices in A-type and B-type unit cells 30
Figure 6. TEM image of a ultra-thin section of a waxy maize starch granule after 7 days of HCl hydrolysis 31
Figure 7. Scheme of the cluster model of amylopectin in the starch supramolecular architecture.....32
Figure 8. Polarized light optical micrograph of native potato starch granules in excess water. 33
Figure 9. V-amylose single crystals and their corresponding electron diffraction 39
Figure 10. Schematic drawing of the structural segment of the amylose chain along with the nomenclature of selected atoms 54
Figure 11. Fluorescence spectra of the supernatants obtained after treatment 3 59
Figure 12. Multi-peak-fit of the fluorescence emission spectrum of supernatant 8 60
Figure 13. Biuret test of the protein solutions.....61
Figure 14. UV-vis spectra of the supernatant samples.....62
Figure 15. A set of fluorescence spectra of the supernatants registered by using pyrene (Py) as a fluorescent probe 64
Figure 16. Fluorescence emission spectra of the organic layers obtained from solution 8. 64
Figure 17. Fluorescence emission spectra of the solutions 1-3.....66
Figure 18. Fluorescence emission spectra of the fractions 4-8 67
Figure 19. Scanning electron microscopy images of starches obtained after different alkaline treatments 68
Figure 20. X-ray diffraction patterns of starch slurries.....69
Figure 21. Differential scanning calorimetry patterns of starch slurries 70
Figure 22. Small-angle X-ray scattering profiles of the slurry starches obtained during the steps 2, 4, 6 and 8 at treatment 5.....73
Figure 23. Polarized light and non-polarized light micrographs of the slurry starches obtained in steps 2, 4, 6 and 8 74
Figure 24. Scanning electron microscopy of supercritically dried rice starch granules 76
Figure 25. Size distribution of rice starch obtained by Mie scattering.....77
Figure 26. Autocorrelation functions obtaind from fraction *f*11, at 25°C in different angles.....81
Figure 27. Rh as a function of θ for amylose obtained in the *f*11 fraction during the gel filtration chromatography 82
Figure 28. Relaxation mode (Γ) as a function of the scattering vector (q^2).....83
Figure 29. Plot of dissymmetry d(θ) vs. cos θ for the *f*11 fraction 83
Figure 30. Relationship between apparent gyration radius, elution volume and molecular weight of rice starch amylose 84

Figure 31. Influence of the KOH concentration in the R_h and R_g values of amylose solutions stored for different times 85
Figure 32. Influence of the KCl concetration in the R_h and R_g values of amylose chains stored for different times 87
Figure 33. Benedict's test performed to verify the existence of glucose presence 89
Figure 34. TEM images of lamellar single crystals of V-amylose complexed with isopropanol 96
Figure 35. TEM image of lamellar single crystals of V-amylose complexed with linalool 97
Figure 36. TEM image of a Visopropanol single crystal; corresponding base plane electron diffraction pattern correctly oriented with respect to the crystal and indexation of the pattern 98
Figure 37. Lamellar single crystals of V-amylose complexed with α-naphthol 99
Figure 38. Vα-naphthol single crystal; corresponding base plane electron diffraction pattern correctly oriented with respect to the crystal and indexation of the pattern 100
Figure 39. Electron diffraction patterns recorded on Vα-naphthol crystals rotated by ±26° and ±36° around *a**; diffraction diagrams recorded on crystals rotated by ±40° and ±47° around *a**+*b** 101
Figure 40. Synchrotron X-ray diffraction fiber diagrams recorded on mats of sedimented Vα-naphthol crystals and X-ray diffraction pattern after background subtraction and re-mapping into cylindrical reciprocal space 102
Figure 41. HREM image of a Vα-naphthol crystal viewed along the chain axis *c*; power spectrum of the lattice image; real-space translational average and 4-fold rotation average of the image 104
Figure 42. Canonical orientations of the hydroxymethyl groups of glucose. 106
Figure 43. Molecular drawings of the six helices models 108
Figure 44. Details of the atomic structure of the optimized isolated L_1 helix onto which are superimposed the hydrogen bonds, displayed as dashed lines 109
Figure 45. Plot of calculated energy and rotation angle for the L_1 and R_1 helices 110
Figure 46. Characteristics of L_1 structure: complementary shapes of two interacting helices and molecular model evidenced the dimerization of the chains 113
Figure 47. Variation of the van de Walls energy with the number of α-naphthol molecules inserted in and in between helices 114
Figure 48. Molecular projections of the L_1 model 116
Figure 49. Simulated and experimental electron diffraction patterns of the L_2 crystal structure 116
Figure 50. Molecular projections of the V-amylose/α-naphthol inclusion complex refined using the SHELX program 121
Figure 51. Longitudinal view showing the a-naphthol molecules located inside the helix .. 121
Figure 52. Experimental and simulated diffraction electron pattern obtained from refined model by SHELX program 122
Figure 53. Refined model superimposed in the real-space averaged lattice image of the crystal 123

TABLE INDEX

Table 1. Fluorescent supernatant peak area obtained by multi-peak fitting for different treatments 60
Table 2. Results from the biuret colorimetric test 61
Table 3. UV-vis and fluorescence results for the protein presence in different steps of the alkaline extraction using NaOH solution at 0,24% w/v 63
Table 4. DSC parameters obtained for the starches extracted with different NaOH concentrations 71
Table 5. R_g, R_h, ρ, and M_w for the amylose fractions 82
Table 6. ρ factor at different storage times in KOH solutions 86
Table 7. ρ factor at different storage times in KCl solutions 88
Table 8. Characteristics of optimized helices in isolation 108
Table 9. Characteristics of optimized helices in the packing 111
Table 10. Conformational parameters of the right and left-handed helices minimized in the packing 113
Table 11. Characteristics of minimized amylose/α-naphthol systems 115
Table 12. Symmetry factor for each I_{hk} group as well as the *gsf* values for the simulated diffraction patterns 118

ANNEXES

Annex 1. d-spacings corresponding to *hk*0 reflections from electron diffraction patterns recorded at room temperature on untilted Visopropanol single crystals. The experimental *d*-spacings (d_{obs}) are compared with the values (d_{cal}) calculated from the parameters of the refined unit cell 145

Annex 2. d-spacings corresponding to *hkl* reflections from electron diffraction patterns recorded at room temperature on Vα-naphthol single crystals. The experimental *d*-spacings (d_{obs}) are compared with the values (d_{cal}) calculated from the parameters of the refined unit cell 147

Annex 3. d-spacings corresponding to *hkl* reflections from in synchrotron X-ray diffraction diagrams recorded on dry mats of Vα-naphthol crystals. The experimental *d*-spacings (d_{obs}) are compared with the values (d_{cal}) calculated from the parameters of the refined unit cell 149

Annex 4. Conformational parameters of the isolated right and left-handed helices. Angles are expressed in °, puckering amplitudes in Å 151

Annex 5. Experimental (exp) and simulated diffracted intensities (L_1, L_2, L_3, R_1, R_2 and R_3 models). The spots were represented in according to their relative intensities: absent (-), weak (W), medium (M) and strong (S). The total number of spots in accordance between experimental and simulated diffracted intensities are given in the last line as agreement 153

Annex 6. Cell parameters, stress tensor components, final energy and density of initial (ini) and optimized (opt) helices in NVT molecular dinamics. 155

Annex 7. List of experimental normalized intensity averages measured from *hk*0 reflections in electron diffraction patterns recorded at room temperature on untilted Vα-naphthol single crystals 157

Annex 8. Scientific production 159

RÉSUMÉ

Durant ce travail, nous avons étudié l'extraction alcaline de l'amidon de riz brésilien, le comportement hydrodynamique de l'amylose en solution ainsi que la formation et la structure cristalline de complexes d'inclusion d'amylose V. L'efficacité dans la déprotéinisation pendant l'extraction alcaline a été évaluée en utilisant le test de Biuret ainsi que les spectroscopies UV-Vis et de fluorescence. En parallèle, les modifications morphologiques des granules d'amidon et leur gélatinisation alcaline ont été étudiées. L'évolution de la cristallinité a été suivie afin de comprendre l'effet de la soude sur l'ultrastructure des grains d'amidon. Des tentatives de séparation et de purification de l'amylose de riz brésilien par précipitation avec le thymol ont été faites. L'échantillon obtenu a été fractionné par chromatographie de filtration sur gel et analysé par diffusion de la lumière. En outre, de l'amylose commerciale a été étudiée en solution aqueuse en fonction du temps de stockage et de la force ionique. Des cristaux lamellaires d'amylose V ont été préparés par addition de complexants à des solutions métastables diluées d'amylose synthétique. La morphologie et la structure des cristaux ont été étudiées par microscopie électronique en transmission et diffraction des électrons et des rayons X. La structure cristalline du complexe de l'amylose V avec l'α-naphthol a été étudiée en détail par modélisation moléculaire. Le modèle conduisant au meilleur facteur d'accord est constitué d'un réseau tétragonal de simples hélices gauches d'ordre 8, empilée de manière anti-parallèle. Des molécules d'α-naphthol sont incluses dans la maille cristalline, à la fois dans et entre les hélices.

ABSTRACT

The main purposes of the present work were to follow the alkaline extraction of a Brazilian rice starch, to study the hydrodynamic behavior of amylose, a biopolymer extracted from starch, and to study the crystallization and molecular modeling of V-amylose crystals. The efficiency of the deproteinization by the alkaline treatment was evaluated using the biuret test as well as UV-vis and fluorescence spectroscopy. In parallel, the morphological changes in starch granules and their alkaline gelatinization were studied. The crystallinity and ultrastructure of starch were monitored in order to understand the effect of alkali on the ultrastructure of starch granules. Amylose was isolated from Brazilian rice starch by dissolution and reprecipitation with thymol. The isolated product was fractionated by gel filtration chromatography and analyzed using light scattering. In addition, commercial amylose was studied in aqueous solutions as a function of storage time and ionic strength. Lamellar crystals of V-amylose were obtained by adding guest molecules to metastable dilute aqueous solutions of synthetic amylose. The morphology and structure of the crystals were studied using transmission electron microscopy as well as electron and X-ray diffraction. The crystal structure of the inclusion complex of V-amylose with α-naphthol was investigated in detail using molecular modeling. The model exhibiting the lowest reliability factor was described by a tetragonal lattice of antiparallel 8-fold left-handed single helices. Molecules of α-naphthol are included in the crystal lattice, both inside and in-between helices.

RESUMO

O objetivo principal do presente trabalho foi estudar a extração alcalina do amido brasileiro, o comportamento hidrodinâmico da amilose, um biopolímero extraído do amido, e a cristalização e modelagem molecular dos cristais de V amilose. A eficiência na desproteinização durante a extração alcalina foi avaliada usando o teste de biureto bem como as espectroscopias de UV-Vis e fluorescência. Em paralelo, as alterações morfológicas dos grânulos de amido e sua gelatinização alcalina foram estudadas. A cristalinidade e a ultra-estrutura do amido foram monitoradas a fim de compreender o efeito do álcali na ultra-estrutura dos grânulos. A amilose foi isolada a partir do arroz brasileiro por dissolução e reprecipitação com timol. A amostra isolada foi fracionada por cromatografia de filtração em gel e analisada por espalhamento de luz. Além disso, amilose comercial foi estudada em solução aquosa em diferentes tempos de armazenamento bem como em diferentes forças iônicas. Cristais lamelares de V amilose foram obtidos pela adição de um complexante a soluções metaestáveis diluídas de amilose sintética. A morfologia e a estrutura dos cristais foram estudadas utilizando microscopia eletrônica de transmissão e difração de raios-X. Os detalhes da estrutura cristalina do complexo V$_{\alpha\text{-naphthol}}$ foram investigados por meio de modelagem molecular. O modelo exibindo o melhor fator de acordo, entre os dados experimentais e simulados, foi obtido a partir de uma estrutura tetragonal contendo hélices esquerdas simples com oito resíduos de glicose por volta de hélice. As moléculas de α-naftol foram localizadas na estrutura cristalina dentro e entre as hélices.

CHAPTER 1

INTRODUCTION

On trouve l'amidon sous forme de grains semi-cristallins principalement composés de deux homopolymères d'α-D-glucose : l'amylose et l'amylopectine. L'amylose est un polymère linéaire dans lequel les unités glucosyles sont reliées par des liaisons α(1,4). L'amylopectine est une macromolécule ramifiée dont les segments linéaires sont reliés par des liaisons α(1,6). Un grand nombre de produits à base d'amidon sont utilisés comme ingrédients dans l'industrie agro-alimentaire. Certains d'entre eux ont été développés pour retenir de l'eau, former des gels visqueux ou apporter certaines qualités texturales. L'utilisation de l'amidon comme additif dans les aliments a stimulé le développement de différentes techniques d'extraction, afin de proposer des produits de haute pureté et avec des propriétés physico-chimiques bien définies. Dans ce contexte, des avancées importantes ont été faites durant les dernières décennies dans les protocoles d'extraction de l'amidon. La méthode alcaline est largement employée, bien que ce traitement puisse modifier la structure des grains d'amidon.

La cristallisation de l'amylose sous la forme V (simples hélices) constitue un important sujet d'intérêt. Il existe en effet de nombreux complexes de l'amylose avec une grande variété de molécules organiques et inorganiques, permettant d'envisager des applications dans le domaine pharmaceutique ou phyto-sanitaire car les molécules emprisonnées dans les complexes peuvent être relarguées. Les complexes d'inclusion cristallins produisent des clichés de fibres bien résolus par diffraction des rayons X. En travaillant à partir de solutions diluées, on peut préparer des monocristaux lamellaires qui produisent des clichés de diffraction électroniques ponctuels. Quelques modèles structuraux ont été proposés mais plusieurs questions restent encore sans réponse relatifs, en particulier, à l'hélicité de l'amylose V, au nombre d'unités glucose par tour et à la localisation des molécules complexantes dans la maille cristalline.

Dans la première partie de ce mémoire, nous étudierons l'influence de la concentration de la soude dans les traitements d'extraction des protéines et de purification de l'amidon de riz brésilien. La quantité de protéines résiduelles au cours du traitement a été

déterminée en utilisant le test de Biuret ainsi que les spectroscopies UV-Vis et de fluorescence. La morphologie des grains d'amidons au cours du traitement alcalin a été étudiée au moyen d'observations par microscopie électronique à balayage. L'évolution de leur cristallinité a été évaluée par diffraction des rayons X aux grands angles et la calorimétrie à balayage différentiel. Nous avons employé la diffusion des rayons X aux petits angles pour étudier l'action de la soude sur l'organisation lamellaire semi-cristalline des grains d'amidon. Enfin, des informations complémentaires ont été obtenues en observant les variations de biréfringence des grains d'amidon par microscopie optique en lumière polarisée pendant l'extraction des protéines.

Dans une seconde partie, nous aborderons les aspects de conformation des chaînes d'amylose en solution aqueuse. Nous avons étudié leur comportement hydrodynamique en fonction du temps de stockage des solutions et de la force ionique du milieu apr diffusion dynamique de la lumière. Les données ont été complétées par celles obtenues par diffusion statique de la lumière permettant, ce qui a permis de déterminer le rayon de giration des molécules.

Enfin, dans la troisième partie, nous décrirons la préparation des complexes d'inclusion cristallins de l'amylose V, en particulier ceux préparés avec l'isopropanol et l'α-naphthol. Ils ont été caractérisé en utilisant conjointement la diffraction des électrons et des rayons X et l'imagerie électronique moléculaire à haute résolution. A partir du jeu de données recueilli, nous avons proposé un modèle de la structure cristalline du complexe $V_{\alpha\text{-naphthol}}$ établi par analyse conformationelle et modélisation moléculaire.

Starch occurs as semicrystalline granules mainly composed of two homopolymers of α-D-glucose, namely amylose and amylopectin. Amylose is a mostly linear polymer where α-D-glycosyl units are connected by α(1,4) glycosidic linkages. Amylopectin is a branched macromolecule containing α(1,4)-linked linear segments connected by α(1,6) branching points. A wide range of starchy products are used as ingredients in processed foods. Some of them have been developed to take up water and produce viscous fluids, pastes and gels with desired textural quality. The utilization of starch as additive in the food industry has stimulated the development of different extraction methodologies with the purpose of isolating products with a high purity and well-defined physical properties. In this context, important advances have been made during the last decades in the development of methods for starch isolation. The alkaline method has commonly been used to extract starch, in spite of the fact that this treatment can alter the structure of starch granules.

An important topic in the amylose organization concerns the structure of V-amylose crystals. These complexes take their origin in the remarkable number of inorganic and organic guests that are susceptible to become associated with amylose helices. The study of these complexes presents a great interest for pharmacology and in the food industry since the trapped guest molecules can be released later. Crystalline V-amylose complexes yield well-resolved X-ray fiber diffraction diagrams and when crystallized from dilute solutions, can form remarkable lamellar single crystals producing sharp electron diffractions. Structural models have been proposed but a large number of details remain unsolved. In particular, the handedness, the number of glucose molecules per turn of helix and the location of the guest molecules in the crystal are still to be unambiguously determined.

In the first part of present work, we have studied the influence of NaOH concentration on protein removal and degradation of starch granules during the alkaline extraction. On the one hand, we monitored the variation in protein content during the extraction procedure using the classical biuret test, UV-vis and fluorescence spectroscopy. The morphology of starch granules was observed using scanning electron microscopy (SEM)

and structural changes were followed by wide-angle X-ray scattering (WAXS) and differential scanning calorimetry (DSC). Small angle X-ray scattering (SAXS) was applied to invesitigate the influence of the alkali on the semi-crystalline lamellar organization in starch granules during protein extraction. Finally, the birefringence of the starch granules was observed by optical microscopy and has been used as a complement to the SAXS data.

In a second part, efforts have been devoted to investigate the amylose as a random coil in aqueous solutions. The dynamical behavior of the chains as a function of the ionic strength as the storage time was followed by dynamic light scattering (DLS). The data were complemented by static light scattering (SLS) to measure the radius of gyration.

In a third section, we describe the preparation of V-amylose crystalline inclusion compounds, in particular with isopropanol and α-naphthol, and their characterization using the diffraction techniques. A three-dimensional electron diffraction analysis was performed and a good set of diffraction data was collected from the Vα-naphthol crystals. A modeling study was performed in order to solve the molecular structure of the complex and the results were confronted with high resolution electron microscopy (HREM) lattice images.

O amido é um grânulo semi-cristalino composto basicamente por dois homopolímeros de α-D-glicose, chamados de amilose e amilopectina. A amilose é um polímero linear em que as unidades de α-D-glicose são conectadas através de ligações glicosídicas α(1,4). A amilopectina é uma macromolécula ramificada contendo segmentos lineares, ligados através de ligações glicosídicas α(1,4) e pontos de ramificações através de ligações α(1,6). Uma grande gama de produtos originados do amido são usados como ingredientes em alimentos processados. Alguns deles têm sido desenvolvidos para reter água e produzir fluidos viscosos, massas e géis com a qualidade de textura desejada. A utilização do amido como aditivo na indústria de alimentos tem estimulado o desenvolvimento de diferentes metodologias de extração com a proposta de isolar produtos com alta pureza e propriedades físico-químicas bem definidas. Neste contexto, avanços importantes têm sido feitos durante as últimas décadas no desenvolvimento de métodos de isolamento de amido. O método alcalino tem sido comumente utilizado, apesar desse tratamento poder alterar a estrutura dos grânulos de amido.

A cristalização da amilose sob a forma V (hélices simples) constitui um importante centro de interesse. Existe de fato, numerosos complexos de amilose com uma grande variedade de moléculas orgânicas e inorgânicas, permitindo aplicações na área farmacêutica e/ou fitossanitária, já que esses complexos podem ser utilizados na liberação controlada das moléculas aprisionadas. Os complexos cristalinos de V amilose produzem espectros de raios-X de fibra bem resolvidos e, quando cristalizados a partir de soluções diluídas podem formar cristais lamelares, produzindo difrações eletrônicas pontuais. Modelos estruturais têm sido propostos, mas um grande número de detalhes permanecem desconhecidos. Em particular, não é clara a helicidade, o número de moléculas de glicose por cada volta da hélice e se os complexos são ligados na cavidade da amilose, entre as hélices ou em ambas.

Na primeira parte do trabalho, estudo-se a influência da concentração de NaOH na remoção das proteínas e a degradação dos grânulos de amido durante a extração

alcalina. Nesse sentido, monitorou-se a variação do conteúdo de proteína durante o procedimento de extração, usando o teste clássico de biureto e as espectroscopias de UV-Vis e fluorescência. A morfologia dos grânulos de amido foi observada utilizando microscopia eletrônica de varredura e mudanças estruturais foram investigadas por espalhamento de raios-X a altos ângulos e calorimetria de varredura diferencial. Espalhamento de raios-X a baixos ângulos foi aplicado a fim de explorar a ação alcalina sobre a organização lamelar semi-cristalina dos grânulos de amido durante a extração das proteínas. Finalmente, a birrefringência dos grânulos de amido foi observada através de microscopia óptica e foi usada para complementar os dados de espalhamento de raios-X a baixos ângulos.

Na segunda parte, esforços foram feitos para investigar a amilose como um novelo aleatório em soluções aquosas. O comportamento hidrodinâmico das cadeias, como uma função da força iônica e do tempo de armazenamento, foi estudado por espectroscopia de correlação de fótons. Os dados foram complementados por espalhamento de luz estático, onde o raio de giro foi medido.

Na terceira seção, descrevemos a preparação dos compostos de inclusão cristalinos de V amilose, em particular com isopropanol e α-naftol, e sua caracterização, a partir das técnicas de difração. Uma análise de difração eletrônica tridimensional foi realizada bem como imagens de microscopia eletrônica de alta resolução levando a uma coleção de dados cristalinos dos cristais de $V_{\alpha\text{-naftol}}$. Um estudo de modelização foi feito com o objetivo de resolver a estrutura do complexo e os resultados foram confrontados com as imagens de microscopia eletrônica de alta resolução.

CHAPTER 2

BIBLIOGRAPHIC REVIEW

Starch is a carbohydrate which is insoluble in water and is used by plants as a way to store the excess of glucose. Starch occurs as semicrystalline granules mainly composed of two homopolymers of α-D-glucose, namely amylose and amylopectin. The native granules have a size typically ranging from 1 to 100 μm and a shape that may significantly vary depending on the botanical origin (**Figure 1**).

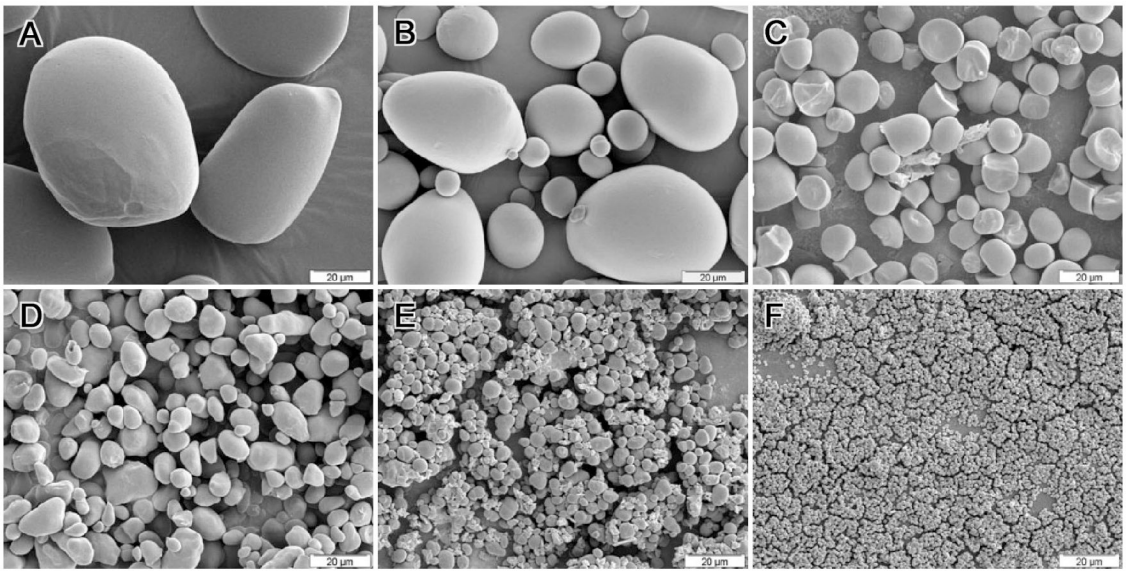

Figure 1. Scanning electron micrographs of starch granules from different origins.
A: *Canna edulis* ; B: potato ; C: pinhão ; D: chestnut ; E: cocoa ;
F: quinoa. (images: D. Dupeyre, CERMAV, Grenoble, France)

Starch is the main source of carbohydrates in the human diets. It is supplied by traditional foods such as cereals, roots and tubers. Among carbohydrate polymers, starch is currently enjoying increased attention owing to its usefulness in different products. Starch greatly contributes to the textural properties of many foods and is widely used in industrial applications as a thickener, colloidal stabilizer, gelling and water retention agent. The physico-chemical properties and functional characteristics of starch systems and their uniqueness in various products vary with starch botanical origin (**Svegmark and Hermansson, 1993**).

2.1. Amylose

Amylose (**Figure 2**) is a mostly linear molecule of α(1→4)-linked D-glucopyranosyl units, containing about 1% of α(1→6) branching points (**Takeda et al., 1987**). The linearity was deduced from the susceptibility of the amylose molecule to complete hydrolysis by β-amylase. This enzyme cleaves the α(1→4) bonds from the non-reducing end and cannot cut the α(1→6) bonds. If degraded by pure β-amylase, the linear amylose is completely transformed into maltose.

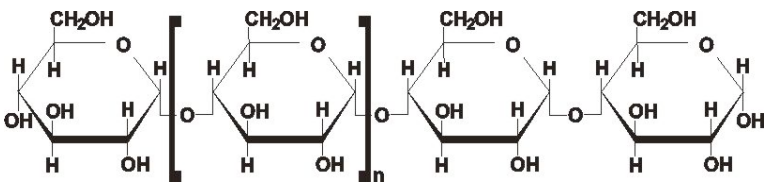

Figure 2. Chemical structure of amylose.

Takeda et al. (**1987**) performed an extensive study of the fine structure of amylose based upon the successive use of β-amylase and isoamylase. Currently, no effective methods for the separation of linear and branched amyloses are known, so all results concerning amylose branching have been obtained by assuming the existence of two quite distinct populations, one strictly linear and the second one characterized by a 40% β-amylolysis limit (**Takeda et al., 1987**). Thus, the branching linkages are often located near the reducing end and/or are due to the existence of multiply branched side chains.

Normally, the amount of branched molecules lies between 25 to 55% on a molecular basis (**Takeda et al., 1987**). The level of branching is continuously increased as a function of molecular weight when fractionated amylose is used (**Banks and Greenwood, 1975**). Hizukuri et al. (**1997**) found an average of 2 to 8 branching points in each amylose molecule, with side chains containing from 4 to over 100 glucosyl units. In this way, the further fractionation of β-limit dextrins shows that the branched amylose contains some clusters of short chains.

Another important molecular parameter is the volume occupied by the polymer in solution. A way to represent this volume is the radius of gyration, R_g, which depends on the molecular weight (M_W). The molecular weight dependence of R_g can be described by the power law, $R_i \sim M_i^n$, where the exponent n is similar to Mark-Houwink coefficient, and M_i and R_i are the molecular weight and the radius of the component i, respectively.

Nowadays, the combined use of high-performance size exclusion chromatography (HPSEC) with a light scattering detector leads to $R_i \sim M_i^n$ relations for the fractionated molecules M_i. Thus, it is possible to determine up to which point amylose chains in solution behave differently from strictly linear chains. Roger and Colonna (**1996**) extracted amylose fractions by aqueous leaching of corn starch granules using 5°C steps over a temperature range of 65-95°C and applied the combined use of HPSEC and light scattering. The dependence of molecular weight on macromolecular size was consistent with the behavior of expanded chains in good solvent. Indeed, the hydrodynamic coefficient n was estimated to lie between 0.6 and 0.7 for the $R_g \sim M^n$ relation, suggesting therefore an extended linear random coil in a large range of M_W ($3x10^5$-$9x10^6$ g/mol). However, the presence of branches does not significantly alter the solution behavior of amylose which behaves like a linear chain (**Buléon et al., 1998**).

Measurements of M_W distribution and $\overline{M_w}$ have been performed on a large number of starch samples of different botanical origins. Whereas proteins are coded, polysaccharides occur with a molecular weight distribution. This distribution is usually represented by number, weight or z-average molecular weight ($\overline{M_n}$, $\overline{M_w}$ and $\overline{M_z}$, respectively). Discrepancies are observed in the literature due to the biological origin of amylose and the molecular degradation occurring during amylose fractionation (**Ong et al., 1994**). Intrinsic viscosity remains a basic technique to calculate the viscosity-average molecular weight ($\overline{M_v}$), using the Mark–Houwink coefficients measured in different solvents (**Foster and Hixon, 1944**). As expected, the polydispersity depends of botanical origin and

also on extraction procedures (**Ring et al., 1985**). The molecular size of the branched molecules is 1.5-3.0 times larger than those of linear molecules. However, no significant differences are observed between average molecular size of cereal amylose.

Nowadays, amylose solutions can be easily characterized by size-exclusion chromatography coupled to on-line multi-angle laser light scattering (SEC-MALLS). However, the hydrodynamic difference between amylose and amylopectin does not allow to clearly discriminate both components (**Ring et al., 1985; Bello-Perez et al.,1996**). Due to a difficult dissolution and a strong aggregation tendency in water, other solvents were used to dissolve amylose (dimethyl sulfoxide-DMSO, aqueous alkaline solution, acidic conditions or DMAc/LiCl; **Buléon et al., 1998**).

Amylose fractionation has been reported to be an efficient and reproducible method (**Yu and Rollings, 1987; Yu and Rollings, 1988; Roger and Colonna, 1992; Fishman and Hoagland, 1994; Roger and Colonna, 1996; Bello-Perez et al., 1998a**) using a specific optimization algorithm. The experimental molecular weight distribution (MWD) measured by SEC–MALLS can be fitted with mathematical functions and described as 'normal', ‘most probable’ and ‘log–normal’ distributions. Good agreements were obtained using either a sum of overlapping Gaussian curves (**Fishman and Hoagland, 1994**) or a ‘most probable’ model (**Roger and Colonna, 1996**).

The flexibility of polymeric chains is the basis of the dimensionless quantity C_∞ (the characteristic ratio), that is defined as the ratio between the dimensions of real and freely joined chains. An important characteristic is the persistence length *a*, defined as the average projection of an infinitely long chain on the initial tangent of the chain. Amylose chains in aqueous solution have *a*=1.71 nm and are more flexible than modified cellulose (*a*=4.8-7.2 nm for cellulose diacetate; *a*=8.0-12.0 nm for carboxymethyl cellulose), but similar to pullulan solutions (*a*=1.2-1.9 nm; **Roger and Colonna, 1996**). Therefore, all these polysaccharides belong to the class of loosely joined polysaccharides, in contrast to stiff polysaccharides such as xanthan (*a*=310±40 nm) and scleroglucan (*a*= 180±30 nm) (**Yalpani, 1988**). Thus, this conformational feature explains why amylose presents a low

intrinsic viscosity compared to other polysaccharides. Another specific feature of interest is the ability of amylose to bind iodine. The existence of I_3^- and I_5^- was checked using Raman spectral measurements and UV-Vis, coupled with theoretical analyses. Yu et al. (**1996**) have shown that the four dominant polyiodide chains which coexist are longer species such as I_9^{3-}, I_{11}^{3-} , I_{13}^{3-} and I_{15}^{3-}.

2.2. Amylopectin

Amylopectin is the major branched component of starch. It is composed of α(1→4)-linked glucopyranosyl residues linked together mainly by linkages but with 5–6% of (1→6) bonds at the branch points (**Figure 3**).

Significant information is provided by chain distributions profiles. The debranching enzymes, isoamylase and pullulanase, specifically hydrolyze the branch linkages and produce the short linear chains. SEC (**Hizukuri, 1985; Hizukuri, 1986**) and high-performance anion-exchange chromatography with pulsed amperometric detection (**Hizukuri, 1986; Hanashiro et al., 1996; Wong and Jane, 1997**) are the two basic techniques used to estimate the chain length distributions.

Amylopectin is divided in three types of chains: short chains (S) with a mean degree of polymerization (DP) ranging from 14 to 18, long chains (L) with DP 45–55, and a few chains with DP above 60.

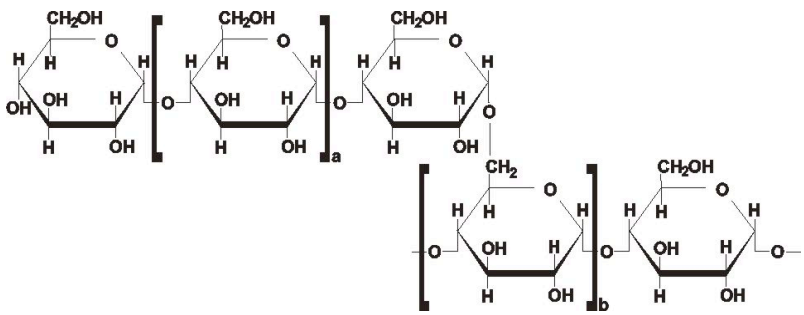

Figure 3. Chemical structure of amylopectin.

Polymodal chain distributions have been reported by Hizukuri et al. (**1986**),

Koizumi et al. (**1991**) and Hanashiro et al. (**1996**). The molecules were separated into four different fractions with DP in the intervals 6-12, 13-24, 25-36 and above 37. The X-ray diffraction pattern in starch granules seems to be dependent on amounts of the DP 6–12 fraction of amylopectin. Hence, Hizukuri et al. (**1997**) suggested that the S-chains with DP between 6 and 12 determined the starch crystalline allomorph. Nevertheless, Ong et al. (**1994**) considered that there was limited evidence to assess this influence of the S-chains on the allomorphism since these ratios were observed only in potato species.

Without doubt, the most important feature of this branched molecule is that the S-chains are responsible for the existence of discrete clusters. Nowadays, the cluster structure concept (**French, 1972; Robin et al., 1974**) is widely accepted. **Figure 4** shows the cluster model. An average chain length between 20 and 23 units interconnects two clusters. The validation of the cluster-type model (**French, 1972; Robin et al., 1974; Robin et al., 1975**) comes from the higher viscosity of amylopectin with respect to glycogen. The lateral assembly of clusters could explain the formation of crystallites. However, the exact global conformation of amylopectin inside a granule remains unknown (**Buléon et al., 1998**).

An alternative to study amylopectin chains is based on the combined use of static and dynamic light scattering of native molecules without any molecular weight reduction (**Burchard, Thurn, 1985; Thurn and Burchard, 1985**). Different models for amylopectin were proposed from the comparison of calculated and experimentally determined particle scattering functions from light scattering studies. The data confirmed that amylopectin is a heterogeneously branched polymer (**French, 1972; Robin et al., 1974; Robin et al., 1975**).

Amylopectin has a very large molecular weight (10^7–10^9) and there is a lack of knowledge about the molecular weight distribution. Chromatographic procedures are unable to fractionate this polymer on a molecular weight basis. For degraded amylopectins (**Yu and Rollings, 1987; Yu and Rollings, 1988**), the quantitative analysis of branching by SEC-MALLS was in good agreement with theoretical predictions made from modelling data.

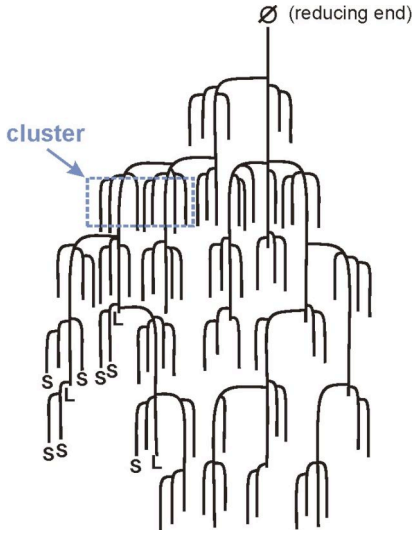

Figure 4. Scheme of the clustered architecture of amylopectin. (adapted from **Buléon et al., 1998**)

2.3. Crystal structure

Starch essentially crystallizes in the A, B allomorphs. A-type occurs in cereal starches whereas B-type is mainly found in tuber starches. A third type, called C, occurring commonly in legumes, roots and some fruits, was shown to correspond to a mixture of A and B types. The models for A and B structures are based on double-helices, right-handed (**Wu and Sarko, 1978a; Wu and Sarko, 1978b**) or left-handed (**Imberty et al., 1988; Imberty et al., 1991**) and packed in an antiparallel (**Wu and Sarko, 1978a; Wu and Sarko, 1978b**) or parallel (**Imberty et al., 1988; Imberty et al., 1991**) fashion in the unit cell. The left-handed form is energetically preferred to the right-handed form (**Imberty et al., 1988**).

The antiparallel packing is debated since it seems incompatible with the cluster model of amylopectin. The most acceptable models for A and B structures are based upon 6-fold left-handed double helices with a pitch height of 2.08–2.38 nm (**Imberty et al., 1988; Imberty et al., 1991**). In the A structure (**Imberty et al., 1988; Imberty et al., 1991**), the double helices are packed with the *B*2 space group in a monoclinic unit cell (a=2.124 nm, b=1.172 nm, c=1.069 nm, γ=123.5°) with eight water molecules per unit cell (**Figure 5A**). Recently, Popov et al. (**2006**) used synchrotron radiation microdiffraction of A-amylose single

crystals to refine the unit cell and confirm the monoclinic space group (*a*=2.0874 nm, *b*=1.146 nm, *c*=1.055 nm, γ=121.94°). In the B structure, double helices are packed with the $P6_1$ space group in a hexagonal unit cell (*a*=*b*=1.85 nm, *c*=1.04 nm) with 36 water molecules per unit cell (**Figure 5B**) (**Imberty et al., 1991**). The symmetry of the double helices differs in A and B structures, since the repeated unit is a maltotriosyl unit in the A form and a maltosyl unit in the B form (**Imberty et al., 1991**).

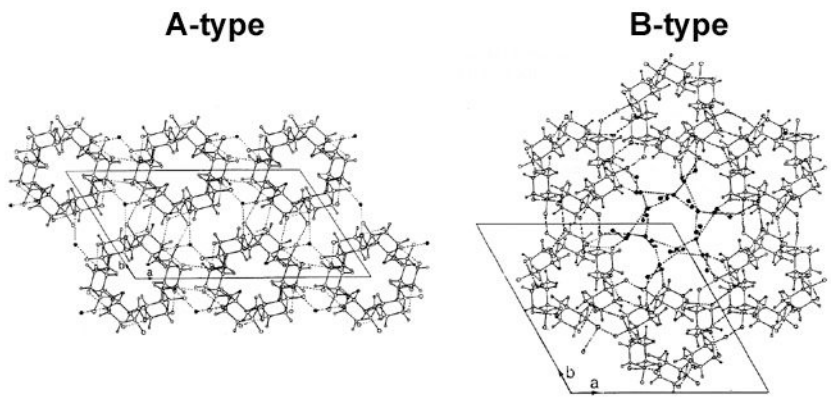

Figure 5. Projection of the crystal packing of double helices in A-type and B-type unit cells. (from **Imberty et al., 1988**).

2.4. The alternating ultrastructure of starch

The starch granule organization is very complex and depends on its botanical origin. Many questions on the semi-crystalline ultrastructure remain unanswered, such as the respective contribution of amylose and amylopectin to crystallinity, the distribution of ordered and disordered regions in the granule, the size distribution of crystalline regions or the organization in mixed A- and B-type granules. Detailed knowledge regarding the structure and the arrangement in the granule can be obtained studying the insoluble residue obtained after acid hydrolysis of native granules (**Robin et al., 1974**). Under acid conditions, granules weaken, crack and show a lamellar organization. The layered concentric shell structure of starch granules has been observed by scanning electron microscopy (SEM) and transmission electron microscopy (TEM) after acid hydrolysis (**Yamaguchi et al., 1979**), as

shown in **Figure 6**. The more resistant growth rings are believed to represent the crystalline part of the granule. Amorphous areas which are supposed to be more susceptible to acid hydrolysis would be hydrolyzed first.

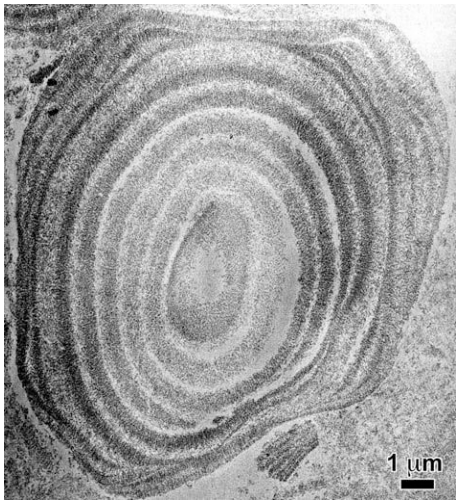

Figure 6. TEM image of a ultra-thin section of a waxy maize starch granule after 7 days of HCl hydrolysis (staining with lead citrate; image: I. Paintrand, CERMAV, Grenoble).

A schematic representation of the granule architecture is given in **Figure 7**. Starch granules are usually believed to consist of alternating 120-400 nm thick amorphous and semi-crystalline layers (**Gallant et al., 1992**). The organization of semi-crystalline shells has been widely studied by TEM imaging of thin sections of granules (**Gallant and Guilbot, 1969; Kassenbeck, 1978; Oostergetel and van Bruggen, 1989; Gallant et al., 1992**), small-angle X-ray (**Sterling, 1962; Cameron and Donald, 1992, 1993**) and neutron scattering (**Blanshard et al., 1984**). The crystalline shells are a succession of alternating amorphous and crystalline lamellae. The total thickness of one amorphous and one crystalline lamella is 9-10 nm (**Figure 7**). Putaux et al. (**2003**) used acid hydrolysis to determine the lateral dimensions of the elementary crystallites inside the crystalline lamellae. Insoluble residue consisted of crystalline lamellae made of parallelepipedal units with a length of 30–40 nm, a width of 15–25 nm, and a thickness of 5-7 nm.

Oostergetel and van Bruggen (**1993**) concluded that, in potato, the semi-crystalline domains formed a network of left-handed superhelices (diameter 18 nm,

pitch 10 nm), which could be a well-ordered skeleton for the starch granule. Lastly, Gallant et al. (**1992,1997**) proposed that lamellae are organized in spherical blocklets with a diameter ranging from 20 to 500 nm, depending on their location within the granule and the botanical origin of starch.

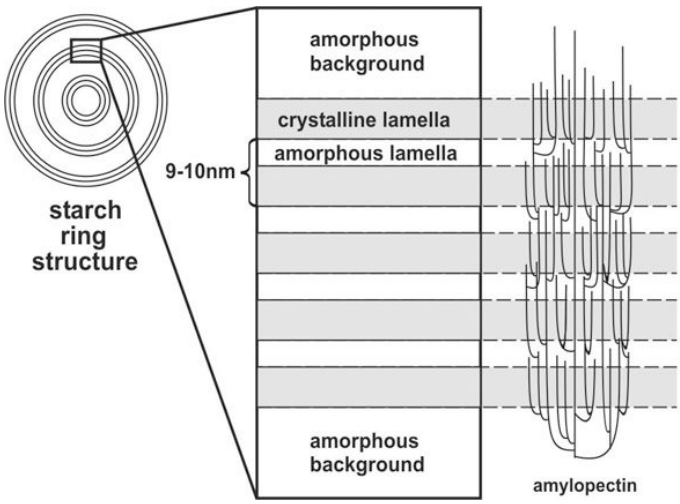

Figure 7. Scheme of the cluster model of amylopectin in the starch supramolecular architecture. (adapted from **Cameron and Donald, 1992**).

2.5. Macromolecular orientation

Figure 8 shows potato starch granules observed in water under polarized light. A characteristic Maltese cross (centred at the hilum) led to the granules being considered as distorted spherocrystals (**French, 1984**). The sign of birefringence is positive indicating that the average orientation of molecules is radial. The intensity of birefringence depends on the shape and orientation of the granules in the polarization system. Using solid-state light scattering of non-spherical granules, it was possible to observe that the molecular orientation was perpendicular to the growth rings and to the surface of the granule (**Borch et al., 1972**).

Buléon et al. used microfocus X-ray diffraction with a 2 μm beam to confirm that the molecules at the edge of potato starch granules were oriented perpendicular to the surface (**Buléon et al., 1997**). A lower level of orientation was found in the granule, but the

interpretation was more complicated since in the centre of the granule, the beam probably averaged over helices pointing forward, backward and sideways. No specific orientation at a 2 µm scale was found for wheat starch granules, either on the edges or in the centre, which means that the radial orientation in such granules is weak and limited to very small domains (**Buléon et al., 1997**).

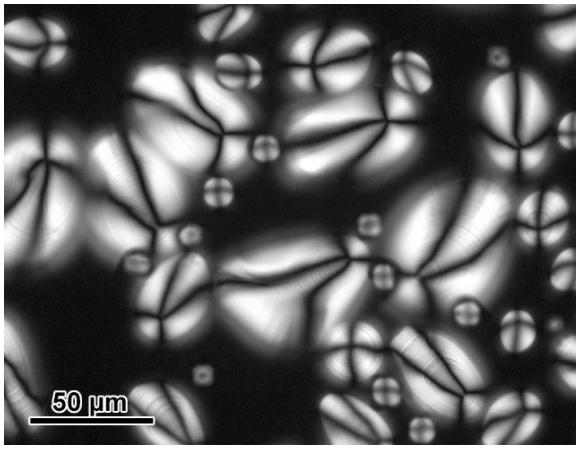

Figure 8. Polarized light optical micrograph of native potato starch granules in excess water (image: J.L. Putaux, CERMAV, Grenoble).

2.6. Thermal properties

Starch gelatinization is the collapse (disruption) of the molecular order within the starch granule resulting from irreversible changes in the properties such as granular swelling, native crystalline melting, loss of birefringence and starch solubilization (**Atwell et al., 1988**). It is an important starch functional property that varies with composition (amylose to amylopectin ratio, phosphorus, lipids, proteins and enzymes, etc.), molecular structure of amylopectin (unit chain length, extent of branching and molecular weight), granule architecture, crystalline to amorphous ratio, granule morphology and size distribution of starches (**Shiotsubo and Takahashi, 1984; Krueger et al., 1987; Cooke and Gidley, 1992; Singh, and Singh, 2001; Kaur et al., 2002; Singh and Singh, 2003; Kaur et al., 2004; Singh and Kaur, 2004; Kaur et al., 2005**). Gelatinization has been studied by various means such as thermal analysis (**Wada et al. 1979; Nakazawa et al., 1984; Shiotsubo and**

Takahashi, 1984), X-ray diffraction (**l'anson et al., 1988; Zobel et al., 1988; Cameron and Donald, 1992; Cameron and Donald, 1993**) and nuclear magnetic resonance (NMR) (**Chinachoti et al., 1991**). Differential scanning calorimetry (DSC) is the most common technique used to detect both first order and second order thermal transitions (**Huang et al., 1994; Nakazawa et al., 1984; Russel and Oliver, 1989; Yook et al., 1993**).

DSC studies have shown that starch modifications may alter thermal transition onset (T_{onset}), peak (T_{peak}) and conclusion (T_{end}) temperatures and the overall enthalpy (ΔH) associated with gelatinization. Upon hydroxypropylation, the reactive groups introduced into the starch chains are capable of disrupting the inter- and intra-molecular hydrogen bonds, leading to an increase in accessibility by water that lowers the temperature of gelatinization (**Seow and Thevamalar, 1993; Perera et al., 1997; Kaur et al., 2004**). Weakening of the starch granules by acetylation leads to early rupture of the amylopectin double helices, which accounts for the lower values of T_{onset}, T_{peak} and T_{end} (**Adebowale and Lawal, 2003**). The decrease in the thermal parameters is consistent with fewer crystals being present after modification (owing to damage to the crystals during acetylation) and with a cooperative melting process enhanced by added swelling (**Singh et al., 2004**).

Crosslinking also alters the thermal transition characteristics of starch, the effect depending on the concentration and type of cross-linking reagent, reaction conditions and the botanical source of the starch. An increase in gelatinization temperature has been observed for cross-linked starches. This phenomenom is related to the reduced mobility of amorphous chains in the starch granule as a result of the formation of intermolecular bridges. The level of phosphate cross-links has a strong influence on the DSC properties of starches. Choi and Kerr (**2004**) reported that cross-linked starches prepared using a relatively low concentration of the $POCl_3$ had gelatinization parameters similar to those of native starches, while cross-linked starches prepared using higher reagent concentrations showed considerably higher T_{end} and ΔH values. These results are consistent with those of Yeh and Yeh (**1993**) and Liu et al.(**2003**), who reported that ΔH of starch increased with increasing levels of cross-linking; however, T_{peak} was not affected significantly. Crosslinking at lower

levels reduces the proportion of the starch that can be gelatinized, resulting in a lower value of ΔH (**Yook et al., 1993**).

When a stored starch gel is reheated in a DSC, an endothermic transition occurs that is not present in the DSC scan of the freshly gelatinized sample. Such a transition is generally attributed to the melting of recrystallized amylopectin. The enthalpy of retrogradation is generally considered to correspond to order-disorder transitions of crystallites, i.e. double helices present in extended order arrays and regions of lesser crystalline order. The retrogradation properties of starches are indirectly influenced by the structural arrangement of starch chains within the amorphous and crystalline regions of the ungelatinized granule, which in turn, influences the extent of granule breakdown during gelatinization and the interactions that occur between the starch chains during gel storage (**Perera and Hoover, 1999**).

2.7. Alkaline extraction of Brazilian rice starch

The increase in the starch utilization as additive in the food industry (**Juliano, 1984**) has stimulated the development of different extraction methodologies with the purpose of isolating products with a high purity and well-defined physical properties. In this context, important advances have been made during the last decades in the development of methods for starch isolation. The alkaline extraction method was pioneered by Dimler et al. (**1944**) allowing the starch extraction from wheat and maize flours. This procedure proved to be an effective method for starch isolation from wheat flour giving high yield and purity. Since then, the alkaline extraction has been studied as an effective method for starch isolation from maize (**Mistry and Eckhoff, 1992a; Mistry and Eckhoff, 1992b**), wheat (**Dimler et al., 1944; Matsunaga and Seib, 1997**) and rice (**Yang et al., 1984; Lumdubwong and Seib, 2000; Chiou et al., 2002; Sodhi and Singh 2003; Puchongkavarin et al., 2005**). Among all of them, rice has received much attention mainly because of its applicability in industrial products and as food additive.

In the processing of Brazilian rice, during husk and polishing, a significant amount of rice grains is broken (**Elias et al., 2005**). This broken rice becomes a cheap product. It is abundant and can thus be used to produce starch. Due to its properties, rice starch can be used as a substitute of corn starch in food applications (**Juliano, 1984**). The alkaline procedure to isolate starch from rice is different from that used to extract starch from corn, wheat and potato. This is due to differences in protein content and starch properties in each case. The rice grain contains four types of proteins present in the endosperm. They are tightly associated with the surface of the starch granule making difficult their detection and removal (**Tanaka et al., 1980**). These proteins have been fractioned by selective solubility. The rice flour is first rinsed with water to remove albumin. Then, sequential treatments with dilute brine, dilute alkali and 70% ethanol solutions are performed to extract globulin, glutelin and prolamin, respectively (**Agboola et al., 2005**).

Thus, the alkaline method has commonly been used to extract the rice starch (**Yang et al., 1984; Lim et al., 1999; Lumdubwong and Seib, 2000; Chiou et al., 2002; Sodhi and Singh 2003**), in spite of the fact that this treatment can alter the structure of starch granules (**Lim et al., 1999; Chiou et al., 2002; Cardoso et al., 2006**). It is believed that the nature of the alkaline solution plays an important role in the modification of the granular structure of starch which, consequently, affects the organization and the physical properties of the resulting material (**Lugay and Juliano, 1965; Tako and Hizukuri, 2002; Puchongkavarin et al., 2005**). Due to the variety of conditions (alkali concentration and contact time with rice flour), it is important to investigate the effect of alkali during the extraction of starch.

2.8. V-amylose crystals

In contrast with its molecular simplicity, amylose is extremely versatile in its mode of crystallization. In its native form, this linear $\alpha(1\rightarrow4)$-D-glucan essentially crystallizes in the A and B allomorphs. Besides these two allomorphs, which can also be obtained by

crystallization from aqueous solutions (**Buléon et al., 1984; Gidley and Bulpin, 1987; Pfannemüller, 1987**), a number of single helical amylose complexes, categorized under the generic name of V-amylose have been described. The multiplicity of V-amylose crystals takes its origin in the remarkable number of hydrophobic or hydrophilic inorganic and organic guests that are susceptible to becoming associated with amylose helices serving as hosts (**Tomasik and Schilling, 1998a; Tomasik and Schilling, 1998b**). From a practical point of view, the study of these complexes is of interest in connection with flavor retention and release in food and as a molecular encapsulation principle, in particular in pharmacology and in the food industry.

Some of the crystalline V-amylose complexes yield well-resolved X-ray fiber diffraction diagrams. Structural models have been proposed but a number of details remain to be determined (**Winter and Sarko, 1974; Zaslow et al., 1974; Murphy et al., 1975; Rappenecker and Zugenmaier, 1981; Brisson et al., 1991**). In particular, it is not always clear to know whether guest molecules are included within the cavity of helical amylose, in between the helices, or in both locations.

When crystallized from dilute solution, depending on the guest molecule, amylose can yield remarkable micrometer-sized lamellar single crystals (**Manley, 1964; Bittiger and Husemann, 1969; Yamashita et al., 1973; Booy and Chanzy, 1979; Buléon et al., 1984; Whittam et al., 1989; Buléon et al., 1990; Welland and Donald, 1991**). They give sharp electron diffraction diagrams provided that precautions are taken to keep the guest molecules within the crystalline domains during the observation in the vacuum of the transmission electron microscope. With amylose in the V form, chain folding does not seem to be a problem, since similar monolamellar crystals with smooth surface can be obtained with any polymer chain length. This beneficial property must be related to the so-called 'flip' that is susceptible to occur between two adjacent glucosyl moieties connected by a $\alpha(1\rightarrow4)$-linkage (**Jacob et al., 1998; Gessler et al., 1999; Nimz et al., 2004**). Indeed, this flip, when it occurs, leads to a reversal of the molecular trajectory, thus favoring a chain folding mechanism to form lamellar crystals.

At present, five families of lamellar single crystals of V-amylose have been characterized in terms of morphology and electron diffraction diagrams. Hexagonal crystals of V_H amylose (**Figure 9A**), exhibit hexagonal diffractograms and are prepared from the addition of either hot ethanol or fatty acids to aqueous solutions of amylose (**Yamashita et al., 1973; Whittam et al., 1989; Brisson et al., 1991; Welland and Donald, 1991**). There are two families of rectangular V-amylose crystals presenting two different types of rectangular diffractograms. One of them, under the generic name of $V_{isopropanol}$ (**Figure 9B**), corresponds to crystals incorporating either isopropanol or a wealth of other complexing agents, namely some alcohols, ketones, as well as a number of organic reagents (**Yamashita and Hirai, 1966; Buléon et al., 1990; Nuessli et al., 2000**).

$V_{butanol}$ crystals (**Figure 9C**), which result from the addition of *n*-butanol or *n*-pentanol, correspond to the other family (**Manley, 1964; Yamashita, 1965; Yamashita et al., 1973; Booy et al., 1979; Helbert and Chanzy, 1994**). Square $V_{glycerol}$ crystals (**Figure 9D**), diffracting along a nearly 4-fold symmetry, are formed during the high-temperature crystallization of amylose with glycerol in the absence of water (**Hulleman et al., 1996**). A fifth family is obtained with α-naphthol or quinoline as complexing agents. The crystals of $V_{\alpha\text{-naphthol}}$ (**Figure 9E**) have a squarish shape and yield electron diffractograms with 4-fold symmetry (**Yamashita and Monobe, 1971;. Winter et al., 1998; Helbert, 1994**). It is likely that the number of families of lamellar single crystals of V-amylose will be greater than 5. Among the candidates, it seems that V_A or V_{DMSO} amylose should also yield lamellar single crystals, since both allomorphs can be readily crystallized to a substantial perfection, denoted by well-resolved X-ray diagrams (**Winter and Sarko, 1974; Murphy et al., 1975**). However, so far, all attempts of crystallizing these allomorphs from dilute solutions have resulted in the production of sharpeless precipitates but not lamellae.

The resolution of the crystal structure of V_H amylose has shown that this allomorph consisted of the hexagonal close packing of left-handed 6-fold amylose helices, together with intra and extrahelical molecules of water (**Winter and Sarko, 1974; Zaslow et al., 1974; Murphy et al., 1975; Rappenecker and Zugenmaier, 1981; Brisson et al.,**

1991). In the V_H case, the intra-helical cavity may also accept a number of linear guests (**Godet et al., 1993a; Godet et al., 1993b; Nimz et al., 2004**), but there is no room for them in between the helices. Upon selective drying, the crystals of $V_{butanol}$, $V_{isopropanol}$ and $V_{glycerol}$ invariably yield V_H electron diffraction diagrams (**Manley, 1964, Booy et al., 1979; Buléon et al., 1990; Helbert and Chanzy, 1994; Hulleman et al., 1996**) which suggests that these crystalline complexes also consist of left-handed 6-fold amylose helices, with some of the guest molecules located between the helices. The $V_{isopropanol}$ crystals have also been described as made of 7-fold helices by analogy with β-cyclodextrins (**Yamashita and Hirai, 1996**). However, their reversible conversion into the 6-fold V_H structure without change in morphology is questioning the occurrence of 7-fold helices in these crystals.

The case of the $V_{\alpha\text{-naphthol}}$ crystals is drastically different from that of 6-fold V-amylose since, in this complex, the amylose chains are thought to form 8-fold helices (**Yamashita and Monobe, 1971; Helbert, 1994; Winter et al., 1998**). At present, almost no firm data exists on this type of V-amylose complexes. The only crystals described so far have rather poor shapes and nothing is known regarding their stability.

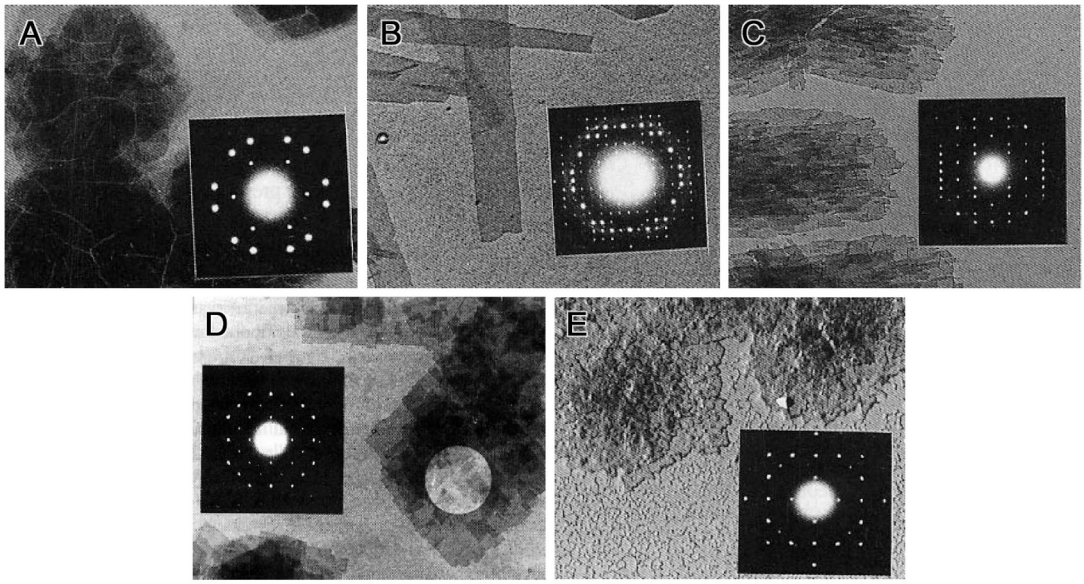

Figure 9. V-amylose single crystals and their corresponding electron diffraction.
A: V_H ; B: $V_{isopropanol}$; C: $V_{butanol}$; D: $V_{glycerol}$; E: $V_{\alpha\text{-naphthol}}$
(images and diffraction patterns: W. Helbert, CERMAV, Grenoble, France).

CHAPTER 3

MATERIALS AND METHODS

3.1. Starch isolation

Industrial *indica* rice (BR-IRGA 410) of Brazilian origin was supplied by "Cooperativa Arrozeira Extremo Sul" (Pelotas, Brazil) containing 8% protein, 32% amylose, 58% amylopectin and 2% of other components. The rice was milled and the fraction with granulometry between 0.10 and 0.42 mm was used. Starch was isolated by alkaline extraction of the proteins as described by Sodhi and Singh (**2003**). Six NaOH concentrations were tested: 0.06, 0.12, 0.15, 0.18, 0.24 and 0.30% w/v for treatment 1 to 6, respectively. In order to soften the endosperm, 1.8 g of milled rice was steeped in 18 mL of NaOH and allowed to settle for 24 h, at 20°C. The supernatant liquor (12 mL) was discarded and the remaining slurry was diluted to the original volume (18 mL) with NaOH. The mixture was shaken for 10 min and centrifuged at 1250 rpm for 5 min in an analytical centrifuge ALC model PK 120. After that, the supernatants and the slurry parts were once more separated. This procedure was repeated eight times and eight supernatants were produced during each treatment. The slurry starch was suspended in distilled water, passed through a 0.125 mm nylon cloth and centrifuged at 2000 rpm for 5 min. Finally, the samples were washed with distilled water until pH 7.0 to give the treated starches. The total yield of starch was determined to be 60 ± 10%.

3.1.1. Protein detection

3.1.1.1. Intrinsic fluorescence spectroscopy

Intrinsic fluorescence spectroscopy was used in order to detect protein presence in the supernatant fractions. The analyses were performed in a Hitachi F-4500 spectrofluorometer operating in the 300-600 nm range of using an excitation wavelength of 350 nm. The different supernatants obtained during starch isolation were analysed without any dilution using a quartz optical cell. A multi-peak fitting procedure was performed in order to determine the area of emission spectra.

3.1.1.2. Biuret colorimetric test

The biuret test was applied following standard procedures (**AACC, 2000**). In this method, protein detection is based on the capacity of the cupric ion to form coordination compounds with nitrogen in the peptide bond of the proteins. Four different color graduations provide qualitative information about the presence of proteins, as follows: light blue, which indicates proteins absence; dark blue, indicating the probable presence of proteins; and light purple and dark violet, indicating the presence of proteins.

3.1.1.3. UV/Vis

The UV/Vis measurements of the different supernatant solutions were performed in a Shimadzu UV-1601PC spectrometer using a quartz cell with a 10.0 mm optical path. The solutions obtained from the biuret test were analyzed without any dilution. The UV/Vis spectra in the range between 350 and 700 nm were recorded. The absorption intensity at λ_{max} (540 nm) brought additional quantitative information to the protein detection.

3.1.1.4. General procedure for protein labelling using pyrene molecule (Py)

In order to record the fluorescence spectra of the supernatants, pyrene was added to the different supernatant fractions obtained during starch isolation of treatment 5. The emission spectra of the pyrene molecule (Py), concentration 1 x 10^{-7} M, were recorded in the range of 350–600 nm, using a Hitachi F-4500 spectrofluorometer. The excitation wavelength employed was 336 nm. The ratio I_1/I_3 of the first (373 nm) and third (384 nm) peaks in the Py emission spectrum, sensitive to the local polarity (**Winnik et al., 1987; Grieser and Drummond, 1988; Evertsson et al., 1996; Christoff et al., 2001**), was used to detect the presence of proteins in the supernatants during starch isolation.

3.1.1.5. General procedure for protein labelling using isothiocyanate benzoxazole dye

The isothiocyanate was dissolved in DMSO to a final concentration of 1 mg/mL. Small aliquots of this solution (400 μL) were added, slowly and with gentle stirring, to 5 mL of the supernatant solution. The protein–dye mixture was kept overnight at room temperature (25°C). The rice proteins were labelled using an excess of fluorochrome in order to increase the maximum yield, since it is reasonable to assume that labelling will not occur for all protein residues. In addition, some residues may be unavailable due to protein folding. As observed in a previous work, these labelled proteins could not be separated from free dyes by gel filtration chromatography on Sephadex® G-50 (**Holler et al., 2002; Rodembusch et al., 2005b**). In the present work, the separation of the labelled protein from free fluorescent dye was achieved by washing the eight protein solutions five times with ethyl acetate, in which the dye is highly soluble.

3.1.2. Morphology and structure of starch granules

3.1.2.1. Wide-angle X-ray diffraction (WAXS)

WAXS data were collected at room temperature using a diffractometer powered by a Philips PW3830 generator providing a Ni-filtered CuKα radiation (λ=1.542 Å) and operating at 30 kV and 20 mA. X-ray diffraction patterns were recorded after equilibration of the water content in the washed starch at 90% R.H. (relative humidity) for 9 days. The hydrated powders were sealed in borosilicate capillaries in order to prevent any significant change in water content during measurement. Diffraction patterns were recorded during 2 h exposures on Fujifilm imaging plates and read using a Fujifilm BAS 1800 II Phospo-imager. Calibration was achieved using calcite powder. Diffraction spectra were obtained by radial averaging of the powder patterns and normalized to the same total integrated area between 2θ=3 and 35°.

3.1.2.2. Differential scanning calorimetry (DSC)

DSC measurements were performed with a Perkin Elmer DSC-4 calorimeter using heating scan rates of 5°C/min from 25 to 100°C. Before analysis, the water content in the specimens was adjusted by water desorption at 90% R.H. for 9 days. The calibration was performed using indium and an empty aluminum pan was used as reference. The transition temperatures and enthalpies were determined using the Pyris software.

3.1.2.3. Scanning electron microscopy (SEM)

Drops of granule suspensions were allowed to dry onto copper stubs. The specimens were coated with Au/Pd and observed in secondary electron imaging mode with a JEOL JSM-6100 microscope at Centre de Recherche sur les Macromolécules Végétales, France, operating at 8 kV voltage.

In addition, the aqueous starch suspension of treatment 5 was supercritically dried using CO_2 and subsequently coated with gold prior to examination. For this particular sample, scanning electron microscopy images were obtained using a JSM-5800 microscope at Centro de Microscopia Eletrônica, UFRGS, Brazil under an accelerating voltage at 20 kV.

3.1.2.4. Small-angle X-ray scattering (SAXS)

The eight slurry starch samples produced during the alkaline treatment 5 were evaluated by SAXS. The measurements were carried out at the “Laboratório Nacional de Luz Síncrotron – LNLS” (Campinas, Brazil), on the beamline D11A, the wavelength of the X-rays being 0.1608 nm. The slurry starch samples were placed between two mica sheets. A collimated X-ray beam was passed horizontally through a chamber containing the sample, under vacuum. Afterwards the beam was diffracted on a linear detector placed at 43.5 cm from the sample. Measurements were performed at 20°C with an exposure time of 5 min. Silver behenate was used for calibration purposes. The intensities were corrected taking into account the detector response and the dark current signals, as well as the sample transmission and the background scattering.

3.1.2.5. Optical microscopy

The birefringence of the slurry starches obtained in treatment 5 were evaluated qualitatively using an Olympus BX41 microscope operated with polarized light.

3.1.2.6. Mie scattering

The particle size distribution of the final starch was determined by Mie scattering analysis, using a Cilas 1064 standard setup. Data analysis was performed using the “particle expert” software by Cilas. The starch concentration was approximately 0.3 mg/mL. In order to guarantee their homogeneity, the samples were submitted to soft ultrasound radiation during the experiment.

3.2. Light scattering of aqueous amylose solutions

3.2.1. Amylose extraction

Amylose was isolated from rice starch (BR-IRGA 410) by precipitation with thymol, as previously described by Haworth et al. (**1946**). Starch was dispersed in boiling water (1% w/v) and kept under stirring for 30 min. Sodium chloride (0.1% w/v) and thymol (0.13%) were added to the mixture and the solution was cooled rapidly to room temperature. The mixture was allowed to settle for 48 h for the complex precipitation. The precipitate was washed with saturated thymol solution, ethanol and ether. The final product was dried in vacuum at room temperature. Isolated amylose was dispersed in 1 M KOH, gently stirred overnight and then diluted to pH 10.5. The sample (5 mL in KOH pH 10.5) was submitted to a gel filtration chromatography in a column (2.6 x 100 cm) packed with Sephacryl S-400 percolated with KOH pH 10.5 at a flow rate of 8 mL per hour (linear flow 1.5 cm/h), at 4°C. The initial 5 mL were rejected and fractions of 1 mL were then collected for dynamic (DLS) and static light scattering (SLS) analysis. Fractions were named according to the correponding mL number (e.g., *f7* is the fraction colected during the elution of the 7th mL).

The fractionated amylose was shown to be contaminated with amylopectin. To overcome this drawback commercial amylose (Sigma) was also used in some light scattering experiments. In this case, amylose was dissolved in 1M KOH solution and stirred over night. After complete polymer dissolution, the amylose solutions were diluted with water or HCl solution in order to obtain different ionic strengths. Samples were filtered through 0.22, 0.45 and 1.20 μm pore membranes and placed into dust free cells for light scattering experiments. The measurements were performed at different storage times.

3.2.2. Light scattering

Light scattering measurements were performed on an automatic BI-200M goniometer and a BI-9000 AT digital correlator (Brookhaven Instruments). A coherent He-Ne laser (λ=632.8 nm) was used as light source. All solutions were thermostated in a refractive-index-matching liquid (decaline) at room temperature. The experiments were performed in triplicate. Static (SLS) and dynamic light scattering (DLS) experiments were performed at 9 different scattering angles θ within the range 35° < θ < 145° . Three individual 3 min runs per angle were taken in DLS experiments.

In SLS, the equation for the scattered static intensity of a polydisperse system is given by the Zimm equation (**Berne and Pecora, 1976**):

$$\frac{Kc}{R(\theta)} = \frac{1}{M_{\mathrm{w}}}\left(1 + \frac{1}{3}q^2\left\langle R_{\mathrm{g}}\right\rangle_{\mathrm{Z}} + \ldots\right) + 2A_2c + 3A_3c^2 + \ldots \tag{1}$$

$$K = \frac{4\partial^2 n_{\mathrm{o}}{}^2\left(\mathrm{d}n/\mathrm{d}c\right)^2}{N_{\mathrm{A}}\ddot{e}_{\mathrm{o}}{}^4} \tag{2}$$

$$R(\theta) = \frac{r^2 i_\theta}{I_{\mathrm{o}}} \tag{3}$$

where the concentration c is expressed in g/cm^{-3}, q = (4π/λ)sin(θ/2) is the wave vector, λ the wavelength of the incident beam, n_{o} is the refraction index of solvent and $R(\theta)$ is the Rayleigh ratio.

This method was applied to estimate M_w from the commercial amylose used in this work. The radius of gyration (R_g) for the amyloses was obtained by SLS using the dissymmetry method (**Hellweg and Eimer, 1998**), according to the following relation:

$$\frac{I_\theta}{I(180^\circ - \grave{e})} \cong 1 + 2\left(\frac{R_g}{3}\right)q^2 \tag{4}$$

Moreover, in DLS analysis the fluctuations in the scattered intensity are due to the Brownian motion of the macromolecules in scattering volume (**Berne and Pecora, 1976**). The counted photons are correlated in the time, giving an autocorrelation function (ACF) with exponential decay. The characteristic relaxation time (τ) is related to a characteristic frequency or relaxation rate (Γ) through the relation:

$$\hat{o} = \frac{1}{\Gamma} \tag{5}$$

The apparent translational diffusion coefficient of the macromolecule in the solution can be determined by the slope of the curve given by the following relation:

$$D_T = \frac{\Gamma}{q^2} \tag{6}$$

The hydrodynamic radius (R_h) can be derived from the diffusion coefficient in infinite dilution, D_o, via Stokes-Einstein relation:

$$R_h = k_B T/(6\partial\eta_o D_0) \tag{7}$$

where k_B is Boltzmann constant, T is the temperature of the sample and η_o is the viscosity of the medium. If D is determined with $q_{\to 0}$ e $c_{\to 0}$, R_h corresponds to the absolute hydrodynamic radius, contrary case it is an apparent hydrodynamic radius.

In this work, the ACFs were analysed by the REPES algorithm (**Jakes, 1995**). The fitting procedure was performed directly on the intensity autocorrelation function $g_2(t)$ rather than the field autocorrelation function $g_1(t)$.

3.3. V amylose single crystals

3.3.1. Preparation of the crystals

3.3.1.1. $V_{isopropanol}$ crystals

Synthetic amylose with an average degree of polymerization (DP) of 100, a gift from Dr. Gessler (Free University of Berlin), was dispersed in water (0.1% w/v). The solution was sonicated for 5 min to break aggregates and submitted to nitrogen bubbling for 20 min to remove dissolved oxygen. The solution was sealed in a metallic autoclave, heated in an oil bath for 60 min at 150°C and cooled to 80-85°C. At this temperature, the solution was filtered through a 0.2 µm pre-heated filter and 35% v/v of warm isopropanol (70°C) or linalool (65°C) were added to the amylose solution. The mixture was maintained at 65°C for 2 h. The sample was then kept at room temperature and the crystallization occurred within a few hours.

3.3.1.2. $V_{\alpha\text{-naphthol}}$ crystals

Aqueous suspensions of DP 100 synthetic amylose (0.05% w/v) were prepared and α-naphthol was added in a proportion of 1:3 (w/w) with respect to the amylose. The mixture was submitted to nitrogen bubbling for 20 min and then sealed in a vial, which was heated to 150°C by immersion in an oil bath. After 60 min, the solution was filtered through a 0.2 µm preheated filter and the filtrate was kept at 95°C for 2 h before being cooled to room temperature. Crystallization occurred overnight.

3.3.1.3. Density measurement

A film resulting from the drying of a $V_{\alpha\text{-naphthol}}$ crystal suspension was floated on chloroform to which cyclohexane was slowly added. The density of the mixture was measured when the film sank to remain in equilibrium in the mixture of liquids.

3.3.2. Transmission electron microscopy

3.3.2.1. Conventional imaging and electron diffraction

Drops of crystal suspensions were deposited on glow-discharged carbon-coated grids and allowed to dry. For the recording of electron diffraction, some specimens were observed at room temperature and mounted on a Philips rotation holder. Others were mounted on a Gatan 626 cryo-holder operated at liquid nitrogen temperature. In this case, the specimens were quench-frozen in liquid nitrogen prior to insertion in the electron microscope in order to prevent any evaporation of the α-naphthol in the vacuum of the microscope. Base plane electron diffraction diagrams corresponding to *hk0* reflections were collected either at room or liquid nitrogen temperature on crystals with lamellar base perpendicular to the electron beam. Diagrams containing upper layer line reflections were recorded on crystals that were tilted around selected reciprocal axes. Electron diffraction diagrams were recorded on 1 μm^2 circular areas of single crystals. For calibration purpose, crystals were deposited onto gold-coated TEM carbon films, and the diffraction spots were calibrated at room temperature using the diffraction rings of gold.

All observations were performed with a Philips CM200 'Cryo' electron microscope operated at 80 kV for conventional imaging and 200 kV for electron diffraction and high resolution imaging. Images were recorded on Kodak SO163 films and diffraction patterns on Fujifilm imaging plates, read with a Fujifilm BAS-1800II bioimaging analyzer.

3.3.2.2. High resolution electron microscopy

HREM imaging was performed at room temperature with the specimen mounted in a simple-tilt holder. Images were recorded on Kodak SO163 films, at magnifications of 38 000× and 50 000×. No objective aperture was used. Prior to image recording, the crystals were selected by searching the specimen in diffraction mode, with a very low illumination. When the diffraction pattern exhibited high symmetry and spot intensity, the beam was immediately blanked, the microscope switched into imaging mode and the illumination increased. The beam was deblanked and the plate exposed for 1-2 s corresponding to underexposures of a factor 8 with respect to the automatic exposure time. Laser diffractometry on an optical bench was used to select the HREM negatives that exhibited diffracting areas. The regions of interest were chosen depending on the symmetry and resolution of the observed spot pattern. The selected areas were photographically enlarged 4 times on Kodak 4489 films and digitized using an 8 bits Kodak Megaplus digital CCD camera. The images were processed on a Silicon Graphics workstation using the Semper 6.4 program (Synoptics, UK) (**Saxton et al., 1979**).

3.3.3. Synchrotron X-ray diffraction

Synchrotron X-ray experiments were performed on the BM1 beamline at the European Synchrotron Radiation Facility (ESRF, Grenoble, France), using a 0.2×0.2 mm^2 monochromatic beam (λ=0.7840 Å). A suspension of $V_{\alpha\text{-naphthol}}$ crystals was allowed to evaporate in flat polyethylene capsules. Pieces of the resulting mats were introduced in 1.0 mm o.d. glass capillaries and mounted on a 3-axis goniometer. A series of textured diagrams were recorded by changing the orientation of the mat with respect to the incident beam. The diffraction diagrams were collected using a MAR345 imaging plate recorder, positioned about 165 mm from the sample, and scanned with a 100 µm resolution. A powder diffraction pattern of LaB_6 was collected under the same conditions to calibrate the detector distance, the detector tilt, and the position of the center. The sample tilts and rotations were

measured from the azimuthal angles of *hk*0 reflections. Using these values, the diffraction diagrams were mapped into reciprocal space, and the background subtracted using a Sonneveld algorithm extended in two dimensions (**Sonneveld and Visser, 1975; Nishiyama et al., 2002**). The position of low-resolution X-ray diffraction peaks was measured by fitting Gaussian functions and a linear baseline to the radial line profile. The unit cell parameters were determined from the positions of the 002 and 011 peaks that are strong and not influenced by neighboring reflections. The position of these peaks was determined by least-square fitting of the radial profiles.

3.3.4. Molecular modeling

3.3.4.1. Conformational parameters

Molecular models have been built with the Cerius^2 modeling package. The recommendations and symbols proposed by the Commission on Nomenclature (**IUPAC-IUB, 1983**) have been used. The atomic labeling scheme is shown in **Figure 10**.

The relative orientation of two contiguous residues was described by the bond angle τ=C1-O4'-C4' and two torsion angles: ϕ=O5-C1-O4'-C4', Ψ=C1-O4'-C4'-C5'. The torsion angle ω=O5-C5-C6-O6 describes the orientation of the hydroxymethyl group. The orientation of the O6 atom to the ring oxygen (O5) and to C4 can be trans-gauche (*tg*), gauche-gauche (*gg*), or gauche-trans (*gt*). The first letter refers to the orientation of O6 relative to O5 and the second to C4. These orientations correspond to ω torsion angles -60°, 60° and 180°, respectively. A code will be used to differentiate the amylose chains studied here. The first letter describes the chirality of the helix while the integer 1, 2 and 3 describes the orientation of the hydroxymethyl group: *gg*, *gt* and *tg* respectively. Thus L_1 means left-handed helix having its hydroxymethyl groups in the *gg* orientation.

The shape of the pyranose ring is defined by the 3 puckering parameters (**Cremer and Pople, 1975; Perez et al., 2000**). The puckering amplitude Q measures the

deviation from planarity, the polar phase angle of puckering ϕ describes the type of distortion. The third puckering parameter is the polar azimuthal angle Θ for the pseudo-rotational sphere of radius Q.

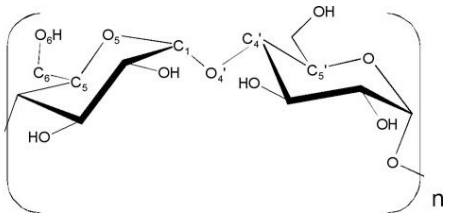

Figure 10. Schematic drawing of the structural segment of the amylose chain along with the nomenclature of selected atoms. For clarity, hydrogen atoms were omitted.

3.3.4.2. Model energy calculation

Molecular mechanics and dynamics simulations have been performed with the Cerius^2 modeling package. The Universal 1.02 force field has been considered (**Rappe et al., 1992**). Electrostatic charges on each atom were calculated using the charge equilibration method (**Rappe and Goddard, 1991**).

3.3.4.3. Molecular dynamics

Molecular dynamics simulations were performed in the NVT and NPT ensembles. The standard Verlet algorithm (**Verlet, 1967**) was used to integrate Newton's law of motion with a time step of 0.001 ps. Relaxation time constants and the mass-like parameter which determines the rate of change of volume/shape matrix were set to 0.1 ps and 1.00, respectively. The molecular dynamics run was started by assigning initial velocity for the atoms according to a Boltzmann distribution at 2*T*, *T* being the target temperature. The velocities of the atoms were quickly scaled down so that the final temperature of atoms was *T*. The total external pressure was maintained at 1 atm, and Nosé's algorithm (**Nosé, 1984**) was used to keep the cell temperature constant. All calculations were performed on Silicon Graphics workstations at the Centre d'Expérimentation et de Calcul Intensif (CECIC, Grenoble, France).

3.3.4.4. Hydrogen bonds

The method traditionally used to detect a hydrogen bond is geometric: two oxygen atoms are considered hydrogen-bonded if the distance between the hydrogen of the donor and the oxygen acceptor is lower than 2.5 Å and if the angle between the oxygen donor, the hydrogen donor and the oxygen acceptor larger than 90°.

3.3.4.5. Connolly surface area and accessibility of functional groups

Surface areas and accessibility of the functional groups were estimated using the Connolly surface tools. The radius of the probe was 1.4 Å.

3.3.4.6. Theoretical electron diffraction pattern

Theoretical electron diffraction patterns of the models of the $V_{\alpha\text{-naphthol}}$ complex were calculated using the single crystal approximation in the Cerius[2] software. The electron radiation energy was 200 KeV.

3.3.4.7. Model refinement

The SHELX program was used to refine the minimized structures against the experimental electron diffraction data. An intensity average was calculated for groups of symmetry-related reflections. Electron diffraction spots presenting double diffraction effect were excluded.

CHAPTER 4

ALKALINE EXTRACTION OF BRAZILIAN RICE STARCH

4.1. Protein removal

Figure 11 shows the fluorescence spectra of the supernatants obtained after treatment 3. All spectra have the same general appearance although the maximal intensity and peak area vary depending on the supernatant number. The first peak is located at 397 nm for all supernatants and it gets more clearly defined for supernatant 3 and onward. The second peak is located at 450 nm for supernatants 1 to 4 whereas it is shifted to approximately 455 nm for supernatant 5 and onward. Fluorescence quenching was not observed during the procedure. According to this, the absolute area of the fluorescence spectra was related to the amount of protein in the supernatants.

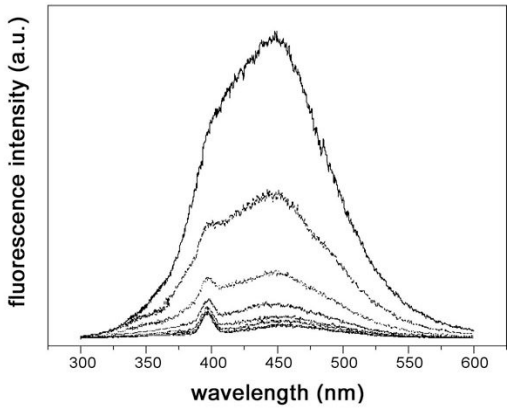

Figure 11. Fluorescence spectra of the supernatants obtained after treatment 3, from supernatant 1 (top) to supernatant 8 (bottom).

Figure 12 presents the fluorescence emission (solid line) and a multi-peak fitting (dashed line) for supernatant 8. The comparison between the real emission and the fit analysis showed that multi-peak fitting could be used in order to define the area of fluorescence emissions accurately.

The calculated areas of the fluorescence emission from different supernatants are presented in **Table 1**. The alkaline extraction during a same treatment led to a decrease of the peak area due to the reduction of the amount of proteins during the treatment. Hence, the sum of the peak areas in each treatment is related to the total amount of proteins removed during the procedure. In treatments 1 and 2, the total amount of proteins extracted

was smaller when compared with the other ones. In treatments 3, 4, 5 and 6, no significant difference could be observed, indicating that, quantitatively, the protein removal was practically the same.

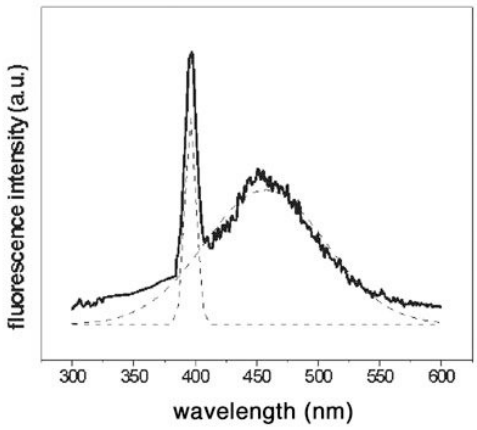

Figure 12. Multi-peak-fit of the fluorescence emission spectrum of supernatant 8.

Supernatants 7 and 8 obtained in all treatments presented a positive and constant area. The positive area in supernatant analyses indicated the presence of proteins even after eight washes with different NaOH concentrations. This result is in agreement with the literature that reports that the starch obtained by alkaline extraction presents a small amount of residual proteins (**Yang et al., 1984; Lumdubwong and Seib, 2000; Cardoso et al., 2007a**).

Table 1. Fluorescent supernatant peak area obtained by multi-peak fitting for different treatments.

supernatant fraction	supernatant area x 10^{-3} (a.u.)					
	treatment 1	treatment 2	treatment 3	treatment 4	treatment 5	treatment 6
1	21.7	31.4	33.4	33.9	33.2	33.4
2	12.9	15.6	15.7	15.6	16.4	16.5
3	5.0	6.9	7.6	7.0	7.0	6.9
4	2.7	2.8	3.2	3.3	3.2	3.3
5	1.7	1.9	2.3	2.3	2.1	2.2
6	1.1	1.2	1.3	1.3	1.4	1.3
7	0.9	1.0	1.2	1.2	1.2	1.2
8	0.9	1.0	1.2	1.2	1.2	1.2
total area	47.2	62.2	66.3	66.1	66.1	66.3

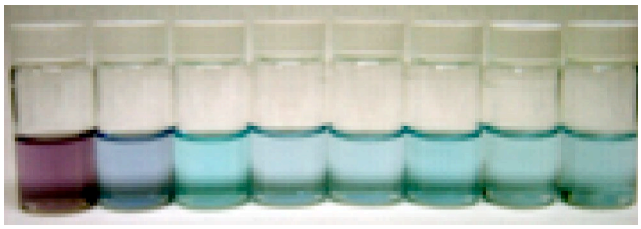

Figure 13. Biuret test of the protein solutions (1 to 8, from left to right).

The area of the peaks in the beginning of the treatments is probably related to the contributions of all proteins. When the treatment is advanced and the proteins are extracted by NaOH solution, the fluorescence area is reduced. In the last two extractions (supernatants 7 and 8), a constancy of the peaks in the spectra is observed. The high solubility of albumin, globulin and glutelin in NaOH solutions suggests that these proteins were totally extracted in supernatant 6 and the presence of proteins in supernatant 7 and 8 can be assigned to prolamins (**Cardoso et al., 2007a**). Moreover, the fluorescence emitted by supernatants 7 and 8 coincides with that of prolamins measured in alkaline medium using an excitation wavelength of 350 nm. The presence of proteins in this stage is directly related to the poor solubility of prolamin in NaOH solutions.

In order to study specifically the treatment 5 since most of alkaline extraction works use NaOH solutions at 0.25% w/v (**Yang et al., 1984; Lumdubwong and Seib, 2000; Sodhi and Singh, 2003; Chiou et al., 2002; Puchongkavarin et al., 2005**), other tests of protein detection were performed to compare with the results showed above.

Table 2. Results from the biuret colorimetric test.

supernatant	color graduation	qualitative information
1	deep violet	presence of protein
2	slight purple	presence of protein
3	dark blue	non conclusive
4	light blue	absence of protein
5	light blue	absence of protein
6	light blue	absence of protein
7	light blue	absence of protein
8	light blue	absence of protein

Currently, the qualitative biuret test has been used as a classical test to detect proteins during the alkaline extraction of starch (**Sodhi and Singh, 2003**). The results of the biuret test for the eight supernatant solutions of treatment 5 are presented in **Figure 13** and summarized in **Table 2**.

The colors obtained for supernatants 1 and 2 clearly indicate the presence of proteins. The color of supernatant 3 was not conclusive.

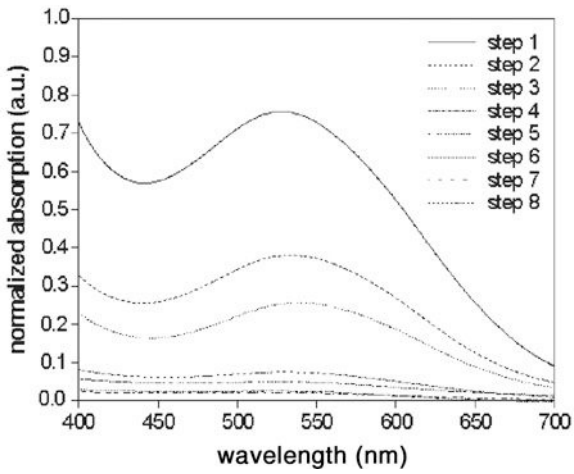

Figure 14. UV-vis spectra of the supernatant samples.

During the biuret test, the supernatants in step 4 and onward exhibited a light blue color, thus indicating absence of proteins.

Figure 14 shows the UV/Vis spectra of the eight supernatants obtained during the alkaline procedure. They all show a peak centered at λ_{max} = 540 nm. This peak is related to the presence of proteins in the supernatants, because it decreases as the protein concentration decreases. The intensity of the absorption at λ_{max} was used to measure the quantity of proteins present. **Table 3** summarizes the UV/Vis results in terms of the protein presence factor $\alpha_{UV\text{-}vis}$ in the supernatants.

This factor is related to the measured absorption values, *A*, as follows:

$$\alpha_{UV\text{-}vis} = [A_n - A_8] / [A_1 - A_8] \quad (8)$$

with *n*, the number of the extraction step, varying from 1 to 8.

Table.3. UV-vis and fluorescence results for the protein presence in different steps of the alkaline extraction using NaOH solution at 0,24% w/v.

supernatant step n°	UV-vis		fluorescence	
	$\alpha_{UV\text{-}vis}$	protein presence	α_{FLU}	protein presence
1	1.00	++	1.00	++
2	0.41	+	0.43	+
3	0.21	+	0.28	+
4	0.08	+	0.16	+
5	0.05	+	0.10	+
6	0.02	+	0.04	+
7	0.00	-	0.00	-
8	0.00	-	0.00	-

Figure 15 presents a set of fluorescence spectra of the supernatants, using pyrene (Py) as the fluorescent probe. All spectra are characterized by four spectral bands that allow identification of small quantities of proteins in the supernatants at each starch extraction step. **Table 3** summarizes the fluorescence results in terms of the protein presence factor α_{FLU}, using the ratio I_1/I_3 as depicted below:

$$\alpha_{FLU} = [\ (I_1/I_3)_8 / (I_1/I_3)_n\ ] / [\ (I_1/I_3)_8 / (I_1/I_3)_1\ ] \qquad (9)$$

with *n* the number of the extraction step, varying from 1 to 8.

Both α_{FLU} and $\alpha_{UV\text{-}vis}$ values initially decrease and become zero after the seventh extraction step when no further protein was detected. Hence, using the protein presence factor it was possible to detect the presence of proteins until the sixth step. Additionally, a small band at 540 nm in the UV/Vis spectra and a baseline shift at 466 nm in the fluorescence spectrum of supernatants 7 and 8 are worth mentioning, which may indicate the presence of residual amounts of proteins. However, the biuret test results indicate no protein after the third stage (**Table 2**). Therefore, UV/Vis and fluorescence spectroscopy proved to be more sensitive to the detection of proteins if compared to the classical biuret test.

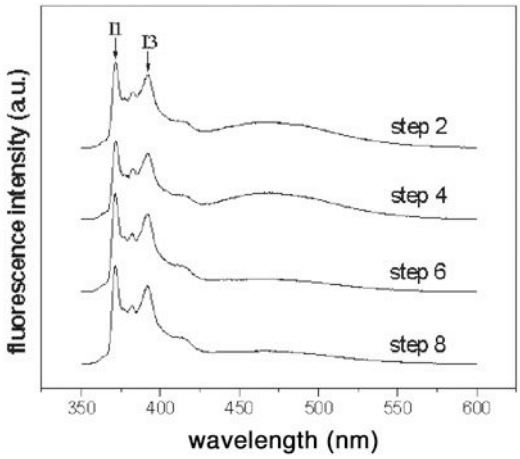

Figure 15. A set of fluorescence spectra of the supernatants registered by using pyrene (Py) as a fluorescent probe.

Finally, in this work the presence of rice proteins in supernatant solutions was evaluated by a new methodology based on direct fluorescence detection using a benzoxazolic isothiocyanate derivative from rice protein-fluorescent probe conjugates. **Figure 16** shows a set of fluorescence emission spectra obtained from the successive washing of solution 8 with ethyl acetate (AcOEt) in order to remove free dye. It is worth mentioning that all solutions presented the same photophysical behaviour.

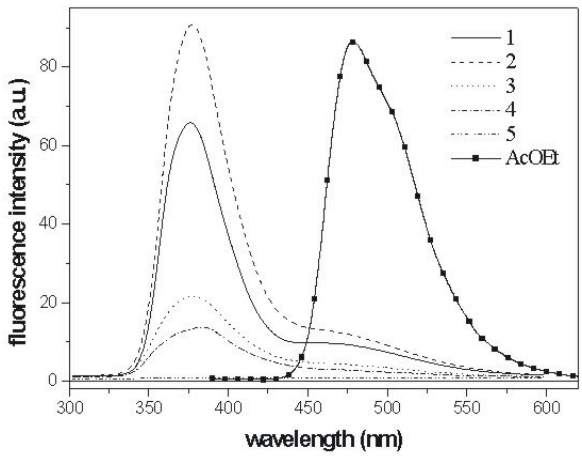

Figure 16. Fluorescence emission spectra of the organic layers obtained from solution 8, which was washed five times with ethyl acetate.

Since the fluorescence emission spectra was obtained from the organic layers, higher intensity located at higher wavelengths could be expected, due to the Excited State Intramolecular Proton Transfer (ESIPT) mechanism (**Arnaut and Formosinho, 1993; Formosinho and Arnaut, 1993**). However, a main emission band (378 nm) ascribed to the normal emission, blueshifted in relation to the ESIPT band (470 nm), was observed. This is due to the dye sensitivity, which indicates the presence of a small amount of aqueous NaOH in the organic layers. In a solution of freshly distilled AcOEt, the fluorescent dye presents one main band located at around 470 nm, as expected, in the absence of basic solution. As can also be seen in **Figure 16**, the fluorescence intensity for the first organic layer is lower than the second one, indicating fluorescence quenching due to the large amount of free dye removed in the first washing. The following organic layers show a decrease in the fluorescence intensity due to lower dye contents. The absence of fluorescence emission can be observed in the fifth washing step, indicating that all free dyes were removed.

Figure 17 depicts the fluorescence emission spectra of solutions obtained from supernatants 1, 2 and 3 after free dye extraction. In solution 1, all proteins are expected to be present. Due to the different protein solubilities, the NaOH solution extracted all the albumin and globulin (water and brine soluble) and a partial amount of glutelin and prolamin (alkali and ethanol soluble) from the slurry. According to the biuret test, it was possible to observe the presence of a significant amount of protein in solution 1, leading to a high protein–dye conjugate concentration.

This result corroborates with the low intensity emission band observed in **Figure 17**, due to fluorescence quenching, which refers to a process that decreases the fluorescence intensity of the sample. The photophysical behaviour observed in **Figure 17** is probably a quenching state between the dye and the quencher, which is the protein that has the highest concentration in solution, and this complex is non-fluorescent. In addition, the fluorescent probe seems to be in a hydrophobic environment, since the main band located at 475 nm is attributed to the ESIPT mechanism.

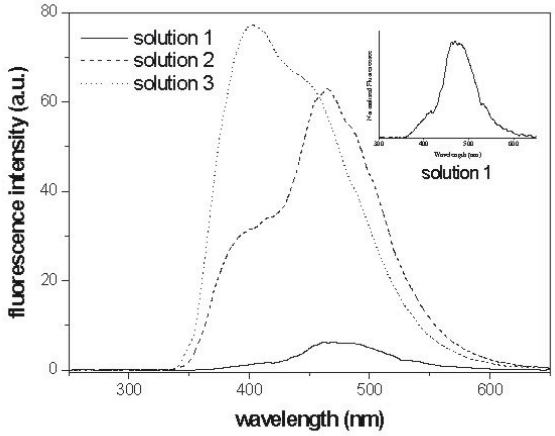

Figure 17. Fluorescence emission spectra of the solutions 1-3. The inset represents the amplified fluorescence emission spectra of solution 1.

In solution 2, due to the absence of albumin and globulin and the partial extraction of glutelin and prolamin in the first solution, the absence of fluorescence quenching gives a higher intensity. Depending on the protein, the dye will be constrained into two different environments. These correspond to a hydrophobic environment, as in the glutelin–dye conjugate, related to the ESIPT band of the dye (465 nm) and a hydrophilic environment, as in the prolamin–dye conjugate, related to the blue-shifted band (405 nm). The latter is ascribed to the normal relaxation of the dye (**Arnaut and Formosinho, 1993; Formosinho and Arnaut, 1993; Ríos and Ríos, 1998; Seo et al., 2005; Vollmer et al., 1994; Rodembusch et al., 2005a**).

In solution 3, a main band is observed at 402 nm, which is blueshifted in relation to the ESIPT band (443 nm). It indicates the same hydrophilic and hydrophobic environments observed in the previous step.

The relative amount of glutelin and prolamin in solutions 2 and 3 may also be evaluated, taking the band intensities into account. In solution 2, where glutelin is expected to be present in a large amount compared to prolamin, a ratio I_{ESIPT}/I_{normal} of 2.03 was determined.

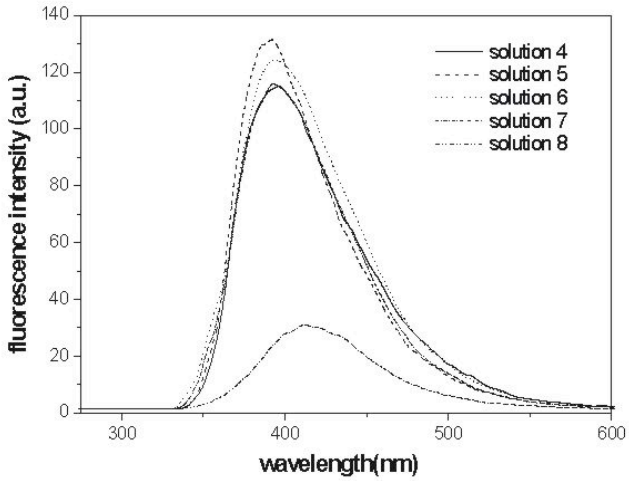

Figure 18. Fluorescence emission spectra of the fractions 4-8.

Since glutelin is more soluble in NaOH solutions, most of the protein was removed in solutions 1 and 2. Solution 3 presents an inversion of the band intensities, giving an intensity ratio I_{ESIPT}/I_{normal} of 0.86.

Figure 18 presents the fluorescence emission spectra of solutions 4–8. A main fluorescence emission band located between 394–412 nm is observed, related to the normal emission of the dye. The band located at 440 nm is not observed after solution 3, probably indicating that glutelin was totally removed at this point. Hence, contrary to the results of the biuret test, fluorescence emission indicates the presence of protein–dye conjugates even in the last solution from the alkaline extraction. It can be concluded that prolamin remains in solution, despite the alkaline treatment.

4.2. Morphology and structure of starch granules

Figure 19 shows SEM micrographs of six alkali-treated rice starches. In the picture corresponding to treatment 1 (**Figure 19a**), polyhedral starch granules are still connected to each other by proteins, making the observation of isolated granules difficult. Moreover, small protein particles, which have not been degraded by the alkaline treatment and that are also observed in native rice flour, can be seen.

After treatment 2 (**Figure 19b**), no protein particle was observed. However, starch granules are still generally connected. The presence of residual proteins was confirmed by fluorescence results. The images of the residues obtained after treatments 3 (**Figure 19c**) and 4 (**Figure 19d**) show more individualized granules. Their morphology and size (between 3 and 8 µm) are in agreement with the literature data (**Sodhi and Singh, 2003; Dang and Copeland, 2003; Qi et al., 2003; Wang and Wang, 2004**).

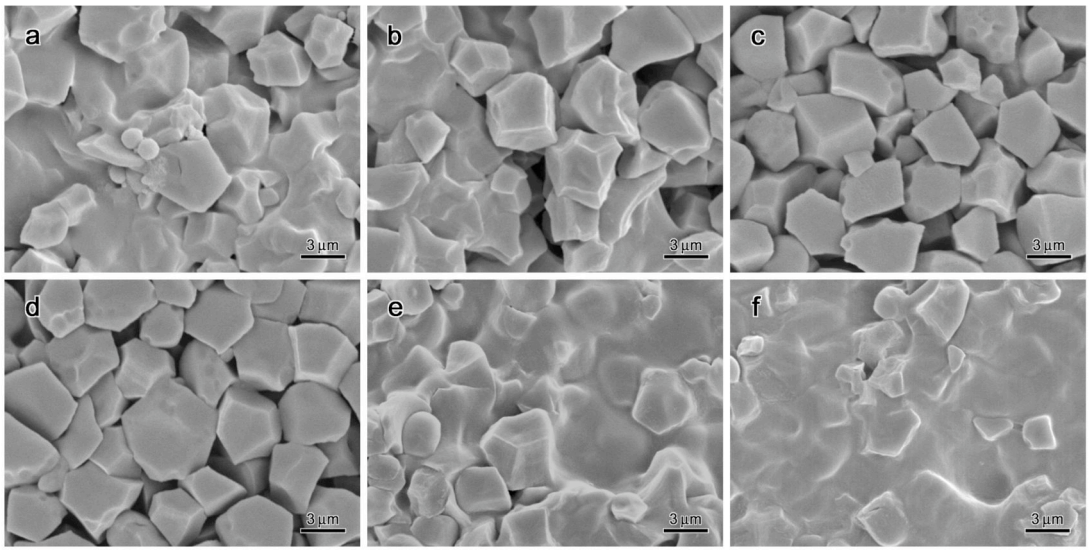

Figure 19. Scanning electron microscopy images of starches obtained after different alkaline treatments: treatment 1 (a) ; treatment 2 (b) ; treatment 3 (c) ; treatment 4 (d) ; treatment 5 (e) ; treatment 6 (f).

After treatment 5 (**Figure 19e**), isolated granules were rarely observed and the sample exhibited a gel-like aspect. The formation of a continuous film was even clearer after treatment 6 (**Figure 19f**). Thus, it appears that treatments with NaOH concentrations higher than 0.24% w/v result in a progressive loss of granular morphology, likely due to an alkaline gelatinization phenomenon.

The WAXS spectra of starch slurries obtained using different concentrations of NaOH are presented in **Figure 20**. The profile shown in **Figure 20a** was the same for the residues obtained after treatments 1, 2, 3 and 4. It corresponds to the diffraction pattern of A-starch, with reflections at 2θ=15.3°, 19.7° and 23.4°, and a doublet at 17.0° and 18.0°

(**Buléon et al., 1998**). However, the diffraction spectra of starches obtained after treatments 5 and 6 were different. After treatment 5 (**Figure 20b**), the intensity of all peaks slightly decreased, although the A-starch pattern could still be recognized. The effect of alkali was even more evident after treatment 6 (**Figure 20c**). The diffraction intensities decreased further and a single peak was now observed at 17.0°-18.0°.

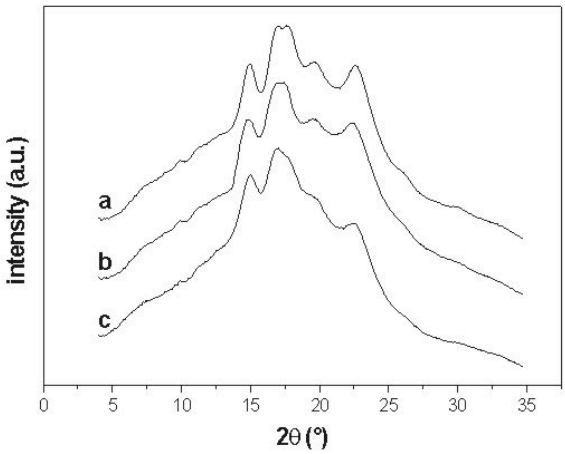

Figure 20. X-ray diffraction patterns of starch slurries: profiles recorded after treatments 1, 2, 3 and 4 (a), treatment 5 (b) and treatment 6 (c).

Sarko and Biloski (**1980**) reported the formation of a crystalline complex between starch and KOH which resulted in changes in the X-ray diffraction patterns. However, we did not observe any evidence of complex formation between starch and NaOH.

The intensity changes during treatments 5 and 6 are a direct consequence of the higher concentration of the alkaline solution. The swelling of the starch granules was drastically enhanced for NaOH concentrations higher than 0.20 mg/mL (**Cardoso et al., 2006; Singh et al., 2007**). Starch granules consist of alternating amorphous and crystalline regions, and gelatinization initially occurs in the amorphous regions. It was proposed that gelatinization was primarily driven by the swelling of the amorphous regions during water uptake (**Marchant and Blanshard, 1978; Donovan, 1979; French, 1984**). Thus, the changes in WAXS spectra for treatments 5 and 6 can be directly related to the swelling of starch and subsequent loss of crystallinity.

The evolution of WAXS spectra is particularly well correlated with the SEM observations. The decrease of crystallinity detected for treatments 5 and 6 is associated with the loss of the granular aspect of starch. However, the decrease of crystallinity deduced from the WAXS profiles (**Figures 20b** and **20c**) is not as high as would be expected from such a drastic change of morphology (**Figures 19e** and **19f**).

The modifications of starch properties were investigated using DSC. For all samples, a single endothermic transition was observed (**Figure 21**). It corresponds to the phase separation of amylose and amylopectin within the starch granules, the amylose leaching out of the granules (**Liu, Lelièvre, Ayoung, 1991; Fujita et al., 1992**).

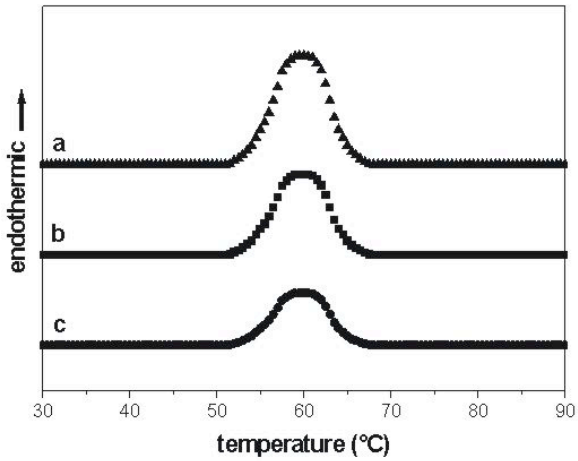

Figure 21. Differential scanning calorimetry patterns of starch slurries: profiles recorded after treatments 1, 2, 3 and 4 (a), treatment 5 (b) and treatment 6 (c).

The characteristic temperatures and enthalpies deduced from the thermograms are given in **Table 4**. During gelatinization, all samples presented similar onset (T_{onset}) and final temperatures (T_{end}). T_{onset} and T_{end} varied between 51.6-53.1°C and 66.2-68.4°C, respectively. No significant difference in maximal peak temperature (T_{peak}) was found for the six treatments.

The enthalpy of gelatinization ΔH is an indicator of the loss of molecular order within the granule that occurs upon gelatinization (**Cooke and Gidley, 1992; Hoover and Vasanthan, 1994; Tester and Morrison, 1990**). ΔH has been reported to be influenced by

the degree of crystallinity of starch (**Thirathumthavorn and Charoenrein, 2006**). In addition, it has been shown that starch granule size and shape, phosphorus content, amylopectin chain length and stability and/or size of crystalline regions also influenced the thermal properties of starch (**Stevens and Elton, 1971; Yuan et al., 1993; Noda et al., 1996; Singh and Singh, 2001; Singh et al., 2004; Wang et al., 2005**).

Table 4. DSC parameters obtained for the starches extracted with different NaOH concentrations. T_{onset} and T_{end} represent initial and final temperatures of the endothermic transition; T_{peak} is the maximal peak temperature and ΔH is the enthalpy of gelatinization. The values were obtained by triplicate average.

treatment	T_{onset} (°C)	T_{end} (°C)	T_{peak} (°C)	ΔH (cal/g)
1	51.6	68.0	58.9	1.2
2	52.1	66.2	59.1	1.1
3	53.1	67.1	59.6	1.2
4	52.9	68.2	59.2	1.1
5	52.2	66.3	58.6	0.8
6	52.4	68.4	59.4	0.6

After treatments 5 and 6, we observed a gradual decrease of enthalpy that cannot be related to the presence of different amounts of water in the samples, since they were equilibrated in a controlled atmosphere before analysis. This variation should be attributed to the internal modification of starch granules due to the action of NaOH during the extraction process. The rheological properties and gelatinization behavior of starch treated with concentrated NaOH solutions are changed, due to the dissociation of intermolecular hydrogen bonding in the amylopectin (**Tako and Hizukuri, 2002; Yamamoto et al., 2006**). The results of Donald et al. (**2001**) suggested that amylose diffuses into the amylopectin crystalline lamellae and disturbs its lamellar organization. The alkaline solution probably reduces the rigidity as well as the stability of the molecular organization of starch. Therefore, the mobility of the amylose chains is increased, which contributes to the loss of granule architecture. Our results thus show that when the starch is extracted using NaOH concentrations higher than 0.24% (w/v), the amorphous region is affected causing a partial disruption of the crystalline domains and reducing the crystallinity of starch granules.

4.3. Morphological and structural analyses during the alkaline starch extraction

4.3.1. The ultrastructure of starch during the extraction

Additionally to the concentration effect of NaOH solutions used in the alkaline extraction, an ultrastructural study was developed in order to understand the role played by the alkaline solution during the starch extraction. This study was conducted with NaOH solutions at 0.24% w/v (treatment 5) since this concentration is normally used as a standard during the alkaline extraction. Moreover, the use of this concentration allows comparing with the classical literature data.

Figure 22 shows the SAXS intensity profiles of slurries obtained from different steps of the starch isolation process performed with NaOH solutions at 0.24% w/v. A broad peak at $q \sim 0.06$ Å^{-1} is observed, which has been already described in the literature and is believed to arise from the alternating crystalline and amorphous lamellae of amylopectin. Since this peak is not seen from dry starch analysis, it implies that the electron density difference between amorphous and crystalline starch is not sufficient to give rise to a similar pattern from the dry material. On the other hand, in hydrated starch the resulting electron density difference is due to a preferential absorption of water into the amorphous regions within the structure (**Cameron and Donald, 1992; Cameron and Donald, 1993**). The peak achieves its maximum at q = 0,063 Å^{-1} corresponding to a 9-10 nm lamellar repeat. The value is in agreement with the data in the literature (**Cameron and Donald, 1992; Cameron and Donald, 1993**).

Figure 23 depicts the OM results, using polarized (left) and non-polarized light (right), for the same fractions of slurry starches analyzed by SAXS. Comparing the images, it can be observed that the aggregation of starch granules progressively decreased upon the alkaline treatment.

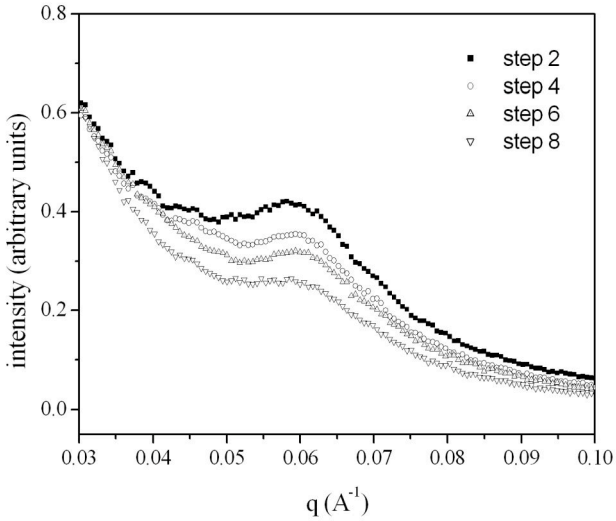

Figure 22. Small-angle X-ray scattering profiles of the slurry starches obtained during the steps 2, 4, 6 and 8 at treatment 5.

The comparison between polarized and non-polarized light microscopy images of samples at the same step of treatment reveals the existence of extinction domains in some birefringent granules. Hence, the alkaline treatment may cause the significant loss of the birefringence observed from step 6. Until recently, the peak at $q \approx 0.06$ Å^{-1} has been interpreted in terms of Bragg diffraction.

However, taking the intensity profile as a whole, rather than only the peak position, additional information about the lamellar structure of starch was obtained. **Figure 22** shows a decrease in peak intensity as the starch extraction proceeds. Cameron and Donald (**1992**) have explained that changes in the SAXS intensity have their origin in two different events due to the fact that the semicrystalline material consists of amorphous and crystalline repetitions of amylopectin. The first possibility is interpreted in terms of preferential water absorption into the amorphous regions, lowering their electron density. The preferential absorption of water into the amorphous regions is known to increase the contrast between amorphous and crystalline lamellae and consequently increases the SAXS profile. The other possibility occurs when the crystalline lamellae are disrupted, lowering the contrast between them and the amorphous lamellae. Thus, the absolute intensity of the peak is lowered, falling to a value below that of native starch.

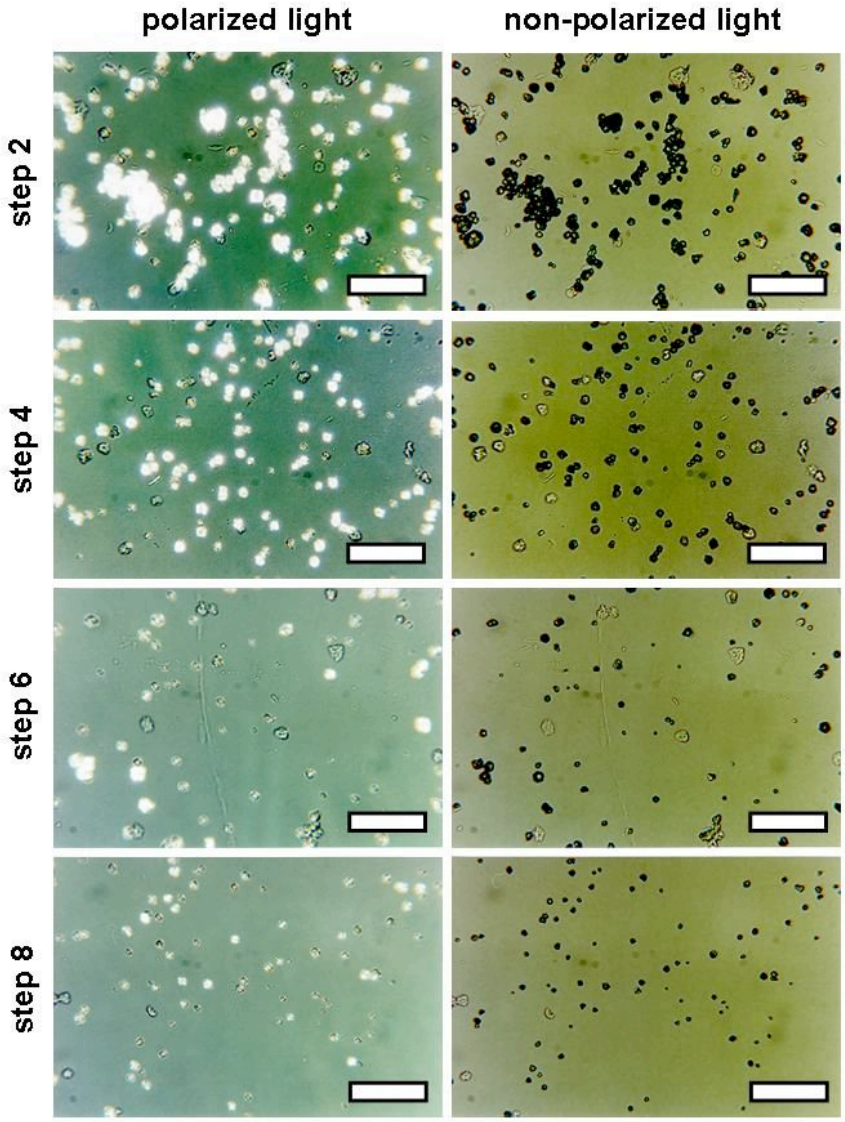

Figure 23. Polarized light (left) and non-polarized light (right) micrographs of the slurry starches obtained in steps 2, 4, 6 and 8 (scale bars: 25 μm).

These facts suggest that during the starch alkaline extraction, the reduction in the peak intensity (**Figure 22**) is related to a disruption of the crystalline lamellae, leading to amorphization. Depending on the amorphization degree, the starch can be gelatinized (**Tako and Hizukuri, 2002**). However, after completing gelatinization the crystalline lamellae are totally disrupted and the order cannot be visible using SAXS.

As in **Figure 22** the SAXS intensity is reduced while the order remains, this process is interpreted as the partial amorphization of the system. Thus, the possibility of total alkaline gelatinization is discarded.

The *q* value of the peak remained practically unchanged throughout alkaline treatment, indicating that the lamellar repeat distance did not change with the partial amorphization.

The disruption of the crystalline lamellae can be associated with the birefringence end point (**Mistry and Eckhoff, 1992a**) and with the reduction on SAXS intensity profile (**Cameron, Donald, 1993**). Tako and Hizukuri (**2002**) associated the dissociation of hydrogen bonding of the amylopectin to the washing procedure with NaOH. Since the starch isolation from rice is more difficult than isolation of starch from corn or wheat, a higher number of washing procedures is required when using alkaline solutions. Thus, the higher contact time between sodium hydroxide and the starch granules contributes to swelling in the amorphous regions imposes a stress upon the amylopectin crystallites, causing the dissociation of hydrogen bonds (**Tako and Hizukuri, 2002**) and a weakening of the amylopectin double helices which results in a crystallinity reduction. Furthermore, these bonds maintain the crystallinity in the lamellae and when they are broken during the alkaline treatment, the lamellar order is gradually disrupted. It is demonstrated by the reduction in the SAXS intensity and birefringence from step 6. Additionally to this, the changes in WAXS spectrum for treatment 5, in the section **4.2.**, can corroborate this interpretation. The intensity of all WAXS peaks was slightly decreased when the alkaline extraction was conducted with NaOH solution at 0.24% w/v. Thus, the subsequent reductions of SAXS and WAXS intensities are, respectivelly, results of the swelling of starch and loss of crystallinity.

4.3.2. The morphology of supercritically dried treated starch

In order to study the effect of drying for the slurry starch obtained from treatment 5, the specimen was supercritically dried and analysed by SEM and Mie scattering. Thus, the results can be compared with the earlier ones presented in the section **4.2**.

Figure 24 shows SEM micrographs of treated starches demonstrating the presence of mainly polyhedral starch granules.

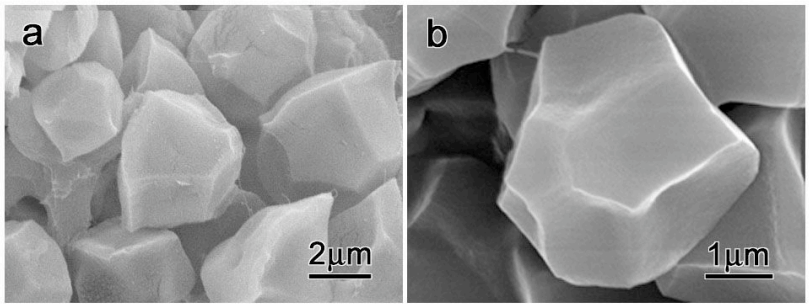

Figure 24. Scanning electron microscopy of supercritically dried rice starch granules. (a) general view. (b) an isolated starch granule viewed at a higher magnification.

Their shape as well as their average size, in the order of 3-8 μm, are in agreement with previously reported results (**Sodhi and Singh, 2003; Dang and Copeland, 2003; Qi et al., 2003; Wang and Wang, 2004**). In **Figure 24a**, isolated starch granules are observed, indicating that proteins were successfully removed. This result is in agreement with the UV-vis and fluorescence analysis (section **4.1.**). **Figure 24b** depicts just one intact rice starch granule. When the starch is supercritically dried the external structure is not affected by the treatment with NaOH since it was not possible to verify significant differences in morphology or size among different granules. However, when the same granule suspension was allowed to dry onto copper stubs, isolated granules were rarely observed and, moreover, the sample presented a gel-like aspect. Thus the drying of the sample presents an important role in the morphology analysis. According to WAXS and SAXS results (sections **4.2.** and **4.3.1.**, respectively), the swelling of ultrastructure and loss of crystallinity reduce the firmness of the granules. The starch obtained from treatment 5 presents a weak internal starch structure. The specimen dried onto copper stubs lost its form and during the drying the sample changed from granular state to gel-like aspect. In contrast to this, when the sample was supercritically dried the granular structure was kept. Hence, the supercritically drying can keep the starch granule form even if the internal structure is damaged.

Additional information about the size distribution of the supercritically dried granules was obtained by Mie scattering. Through a single measurement performed with the

starch granules suspended in water, it was possible to evaluate the granules size distribution (**Sevenou et al. 2002; Nayouf et al., 2003; Morelon et al., 2005**). **Figure 25** shows a bimodal distribution (logarithmic scale).

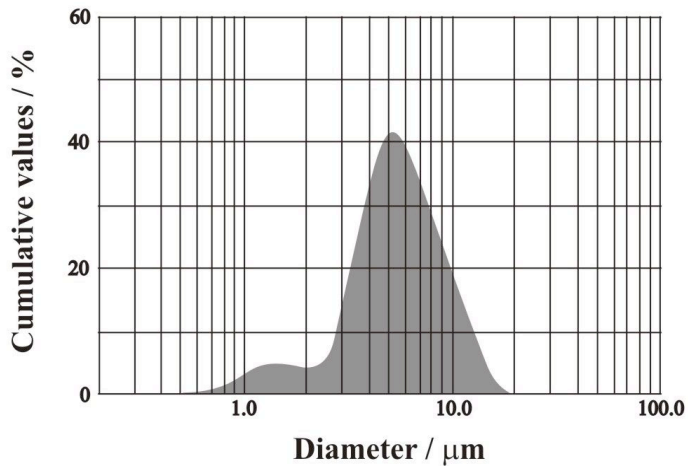

Figure 25. Size distribution of rice starch obtained by Mie scattering.

The main population, accounting for 96% of the sample, gave an average size of 5.3 μm, which is in accordance with the values obtained by SEM (**Figure 24**). The other population, representing around 4% of the sample, gave an average size of 1.0 μm, which may be attributed to smaller granule fragments formed during the treatment or alkali-resistant impurities in the sample. Thus, it is possible to observe that the supercritically dry starch did not change the average size of the granules. Moreover, the starch when redispersed in water kept their granular form.

CHAPTER 5

LIGHT SCATTERING OF AQUEOUS AMYLOSE SOLUTIONS

Light scattering (LS) was used in order to analyse the behavior of aqueous amylose solutions. Two different amyloses were investigated: amylose extracted from BR-IRGA 410 rice starch and commercial amylose from Sigma.

The results obtained with the amylose extracted from BR-IRGA rice starch are presented below. After extraction, amylose was submitted to gel filtration chromatography and 14 fractions (from *f*5 to *f*18) were collected and analysed without previous filtration. **Figure 26** shows typical ACFs obtained from dynamic light scattering measurements on dilute solutions of the fraction *f*11.

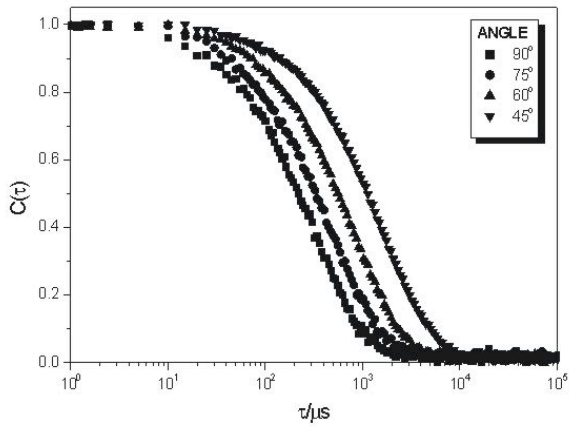

Figure 26. Autocorrelation functions obtained from fraction *f*11, at 25°C in different angles (from right to left: 45°, 60°, 75° and 90°).

As expected, the ACFs appeared to decay slightly faster as the detecting angle increased. In all ACFs, one characteristic decay was observed, related to the translational diffusion coefficient (D_T). Using **equations 5, 6** and **7** (section **3.2.2**), the apparent hydrodynamic radius (R_{app}) were calculated and **Figure 27** shows their typical angular dependence. The extrapolation to angle 0º in **Figure 27,** generates the hydrodynamic radius R_h of 73.0 (±2) nm. **Table 5** presents R_h values for the different amylose fractions in this work. As it was foreseen, the respective R_h values decrease as a function of the fraction eluted, since for the first fractions, the highest molecular weights are expected to be eluted.

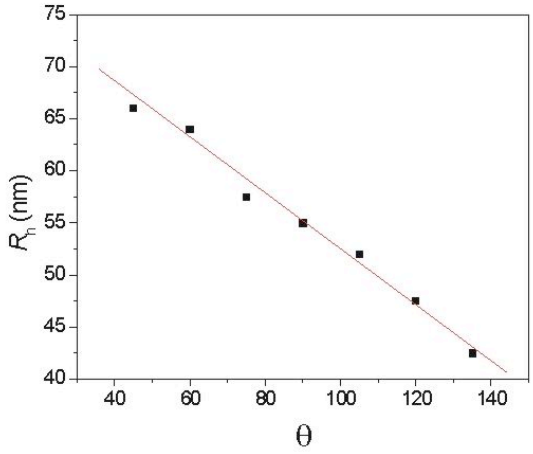

Figure 27. Rh as a function of θ for amylose obtained in the *f*8 fraction during the gel filtration chromatography.

Figure 28 shows the relationship between the relaxation rate (Γ) and the square of the scattering vector (q^2) for *f*8, *f*11 and *f*18 fractions. The slope of the curves in **Figure 28** leads to the diffusion coefficient D_T, using **equation 6**. For each fraction it was possible to observe a different slope and, as the elution volume increases, D_T becomes larger. The non-linear dependence in the plot Γ x q^2 was assumed as an indication of the amylose contamination, a consequence of the extraction procedure. For *f* > *f*10, Γ is linearly dependent on q^2, and the extrapolation of Γ to $q_{\rightarrow 0}$ passes by the origin, clearly indicating that the fast relaxation is related to the chain diffusion. However, until *f*10 fraction the results were contrary to the other ones. It was assumed in this work that this dependence is a consequence of the sample contamination with amylopectin.

Table 5. R_g, R_h, ρ, and M_w for the amylose fractions.

fraction	R_h (nm)	R_g (nm)	ρ	Mw (g/mol)
*f*6	120	84	0.70	1.6×10^6
*f*8	73	64	0.86	9.5×10^5
*f*11	53	45	0.84	4.6×10^5
*f*13	54	44	0.82	4.6×10^5
*f*16	52	44	0.84	4.3×10^5
*f*18	40	32	0.80	2.7×10^5

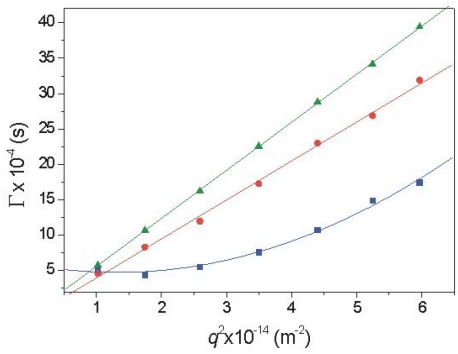

Figure 28. Relaxation mode (Γ) as a function of the scattering vector (q^2).
(■) *f*6; (•) *f*11 and (▲) *f*18 fractions.

During the gel filtration chromatography, aliquots of 1 mL were collected. Thus, the solutions presented unknown amylose concentration due to dilution. Moreover, the weak signal-to-noise ratio of amylose fractions made impracticable a Zimm plot construction. Hence, the dissymmetry method (**equation 4**) was chosen in order to estimate the radius of gyration R_g for all amylose fractions, as depicted in **Figure 29** for the fraction *f11*. The obtained R_g values are presented in **Table 5**.

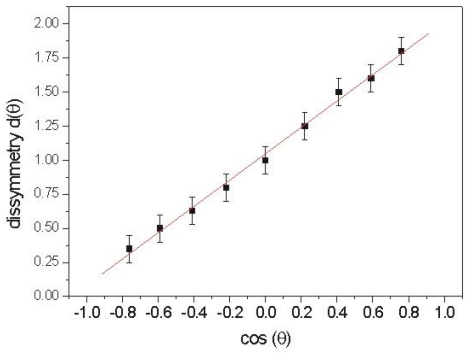

Figure 29. Plot of dissymmetry d(θ) vs. cos (θ) for the *f*11 fraction.

Taking the R_g values, between 32 and 84 nm, the molecular weight (M_w) was calculated according to **equation 10**, using K_v = 2.71 x 10^{-22} m^2.mol/g and v = 1.13 in 0.1 M KOH (**Roger et al., 1999**) :

$$<R_g^2>_z = K_v<M_w>^v \quad (10)$$

The relation between R_g and M_w is presented in **Figure 30**, as a function of the elution volumes collected during the gel filtration chromatography. High R_g (and M_w) values were essentially observed up to an elution volume of 10 mL. Then, the values remained quasi-constant and, for elution volumes higher than 16 mL, R_g and M_w decreased to 32 nm and 2.7 x 10^5 g/mol, respectively.

The values of R_g and R_h are important data. However, when presented separately they supply no information about the structure of the amylose chains in solution. As the static and hydrodynamic dimensions vary characteristically with the structure of the macromolecules, a combination of the two may provide qualitative information on their architecture (**Burchard and Richtering, 1989**). The structure-sensitive parameter ρ is defined as the ratio of radius of gyration R_g obtained from static light scattering to the hydrodynamic radius R_h obtained from dynamic light scattering. The ρ values for different molecular architectures can be found in the literature (**Burchard, 1994**). Generally, ρ decreases with increasing branching density, but an increase in polydispersity counteracts the effect of branching. At 25°C, ρ was found to be between 0.70 and 0.86 (**Table 5**) for the different amylose solutions. This values approach what is predicted for a homogeneous sphere (0.788). The obtained values of ρ for the amylose in this work are in accord to those obtained by Roger and Colonna (**1996**) for amylose isolated using thymol.

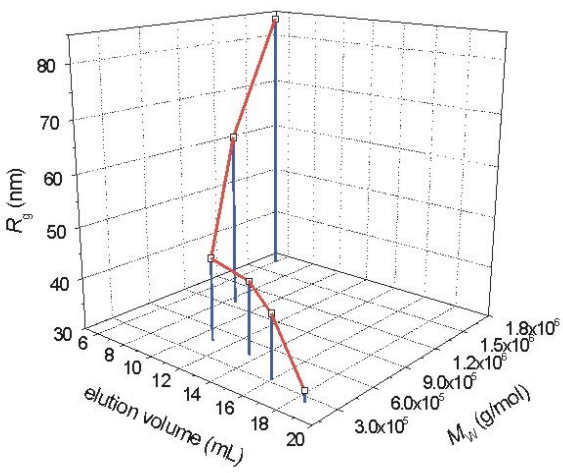

Figure 30. Relationship between apparent radius of gyration (R_g), elution volume and molecular weight (M_w) of rice starch amylose.

However, in the same work, these authors reported that ρ values changed of approximately 2.8 when the same sample was submitted to ultracentifugation. Amylopectin and normal corn starch present ρ values between 1.0 and 1.3, which are characteristic of branched structures. It was also reported that for randomly polysaccharide branched systems, where the ρ parameter remains constant, around 0.9 (**Galinsky and Burchard, 1995**). Bello-Perez et al. (**1998b**) showed that when granular starch lost its structure and the amylose and amylopectin remain dissolved, ρ values are observed to be between 0.80 and 0.90. These values are considered to be typical for spheres or other globular structures. Thus, the ρ values obtained in this work are in agreement with the literature data from starch granules dissolved in alkaline solution. Following the tendency of ρ values, the studied samples in this work were probably contamined with amylopectin. In this way, we are assuming that the high R_g as well as the ρ values estimate for our samples indicate that the amylose was probably not efficiently separated from amylopectin. Hence, the dissymmetry method was not appropriate for radius measurement and consequently, a spheric shape was detected for all amylose fractions. A clear deviation in the radius behavior was observed until the fraction *f*10 (**Figure 30**) probably due to the presence of amylopectin (**Yang et al., 2006**). Although after *f*10 it is doubtful to attribute the ρ values to amylopectin contamination we may assume that applying the thymol complexation followed by gel filtration chromatography the amylose/amylopectin separation was not efficiently performed.

In order to study amylose in varying ionic strength as a function of the storage time, the light scattering study was performed using commercial amylose. Amylose M_w value was obtained in NaOH solutions from Zimm plot procedure being 1.7×10^5 (± 5%) g/mol. **Figure 31** shows the behavior of R_h and R_g under the influence of KOH, stored at different times. In the alkaline medium, the measurements were done in the concentration range of 0.8 - 1.4 M KOH. The scattering analyses of unstored samples were performed immediately after sample preparation. No significant variation on R_h was observed as a function of the KOH concentrations for unstored samples. Thus, the alkali concentration seems to have no

influence on the chain behavior in solution by changing the alkali concentration. Instead of, a general trend is observed when the solutions were stocked. A R_h reduction was verified as a function of time for all samples. Moreover, an increase of R_h values was observed increasing the KOH concentration for a same storage time. The R_g values were also concentration independent in unstored samples. However, when samples are stored, it was observed a slight R_g reduction for shorter storage times. Then, the values increase again for larger storage times. Hence, the storage time seems to play an important role in the amylose structure in solution.

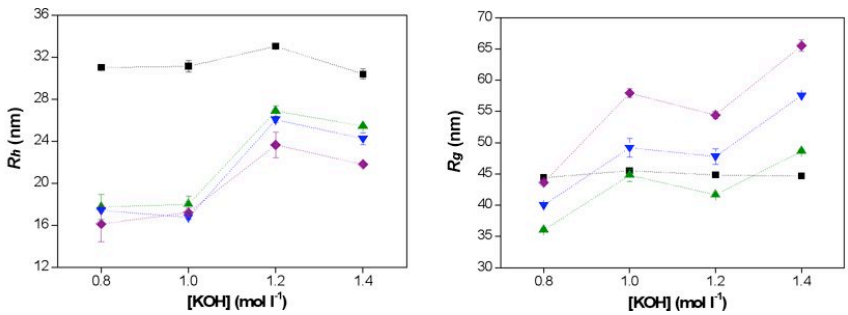

Figure 31. Influence of the KOH concentration in the R_h (left) and R_g (right) values of amylose solutions stored for different times: ■ unstored; ▲ 3 days; ▼ 5 days and ♦ 7 days.

The *r* parameter increases with the storage times for all concentrations, from approximately 1.4 to 2.9, suggesting an increase in the chain polydispersity (**Table 6**). Most of the –OH groups in the anhydrous glucose units are ionized at high pH (12.5), so agglomeration of amylose chains and paste retrogradation can be avoid (**Suortti et al., 1998**). It can be concluded that the alkali can affect the structure and physical behavior of amylose in solution. In spite of this, a molecular degradation could be accelerated by alkali dissolution (**Han and Lim, 2004**).

Table 6. ρ factor at different storage times in KOH solutions.

[KOH]	unstored	3 days	5 days	7 days
0.8	1.43	2.03	2.29	2.70
1.0	1.46	2.48	2.93	3.16
1.2	1.36	1.55	1.83	2.60
1.4	1.47	1.91	2.37	2.98

In order to study the ionic strength effect during amylose storage in salt solution, alkaline amylose solutions were initially neutralized with HCl to produce a neutral solution. Thus, the basic solution responsible for amylose solubilization was substituted by a neutral solution and the ionic strength effect could be followed.

Figure 32 depicts the influence of the KCl concentration in the R_h and R_g values of amylose chains stored at different times.

Following the same behavior presented in alkaline solutions, the unstored samples did not show significant differences in R_h values as a function of the increasing KCl concentration and they were smaller than those measured in KOH. It was expected since the radius of gyration of corn amylose in alkaline solution was high when compared with the values obtained in water or in DMSO (**Nakanishi et al. 1993; Roger et al. 1996**).

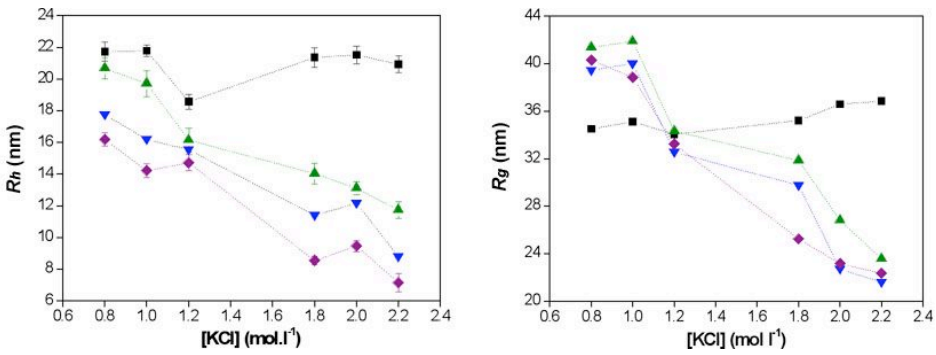

Figure 32. Influence of the KCl concentration in the R_h (left) and R_g (right) values of amylose chains stored for different times: ■ unstored; ▲ 3 days; ▼ 5 days and ♦ 7 days.

In an aqueous neutral solution, amylose chains were reported to exist as a helical conformation, but by adding alkali, the hydrogen bonds stabilizing the structure are progressively destroyed and the amylose chains adopt a more random conformation. At pH 12, the helical conformation was supposed to be completely absent (**Banks and Greenwood, 1972**). Moreover, increasing KOH, a progressive increase in the negative charge on the polymers induces a charge repulsion between chains, increasing the radius of gyration (**Foster, 1965**). As a consequence, the stored samples presented a reduction in R_h values when KCl concentration and storage time were increased. The R_g values measured in

KCl depicted an inverse profile when compared to those obtained for the amylose chains stored in KOH. The highest R_g values in KCl were observed for the smaller salt concentrations (< 1.2 M). A special feature of amylose in KCl was observed when KCl 1.2 M was used, since practically no change in R_g was observed during a storage time of 7 days. This fact suggests a good condition for amylose stabilization by KCl 1.2M, due to an electrostatic stability between the chains and the solvent medium. In this way, due to charge equilibration, the amylose dimension remains unchanged.

The values of the structure-sensitive parameter ρ for the amylose in KCl are given in **Table 7**. This dimensionless ratio increases with the storage time for all concentrations, suggesting an increase in the amylose polydispersity (**Table 7**). The increase in ρ obeys the same behavior as in KOH, being slightly higher. Therefore, the structural changes evidenced from ρ were the same, independent of the solvent. Bello-Perez et al. (**1998b**) reported the same effect for the ρ values during the storage time of amylose in KCl, showing an expected variation in the structure when the storage time increases.

Table 7. ρ factor at different storage times in KCl solutions.

[KCl]	unstored	3 days	5 days	7 days
0.8	1.99	2.00	2.22	2.49
1.0	1.61	2.12	2.47	2.73
1.2	1.83	2.12	2.09	2.26
1.8	1.65	2.27	2.61	2.95
2.0	1.70	1.99	1.69	2.45
2.2	1.76	2.01	2.25	3.12

Moreover, Roger and Colonna (**1996**) reported that ρ values for the stored amylose in the same ionic strength condition change of approximately 2.8 when in the absence of contaminants. These results are similar to those given in **Table 7** for the samples in this work. Bello-Perez et al. (**1998b**) found a different behavior for the relaxation rate distribution of the samples due to changes in the internal structure when storage time in KCl

increase. These authors correlated the diminution in R_h and higher storage time with sample depolymerization, since the peak position of the principal component was slightly changed at higher log τ values for the longest storage times. However, in our systems, the secondary modes in the relaxation time distribution were absent, so depolymerization was excluded.

In order to verify the possible degradation of amylose chains during the storage time in KCl, the Benedict's test for glucose was carried out (**Paixao et al. 2003; Quintino et al. 2005**). Benedict's solution is used for checking a reducing sugar presence. If the sample contains the reducing sugar, the solution will give a red precipitate of cuprous oxide, which is then called a positive test. **Figure 33** shows a partial result of a Benedict's test. In the bottle (a) and (b) no significant difference was observed when the colors were compared. However, the solutions in bottles (a) and (b) are the pure Benedict's solution and KCl 2.2 M amylose solution stored for 7 days after the Benedict's test, respectively. The color observed in bottle (b) indicates the absence of glucose (monomer) in the sample. The red/brown color observed in glucose solutions (c and d) was not present in any amylose samples. The blue color maintained in amylose solutions (b) was a negative test for the presence of glucose in all neutral and alkaline amylose solutions. In this way, as the secondary modes in the distribution of the relaxation times were absent and the Benedict's test performed in the amylose solutions results negative, the changes in the chain dimension during the experiments have not its origin in amylose depolymerization. Hence, the evidences observed are linked to the stabilization of the polymer chains during storage.

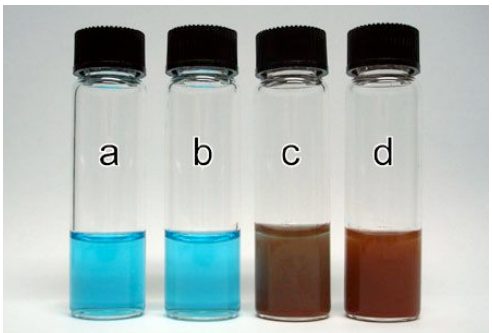

Figure 33. Benedict's test performed to verify the existence of glucose presence.
a) Benedict's solution (blank); b) KCl 2.2 M amylose solution stored for 7 days;
c) 1 mg/mL and d) 0.5 mg/mL glucose standard solutions.

As a general rule, KOH is a friendly solvent for amylose and the observed R_g increment by KOH concentration increase is related to a good solubility of the polymer. The opposite behavior observed in KCl is probably related with a polymer-polymer interaction preferentially over those of polymer-solvent, through hydrogen bonding and the decrease of the electrostatic repulsion by salt screening effect (**Cho et al. 2006**). Artificial apparent decreases in macromolecule size with salt concentration are possible if increasing salt content reduces colloidal stability and leads to coagulation. This possibility was discounted due to the stability of the DLS measurement in the amylose solutions stored at 7 days at high salt concentrations and the fact that the same chain diameters were detected. This high degree of reproducibility was seen in all systems.

Chiou et al. (**2005**) using rice starch observed that when the salt concentration was increased, the hydrodynamic diameter increased for all starches. The system was extremely dilute and thus it was highly unlikely that the observed changes were due to crystallisation. In addition to this, these authors tested the stability over time and the samples were found to be stable for at least 30 min. When kept overnight at room temperature, the samples showed different sizes as inferred from DLS. However, re-measurements after brief sonication gave a DLS diameter within the range of values obtained on the previous day. Since purified starch was used, the change in hydrodynamic diameters was due solely to the expansion or contraction of chains of amylose and amylopectin, and not attributable to a protein or lipid component. The data suggested that the expansion behaviour is sensitive to the branching structure as well as to the distribution of the branch lengths. In this way, the results presented in **Figure 32** for the samples in this work are contradictory to the related by Chiou et al. (**2005**). However, in our system pure synthetic amylose was studied, in opposite to starch, a mixture of amylose and amylopectin. Moreover, the comparison between the systems is pertinent to understand the different behaviour of the solutions. The discrepancies in the hydrodynamic characteristics of both studied systems can be attributed to the composition of the solutions.

Thus, the presence of amylopectin changes the profile referring to chain expansion or contraction in salt solutions during storage. The low solubility of amylose in salt solutions results in a reduction of R_h while, while for a mixture of amylose and amylopectin, an increase is observed. According to this fact, we assume that the hydrodynamic behaviour observed in the mixture of both polymers is attributed to an expansion of the amylopectin chains. As no secondary modes in the distribution of the relaxation times were observed for starch solutions, the contribution of amylose is present in a large spectral band of these polysaccharides. The amylose behavior in salt solutions was incorporated in the amylopectin scattering since this polymer is the major component of starch and its R_h is higher than amylose. Moreover, no longer storage times were investigated for Chiou et al. (**2005**), thus the contraction of amylose is not expected to appear as a distribution of relaxation time.

However, it is believed that a slow amylose-solvent equilibrium begins since until the 7th day a small change in the radius was observed without amylose depolymerization. Even presenting the same chemical structure, amylopectin and amylose have different hydrodynamic characteristics. As the amylopectin presents a higher solubilty than amylose in water solutions, probably, amylopectin molecules are less susceptible to fast radius changes originated from solvent aqueous medium. This hypotesis explains the slow hydrodynamic variations of pure amylose in this work. This fact is clearly observed since, practically, no change was measured for the radius in the unstored amylose samples. In addition, this result for the unstored samples was independent of the alkaline or salt solution used during the experiments. In this way, the amylose does not change its radius instantaneously according to the medium. A delay was verified between amylose stabilization in the alkaline medium and in the salt solutions. Curiously, in 1.2 M KCl solutions, the effect of storage time was not observed. This solution probably stabilizes amylose playing as a colloidal stabilizer. The balance of charges between amylose and solvent is an ideal situation for the amylose in coil structure. As observed in R_g for the amylose in 1.2M KCl solution, no change during the storage time suggest a type of ideal condition for the amylose during the storage time without radius variation.

CHAPTER 6

V AMYLOSE SINGLE CRYSTALS

6.1. $V_{isopropanol}$ crystals

Groups of single crystals prepared from dilute solutions of amylose complexed with isopropanol, dried on the carbon film and observed at room temperature, are shown in the image of **Figure 34A**. The crystals are lamellae with a clear rectangular shape. The crystals are often organized in flower-like aggregates, suggesting that several rectangular crystals initially outgrow from a unique nucleus. Each platelet was about 2-3 μm long and 0.5 μm wide. The more compact regions of superimposed crystals often exhibit cracks, some of them propagating parallel to the long dimension of the outgrowing crystals. These cracks, probably due to drying strain, have already been described by Buléon et al. (**Buléon et al., 1990**). **Figure 34B** shows $V_{isopropanol}$ crystals shadowed with W/Ta. This beam-resistant metallic layer allows to observe the crystals at a higher magnification. The superimposition of thin lamellae is clearly seen, some of them exhibiting an irregular edges, probably due to a heterogeneous our incomplete crystallization or a degradation during drying. The V-amylose crystals complexed with linalool are also elongated rectangular lamellae, growing as crowded flower-like aggregates (**Figure 35**). Individual crystals are rarely seen. This may be due to a lower number of nuclei formed during crystallization.

When the complexing agent (isopropanol or linalool) is dispersed in the metastable amylose phase, the coexisting two phases are not at thermodynamic equilibrium. Thus, in our case, the complex solubility degree probably leads to different mechanism of thermodynamic equilibrium since isopropanol is water-soluble while linalool presents a low solubility in water. Especially in the linalool crystallization, the interface formed between two liquid phases as well as the probable low amount of nuclei available for the crystallization leads to a higher overgrowth of lamellae as a consequence of heterogeneous nucleation (**Sirota, 2007**). Abe et al. (**2005**) suggested that crystals are developed on the folding surface of the lamellae. This fact allows understanding the aggregation tendency of the crystals and the inexistence of individual lamellae.

Crowded flower-like aggregates of crystals were formed during the crystallization with isopropanol and linalool. As we wanted to promote the formation of individual lamellae, the crystallization protocol was changed. We used different commercial and synthetic fractions of amylose with varying DP. We also tried different solubilization temperatures. No alteration in the morphology, aggregation or size of the crystals were observed when these parameters were changed. However, significant alterations were verified when the filtration procedure was performed after amylose and isopropanol mixing. Beyond the superposition of lamellar crystals presented in **Figures 34** and **35**, hexagonal single crystals (corresponding to V_H crystals) are observed serving as a nucleation point for the $V_{isopropanol}$ aggregates.

The corresponding electron diffraction patterns recorded from individual crystals were similar for both complexes (**Figure 36B**). Moreover, all resembled those recorded by Buléon et al. (**Buléon et al., 1990**) and Nuesslli et al. (**Nuessli et al., 2000**) from elongated lamellar crystals prepared in presence of isopropanol, fenchone, menthone, and geraniol. Slight variations in relative intensity could be observed for selected reflections. This diagram contains around 250 spots symmetrically distributed in 4 quadrants with symmetry axes *a* and *b* aligned along and perpendicular to the long side of the platelet, respectively.

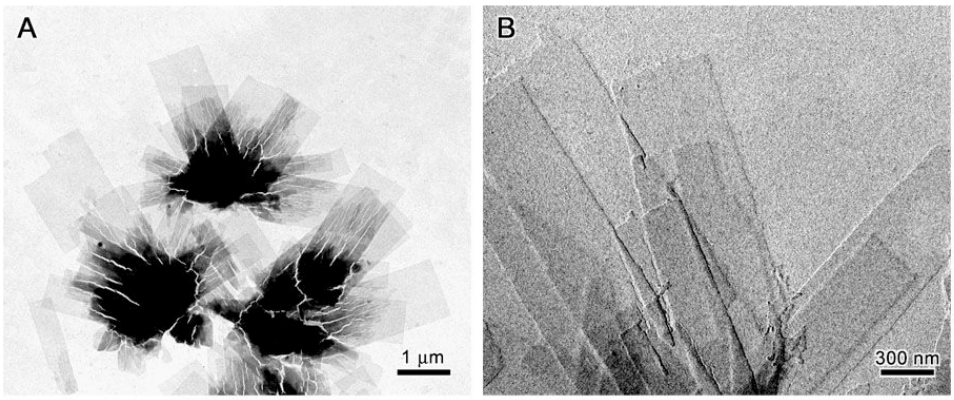

Figure 34. TEM images of lamellar single crystals of V amylose complexed with isopropanol. **A**: crystals taken immediately after crystallization. **B**: crystals shadowed with W/Ta.

As along the *a** and *b** axes, only even order reflections are present (**Figure 36C**), a p_{gg} symmetry is suggested for the diagram and therefore for the corresponding projection of the crystalline structure.

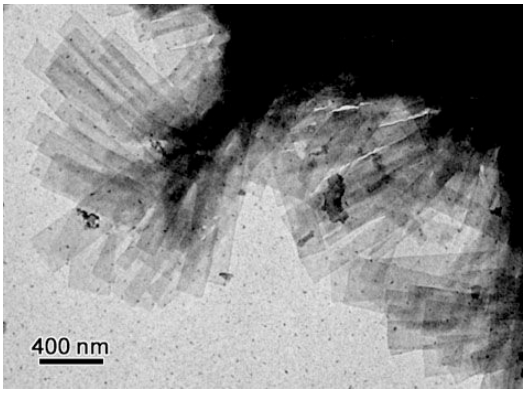

Figure 35. TEM image of lamellar single crystals of V amylose complexed with linalool.

The reflections can thus be indexed according to the orthorhombic space groups $P2_12_12_1$ or $P2_12_12$ (an ambiguity remains along ***c*** which is either a 2_1 or a 2 axis), as proposed by Buléon et al. (**Buléon et al., 1990**). The list of observed electron diffraction spots, together with indexation and corresponding *d*-spacings is presented in **Annex 1**. The unit cell parameters were calculated using a least-square refinement program from a dataset recorded at low temperature. As the crystals are often organized in flower-like aggregates, individual crystals are rarely seen.

Contrary to $V_{linalool}$ complexes, V_H electron diffraction diagrams were recorded from $V_{isopropanol}$ crystals when they were observed at room temperature. As already reported, this phenomenon is due to the evaporation of isopropanol in the vacuum of the microscope (**Manley, 1964; Buléon et al., 1990; Helbert and Chanzy, 1994**). Consequently, we had to quench-freeze the specimens in liquid nitrogen before the insertion in the microscope. In order to know the symmetry of the three-dimensional structure, diffraction patterns must be recorded from $V_{isopropanol}$ crystals tilted about selected reciprocal

axes. Using the cryo-holder, it was not possible to rotate the specimens before tilting. We had to select the crystals that were approximately properly oriented and they were then tilted about the main reciprocal axes. However, the precision of the initial orientation is critical and, due to small amounts of isolated $V_{isopropanol}$ lamellae, it was difficult to record symmetrical diffractions. Consequently, the *c** (chain axis) could not be calculated. Only base plane electron diffraction diagrams containing *hk0* reflections were collected at liquid nitrogen temperature on crystals perpendicular to the electron beam. After calibration, we calculated the unit cell parameters *a*=2.830 (±0.005) nm and *b*=2.950 (±0.005) nm. These values are similar to those reported in literature for single crystals of V amylose complexed with isopropanol (**Buléon et al., 1990**), geraniol, menthone and fenchone (**Nuessli et al., 2000**).

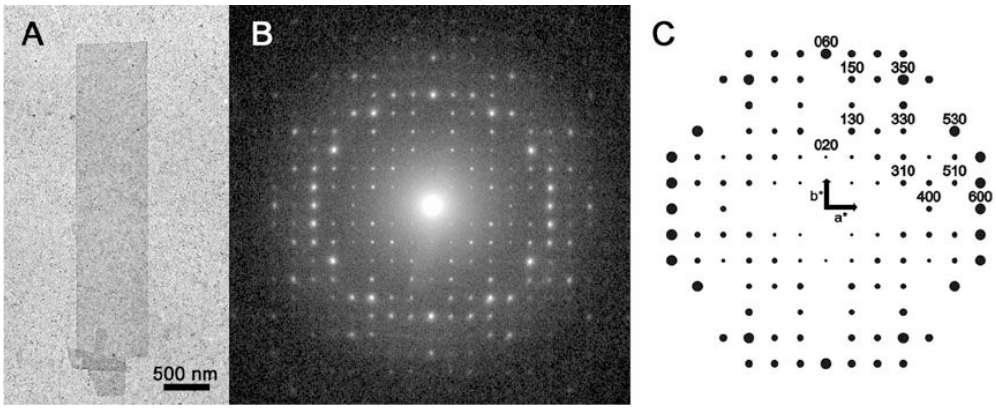

Figure 36. A) TEM image of a $V_{isopropanol}$ single crystal ; **B)** corresponding base plane electron diffraction pattern correctly oriented with respect to the crystal in **A** ; **C)** indexation of the pattern in **B**, up to a resolution of about 0.43 nm. For clarity, only selected reflections have been indexed.

6.2. V amylose / α-naphthol crystals

6.2.1. Morphology, unit cell dimensions and symmetry

Figure 37 shows typical $V_{\alpha\text{-naphthol}}$ lamellar crystals. They generally have a more or less square shape, with a lateral size ranging from 0.5 to 2 µm, and appear to be made of several superimposed square unilamellar crystals. Smaller spherical particles are

also observed and are thought to correspond to α-naphthol in excess. Sometimes, such particles are seen embedded in the lamellar crystals, which suggests that they may act as nucleating agents for the crystallization of amylose chains.

The $V_{\alpha\text{-naphthol}}$ crystals had good stability in vacuum, i.e., they did not exhibit any important decomplexation phenomenon. The crystals also demonstrated substantial stability toward the electron beam.

A typical electron diffraction pattern recorded on an untilted $V_{\alpha\text{-naphthol}}$ single crystal (**Figure 38A**) at low temperature is presented in **Figure 38B**. It contains about 560 spots organized along two orthogonal axes with reciprocal base vectors *a** and *b** of equal length. The diagram extends out to a resolution of about 0.13 nm and displays 4 symmetry axes: two along *a** and *b** and two at 45° with respect to *a** and *b**. This diagram has thus the 4*mm* symmetry and since only the reflections indexed with *h0* or *0k=2n* are present along *a** and *b** axes (**Figure 38C**), it belongs to the two-dimensional *p*4*g* square space group. When accounting for these symmetry elements, the diagram consists of 8 equivalent sectors and thus it contains an overall number of 80 independent reflections. The symmetry of the three-dimensional structure was obtained by rotating $V_{\alpha\text{-naphthol}}$ crystals about selected reciprocal axes. It was found that the patterns recorded by tilting the crystals by a given angle around axes *a** and *b** were identical.

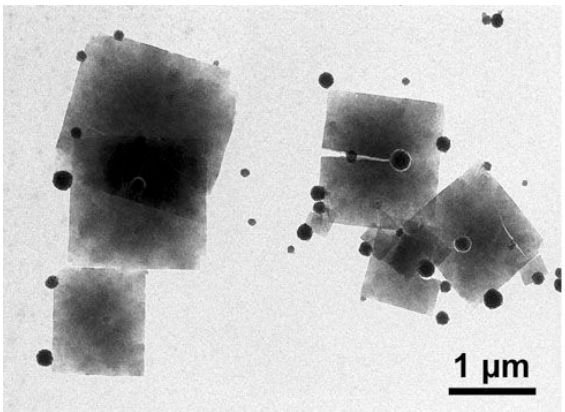

Figure 37. Lamellar single crystals of V amylose complexed with α-naphthol. Dark spherical particles likely correspond to α-naphthol in excess.

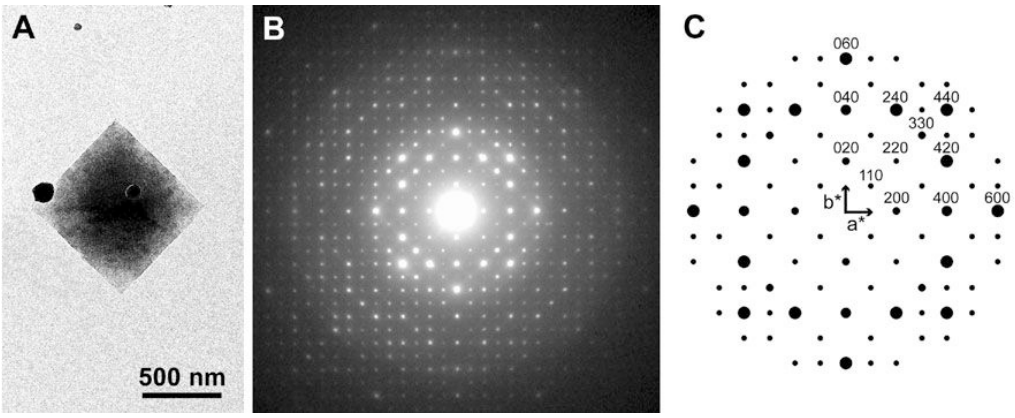

Figure 38. A) Vα-naphthol single crystal ; **B)** corresponding base plane electron diffraction pattern correctly oriented with respect to the crystal in **A** ; **C)** indexation of the pattern in **B**, up to a resolution of about 0.37 nm. For clarity, only selected reflections have been indexed.

Axes *a** and *b** are thus crystallographically equivalent. Moreover, the diffraction diagrams recorded by tilting the crystals clockwise around axes *a** or *b** were identical to those from crystals tilted anticlockwise by the same angle. This equivalence indicates that the *c** axis is perpendicular to the (*a**,*b**) plane and, therefore, that the three-dimensional space group of the Vα-naphthol complex is tetragonal.

A sampling of the patterns corresponding to diffraction zones accessible within the limits of our microscope goniometer is presented in **Figure 39**. **Figure 39A** shows patterns obtained by tilting the crystals by ±26° and ±36° around the *a** axis and corresponding to the $[01\bar{6}]$ and $[01\bar{4}]$ zones, respectively. Diagrams corresponding to $[01\bar{5}]$ (±30°) and $[01\bar{3}]$ (±44°) zones were also recorded but are not presented here. By tilting the crystals by ±40° and ±47° around the axis defined by *a**+*b**, patterns corresponding to the $[1\bar{1}5]$ and $[1\bar{1}4]$ zones, respectively, were recorded (**Figure 39B**). A diagram corresponding to the $[1\bar{1}6]$ zone (±35°) was also recorded but is not shown here. The list of observed electron diffraction spots, together with indexation and corresponding *d*-spacings is presented in **Annex 2**.

The unit cell parameters were calculated using a least-square refinement program from a data set recorded at room temperature. We found the following: *a*=*b*=2.326

(±0.001) nm and *c*=0.788 (±0.001) nm (chain axis), in agreement with previous results (**Yamashita and Monobe, 1971; Helbert, 1994; Winter et al., 1998**).

A density of 1.48 g/cm^3 was measured experimentally on a film consisting of a mat of single crystals. In line with the 8-fold amylose structure helix proposed by Yamashita and Monobe (**1971**), this unit cell could accommodate two amylose helices consisting of 16 glucosyl residues and 8.5 molecules of α-naphthol, assuming that there is no water molecules in the structure.

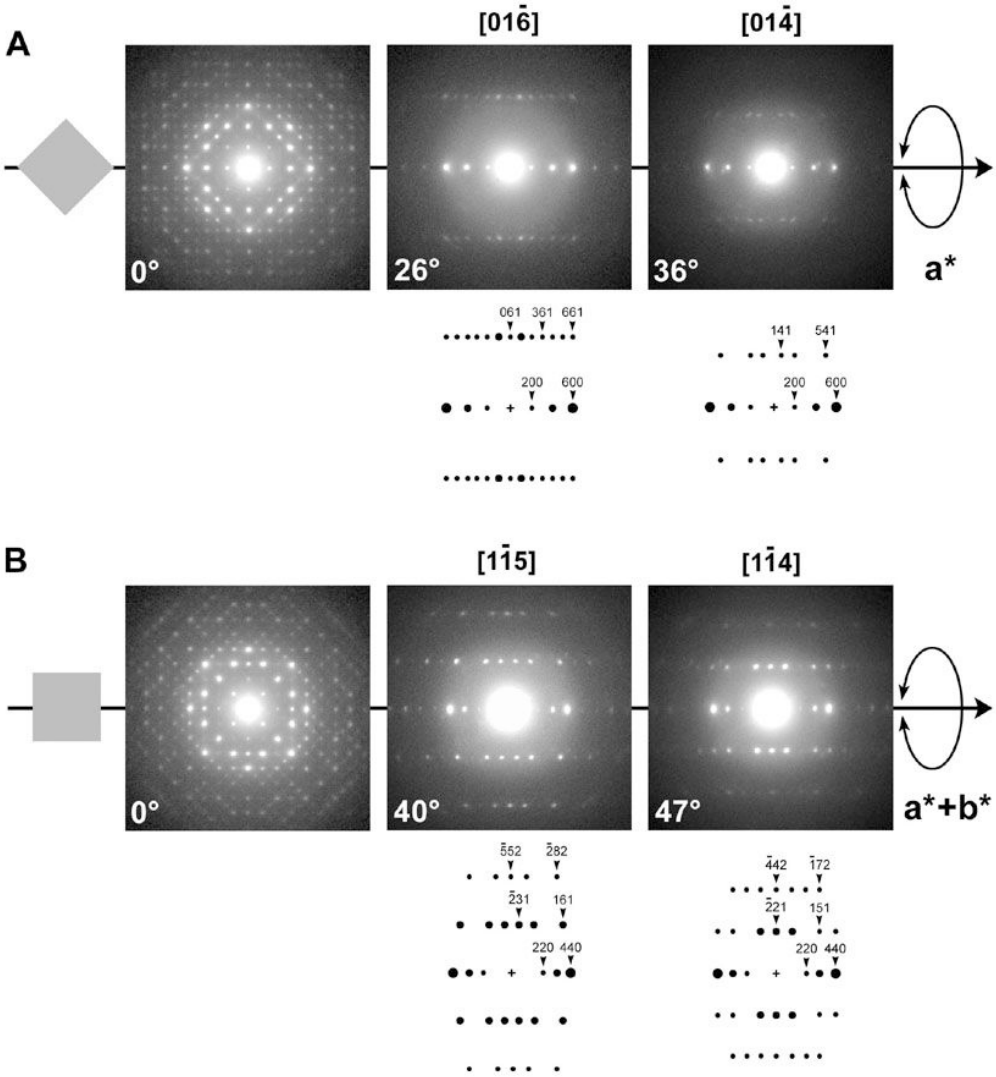

Figure 39. A) Electron diffraction patterns recorded on Vα-naphthol crystals rotated by ±26° and ±36° around *a** ; **B)** diffraction diagrams recorded on crystals rotated by ±40° and ±47° around *a**+*b**. At the left of both figures, the orientation of the square crystal at 0° tilt angle is schematized in gray. The indexation of selected reflections are shown below the tilted patterns.

In this scheme, each amylose helix should be positioned on a 4-fold screw axis, with the implication that the independent repeat unit would not be a glucosyl but a maltosyl residue. Since in the diagram shown in **Figure 38C**, only the reflections with indices *h*00 and 0*k*0 = 2*n* are present along *a** and *b** axes, the likely space group is either $P4_12_12$ (with amylose forming a right-handed helix) or $P4_32_12$ (with a left-handed helix). Both space groups imply that the helices are arranged in an antiparallel fashion.

Figure 40A shows an X-ray diffraction fiber diagram recorded by Y. Nishiyama (CERMAV) at ESRF (Grenoble, France) on a mat of sedimented crystals, with the surface of the mat tilted by an angle of 11° with respect to the incident beam direction. This angle was chosen in order to bring the 004 reflection into Bragg condition.

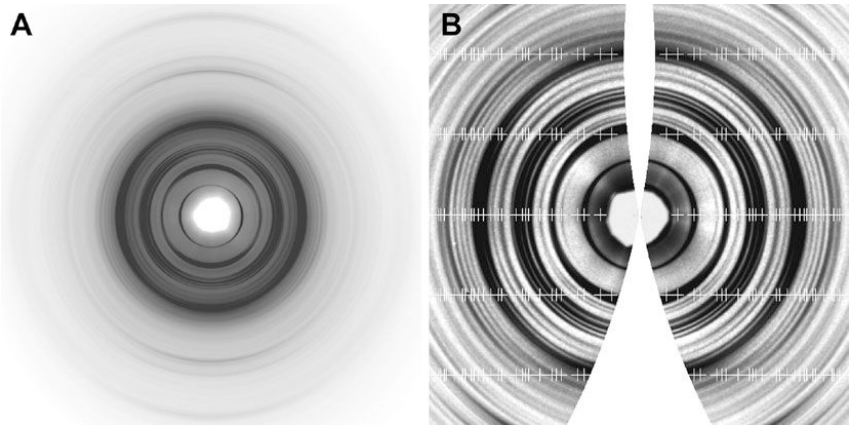

Figure 40. A) Synchrotron X-ray diffraction fiber diagrams recorded on mats of sedimented Vα-naphthol crystals. The mat plane was tilted by 11° with respect to the incident beam. **B)** X-ray diffraction pattern after background subtraction and re-mapping into cylindrical reciprocal space, up to a resolution of about 0.3 nm. The white crosses mark the position of theoretical reflections.

The diagram consists of a number of arcs, each of them having an angular spread (full width at half maximum) of about 35°. This arcing reflects the misalignment of the individual lamellae within the mat, a phenomenon that likely results from uneven deposition of the lamellae during their sedimentation and subsequent drying. The radial broadening of the peaks was very small and corresponded approximately to the size of the incident beam

(**Figure 40B**). No 00*l* reflection was observed up to 0.1 nm resolution. The 004 reflection, which is allowed in both $P4_12_12$ and $P4_32_12$ space groups, was not observed. It is probably very weak or even absent due to the overall 8-fold symmetry of the helix, which brings the intensity of the 004 reflection to a minimum. The 008 reflection, which should be present, is too far out in reciprocal space to be recorded with our equipment. A list of the observed X-ray diffraction spots, together with indexation and corresponding *d*-spacing is presented in **Annex 3**. The unit cell parameters deduced from the X-ray diffraction patterns are *a*=*b*=2.2844 (±0.0005) nm and *c*=0.7806 (±0.001) nm. As generally observed when comparing data from electron and X-ray diffraction diagrams, the parameters deduced from X-ray diffraction are slightly smaller than those resulting from the analysis of electron diffraction patterns. In other crystalline polysaccharides such as cellulose, such parameter increase under electron irradiation has been attributed to a crystalline swelling resulting from beam damage (**Helbert et al., 1998b**).

Patterns such as that shown in **Figure 40A**, which are similar to those recorded by Yamashita and Monobe (**1971**) and Helbert (**1994**), confirm that the amylose helices are perpendicular to the crystal lamellar planes. Quite remarkably, the value of the *c* parameter is equivalent, within experimental error, to fiber repeat values determined by diffraction analysis for the V_H (**Brisson et al., 1991**), $V_{isopropanol}$ (**Buléon et al., 1990**), $V_{butanol}$ (**Helbert and Chanzy, 1994**) and $V_{glycerol}$ (**Hulleman et al., 1996**) complexes.

6.2.2. Molecular lattice image

Figure 41A shows a high resolution lattice image of a $V_{\alpha\text{-naphthol}}$ crystal recorded by J.L. Putaux (CERMAV) at room temperature. Lattice fringes can be seen, although the signal-to-noise ratio is very low and no clear repeating motif can be recognized. The power spectrum (squared Fourier transform of the image) shown in **Figure 41B** confirms that periodic signals are present in the image. The diagram displays 32 clearly visible diffraction spots mirrored in 8 equivalent sectors. It contains 7 independent diffraction spots,

distributed along six layer lines. This optical diffractogram is identical to the electron diffraction pattern (**Figure 41B**) up to the 600 and 060 spots, indicating that the HREM image contains crystal information at a 0.388 nm resolution.

The 1024×1024 pixels^2 images were cut from the original micrograph, with edges parallel to *a* and *b* axes and dimensions corresponding to 32×32 Vα-naphthol unit cells. Only those that produced power spectra with good symmetry and resolution were kept and submitted to a real-space averaging procedure (**Saxton and Baumeister, 1982**).

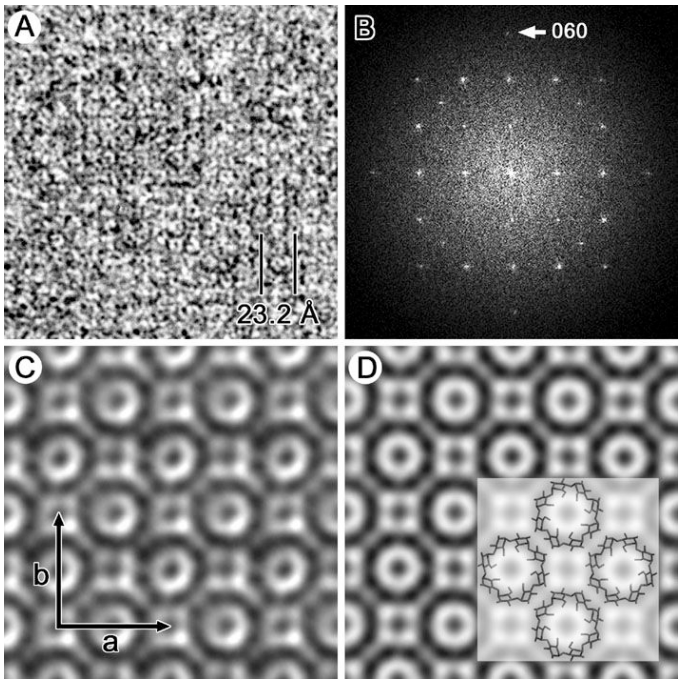

Figure 41. A) HREM image of a Vα-naphthol crystal viewed along the chain axis *c* ; **B)** power spectrum of the lattice image ; **C)** real-space translational average. **D)** 4-fold rotation average of the image in **C.** Inset: a molecular model corresponding to the projection of 8-fold amylose helices viewed end-on is superimposed on the average image.

First, the positions of reflections 600 and 060 were determined form the optical diffractogram. Then, the reciprocal base vectors *a** and *b**, corresponding to absent reflections 100 and 010, respectively, were deduced, as well as real-space lattice vectors *a* and *b*. The experimental image was cut into elementary square boxes with dimensions corresponding to one unit cell, centered on the nodes of a lattice defined by *a* and *b*. Then,

all the boxes were added and an average motif was obtained with a substantially higher signal-to-noise ratio. An average image, built by translating the average motif along *a* and *b* is shown in **Figure 41C**. Considering the 4-fold symmetry of the power spectrum (**Figure 41B**), an additional 4-fold rotational average was calculated from the image in **Figure 41C**. The result is shown in **Figure 41D** and can be described as a square lattice of rings consisting of 8 black oval dots.

The knowledge of the phase contrast transfer function (PCTF) is important in order to verify the correspondence between the average image and the projection of the atomic potential in the crystal (**Erickson and Klug, 1971**). The PCTF is generally determined by recording an image of the amorphous supporting carbon film and by analyzing in the calculated diffractogram the so-called Thon rings whose distribution is directly related to the image defocus (**Thon, 1971**). In our case, as shown in **Figure 41B**, we could not measure the image defocus with precision as we could not detect any clear Thon ring. This absence may be due to the fact that the image was recorded with a very low electron dose, resulting in a very poor contrast. In addition, the image may have been recorded at a defocus where the PCTF has a large bandwidth and therefore, extinction rings would not be seen in the diffractogram. If this assumption is correct, the image has thus been recorded with a defocus close to the so-called Scherzer value, where the contrast is maximum and the atoms are seen as black objects. As a consequence, the rings consisting of 8 black blobs in **Figure 41D** would represent the projection of 8-fold amylose helices along direction *c*, each dot corresponding to a column of glycosyl units. In addition, assuming that the 8-fold amylose helices are in close contact along the diagonal of the unit cell, we can estimate an external helical diameter of 1.62 nm (**Figure 41D**) which is consistent with the models proposed by Yamashita and Monobe (**1971**) and Winter et al. (**1998**).

Black domains also are seen at the center of the helices and in between. Still assuming that the atoms are seen as black objects, these electron-dense regions may correspond to columns of α-naphthol molecules entrapped in the crystal structure, both inside the helical cavity and in the interstitial space between helices.

6.2.3. Molecular model

6.2.3.1. Generation and conformations of helical amylose chains

24 glucose monomers were placed in a cell in such a way that three full helical turns were constructed. The distance between the C1 and C4 atoms in a monomer was constrained to reproduce exactly that found in maltose (**Quigley et al. 1970**) and the helices were optimized.

Each generated helix, which consisted of 80 repeat units (10 helical turns), was placed in a periodic rectangular box. The dimensions of the periodic box were *c*=7.9 nm along the chain axis and *a*=*b*=50 nm. The large values of *a* and *b* were used to ensure that no interaction occurred between the chain and its periodic images. In contrast, the *c* length exactly corresponds to the expected length of a chain having 80 residues. The chains ends were covalently bonded at both ends across the periodic cell to ensure that infinitely long polymers were produced. In addition, the three canonical orientations of the hydroxymethyl groups were considered, namely *gg*, *gt* and *tg* (**Figure 42**). Thus, a total of 6 different helices were produced and optimized.

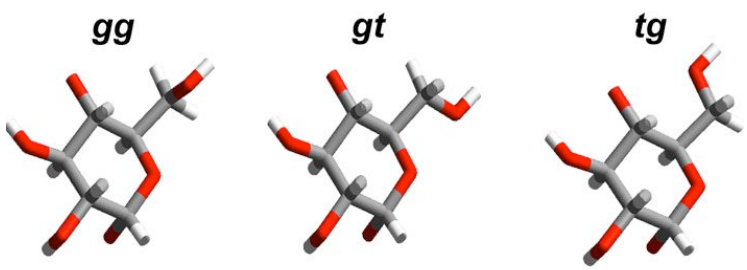

Figure 42. Canonical orientations of the hydroxymethyl groups of glucose.

Conformational parameters at equilibrium are given in **Annex 4**. The Φ and Ψ torsion angles in the minimized structures differ from one structure to the other; Φ ranges

from 90° to 110° and Ψ from -170° to -108°. Those angles are located in the lowest area of the potential energy surface of maltose (**Quigley et al. 1970**). In addition, such a range of values is also observed in the crystal structures of cycloamyloses (**Nimz et al., 2004; Gessler et al., 1999**). All three orientations of the hydroxymethyl group are stable in the final structures and the values are shifted from the canonical ones. The values of the puckering parameters are typical of the $^4C_1$ conformation of a pyranoid ring, ϕ values are small (between 2° and 9°) and the average amplitude is 0.6 Å. According to the literature data, bond angle τ can be in the range 112°-118° (**Rappenecker and Zugenmaier, 1981; Brisson et al., 1991; Gessler et al., 1999; Nimz et al., 2004**). In our models this parameter is remarkably constant between 112° and 113°.

Table 8 presents the optimized energies of the considered isolated helical fragments of the amylose chains having 8 residues per turn, external and internal exposure as well as their hydrogen bonding features. The results reveal that, even in the absence of neighboring molecules, the stereoregularity of the initial structures was conserved during the optimization process. As a consequence, helices have only one independent repeating unit (glucose). The L_1 helical structure behaved differently and it was observed two consecutive independent residues. It is also the lowest energy conformation.

The molecular drawings of the helices are given in **Figure 43**. All helices show a continuous and regular spiral in which a groove can be observed. The exposure of the functional groups at the surface of the helices is presented in **Table 8**. The exterior of the helices is ambivalent, exposing 55% to 67% of the hydrophilic groups. In contrast, the character of the internal surface of the helices strongly depends on the hydroxymethyl group conformation. L_1 and R_1 structures (with the *gg* conformation) have their internal surfaces exposing mostly the aliphatic groups and their internal surface is thus highly hydrophobic. The numerous hydroxyl groups born by the amylose skeleton favor the creation of hydrogen bonds which stabilize the conformation of the chains. **Table 8** lists the hydrogen bonds found in the structures according to geometric criteria (distance and angle).

Table 8. Characteristics of optimized helices in isolation: potential energy in kcal.mol^{-1}.glc^{-1}, exposure (%) of the aliphatic (C-H groups indicated 'phobe') and the hydroxyls and oxygens ('phile') at the external (Ext) and internal surfaces (Int) of the helices and hydrogen bonds (Hbond) description.

	L_1	L_2	L_3	R_1	R_2	R_3
energy	11.7	13.6	13.8	14.1	13.1	18.0
Ext-phile	67	55	59	64	55	69
Ext-phobe	33	45	41	36	45	30
Int-phile	15	52	60	12	51	70
Int-phobe	84	48	40	88	49	30
Hbond*	all residues $O3_n(H)..O2_{n-1}$ every 2 residues $O6_n(H)..O5_{n-1}$ $O2_n(H)..O6_{n+8}$ $O3_n(H)..O6_{n+8}$	$O2_n(H)..O3_n$ $O3_n(H)..O2_{n-1}$		$O2_n(H)..O3_{n+1}$ $O2_n(H)..O6_{n-7}$	$O3_n(H)..O2_{n-1}$	$O3_n(H)..O2_{n-1}$

*when $OX_m(H)..OY_w$ and m = w – intraresidues
when $OX_m(H)..OY_w$ and m ≠ w – interesidues

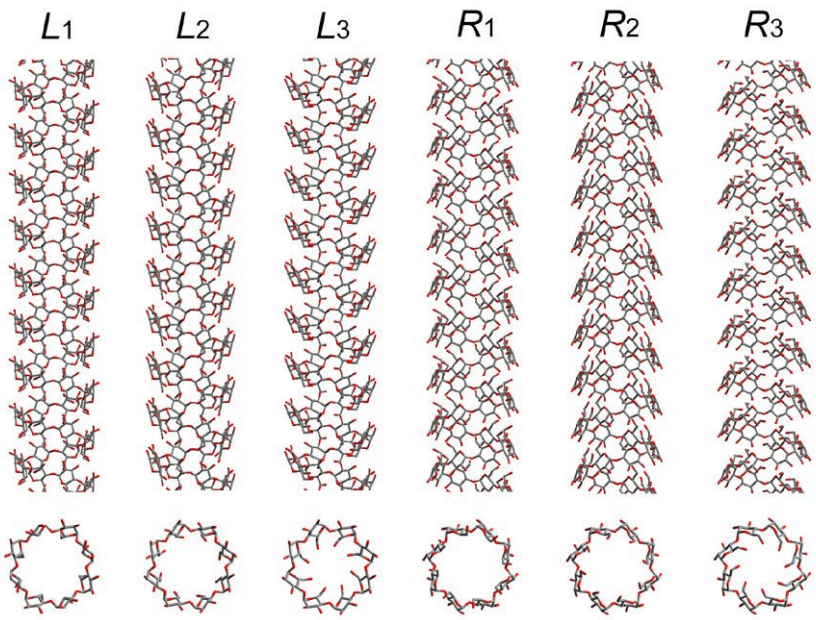

Figure 43. Molecular drawings of the six helices models (top: perpendicular view to the helical axis and bottom: parallel view to the helical axis). For clarity, the hydrogen atoms are not displayed. From left to right are presented the L_1, L_2, L_3, R_1, R_2 and R_3 models.

The distinction between intra-residue and inter-residue hydrogen bonds has been made and the later was also divided into consecutive residues and residues distant by one helical turn. Hydrogen bonds formed between two consecutive residues stabilize the conformation around the glycosidic bridge whereas those formed between residues

separated by a full helical turn, further stabilize the helical conformation of the amylose chain.

The 8-fold helical structures of the amylose chains present very few hydrogen bonds. All helices, with the exception of L_3, possess an hydrogen bond formed between the O3 and O2 hydroxyl groups of consecutive residues and both oxygen atoms act as a donor. The lowest energy conformation L_1 has the larger number of hydrogen bonds. In contrast, the L_3 conformation has no hydrogen bonds and presents the largest energy when compared to the other left-handed helices. Thus, hydrogen bonds have a direct impact on the estimated stability of the isolated helices. **Figure 44** shows the detailed hydrogen bonding network found in the lowest energy helix (L_1). Every two residues, a bifurcated hydrogen bond network is observed. It involves the O6 hydroxyl group with the O5 acetal oxygen between two consecutive residues and with the O2 and O3 hydroxyl groups with a glucose unit separated by a full helical turn.

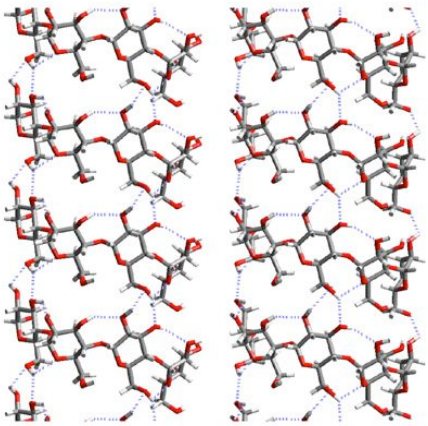

Figure 44. Details of the atomic structure of the optimized isolated L_1 helix onto which are superimposed the hydrogen bonds, displayed as dashed lines. On the right-hand size, a rotation of 5° was performed evidencing the bifurcated hydrogen bonding.

6.2.3.2. Packing of the helices

Dimeric fragments from the right and left-handed helices were introduced in periodic cells having $P4_12_12$ and $P4_32_12$ symmetry, respectively. The dimensions of the periodic cells were defined by the unit cell parameters determined by electron diffraction:

a=b=2.32 nm and c=0.79 nm (chain axis) (**Cardoso et al., 2007b**). The search of stable orientations of the helices in the crystal was performed by systematic rotation of the chains around their helical axis. This procedure was performed at every 1° in the interval 0-180° and, at each step, the energy was calculated. All structures corresponding to local minima of the total energy were then optimized in two steps. In the first step, the skeletal atoms (carbons and acetal oxygens) were constrained and only the hydroxyls and the hydroxymethyls were allowed to move. In the second step, all the atoms were free to move. The cell parameters were always constrained in this two-step procedure. Only the low energy structures that correspond to energy minima have been retained for further analysis. **Figure 45** presents two typical examples of the energy profiles obtained for the L_1 and R_1 helices. The R_1 helix presents five potential energy minima, located at 4°, 43°, 77°, 100° and 131°, while L_1 presents six minima at 30°, 43°, 77°, 100°, 131° and 170°. The orientation of the hydroxymethyl groups presents a small influence on the rotational profile and consequently, the calculated curves were almost unchanged. All minima identified from systematic rotation of the amylose chains were optimized. The structures corresponding only to the lowest energy minimum of each energy profile have been retained for further analysis. **Table 9** gives the energies of the fully relaxed crystal models together with the interaction energies between two neighboring helices.

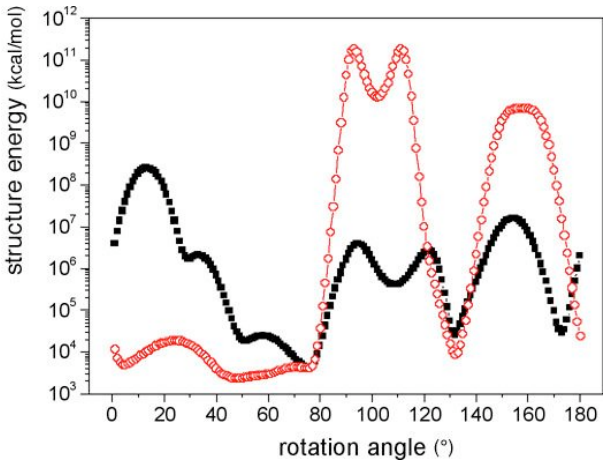

Figure 45. Plot of calculated energy and rotation angle for the L_1 (■) and R_1 (○) helices.

Table 9. Characteristics of optimized helices in the packing: total potential energy (kcal.mol^{-1}.glc^{-1}), interaction energy (kcal.mol^{-1}.glc^{-1}), hydrogen bonds (Hbond) description and surface in contact between the helices (Å^2).

	L_1	L_2	L_3	R_1	R_2	R_3
energy	47.5	76.0	49.5	52.0	53.1	53.6
interaction energy	-4.3	-6.1	-2.6	-3.9	-3.5	-4.5
Hbond* every 2 residues	$O6_n(H)\ldots O3_{sc}$	$O2_n(H)..O4$		$O2_n(H)..O4$ $O6_n(H)..O2_{n+7}$ $O2_n(H)\ldots O6_{sc}$	$O6_n(H)..O3_{n-8}$ $O3_n(H)..O2_n$ $O2_n(H)\ldots O3_{n+1}$	
surface	27	39	25	18	11	14

*when $OX_m(H)..OY_w$ and m = w – intraresidues
when $OX_m(H)..OY_w$ and m ≠ w – interesidues
$O3_{sc}$ and $O6_{sc}$ represent oxygen 3 and 6 of side chain

The most favorable structure is the crystal made of L_1 helices. This is not surprising since it corresponds to the most favorable conformation of the individual chains. However, the total energy depends on the energy of the isolated molecules and on the interaction energy between molecules. The strongest packing corresponds to L_2 helices. This crystal is made of less favorable conformations of the chains. As an effect of hydroxymethyl configuration, the *tg* structures did not present hydrogen bonds. The surfaces that are in contact between two interacting helices in the packing, estimated from the Connolly surfaces, considerably vary from one model to the other, from 11 Å^2 (R_2) to 39 Å^2 (L_2) (**Table 9**). The highest the interaction energy, the largest is the area in contact between two helices.

Figure 46a illustrates the almost perfect packing of two interacting L_1 helices due to the complementary shapes of the helices. The anti-parallel orientation of the helices favored an optimal penetration of the protruding groups of a chain in the groove of the neighboring chain.

Although the conformation parameters of the helices in the optimized packing structures vary from the ones found in the isolated helices, they still adopt typical values. The conformational parameters are presented in **Table 10**. The striking result of the minimization of the crystal structures is that all helices possess two consecutive independent residues, as a result of both the space group symmetries and the presence of neighboring molecules. This feature is well illustrated in **Figure 46b**.

6.2.3.3. Addition of α-naphthol

An initial rough of the number of naphthol molecules that has to be inserted in the crystal structures is estimated from density results. The experimental density was 1.48 g/cm^3 (**Cardoso et al., 2007b**). Considering the total volume of the supercell (4229·10^{-24} cm^3), the total mass of the amylose chains (430·10^{-23} g) and the mass of a naphthol molecule (24·10^{-23} g), it is possible to estimate that the cell must contains between 8 and 9 α-naphthol molecules in order to generate a crystal structure whose theoretical density is in agreement with the experimental one. In addition, the locations of the naphthol molecules in the crystal structures (in the helices, between the helices, or both) have not been experimentally determined.

In order to determine the positions and amounts of the guest molecules using a P_4 space group, it would be necessary use the fractional occupancies. However, this procedure could generate a undesired steric contact since each α-naphthol placed in the crystal cell will generate 8 identical molecules.

Table 10. Conformational parameters of the right and left-handed helices minimized in the packing. Torsion angles Φ and Ψ are the torsion angles across the glycosidic bonds, ω is the torsion angle describing the orientation of the hydroxymethyl group, bond angle τ across the glycosidic bond.

helix	Φ	Ψ	ω	τ
R*1*	92.1° 117.8°	-145.1° -121.6°	-66.2° -56.2°	111.5° 114.4°
R*2*	100.7° 119.5°	-136.0° -118.2°	44.7° 58.4°	112.6° 113.4°
R*3*	102.1° 109.3°	-94.6° -116.1°	115.4° 86.5°	112.6° 112.9°
L*1*	100.1° 105.4°	-145.3° -103.8°	-53.4° -73.5°	112.5° 111.6°
L*2*	90.3° 103.9°	-119.7° -122.7°	131.7° 23.1°	111.4° 110.8°
L*3*	96.1° 94.8°	-126.5° -112.5°	117.1° 132.5°	111.0° 112.9°

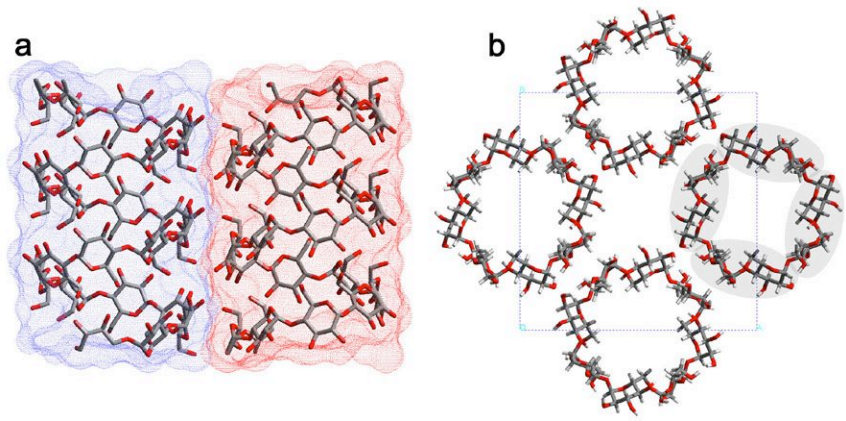

Figure 46. Characteristics of L_1 structure: **a)** complementary shapes of two interacting helices ; **b)** the molecular model evidenced the dimerization of the chains.

In this section, supercells having the P_1 symmetry were generated by considering 4 full helical turns. Those supercells thus have a *c* axis of 3.16 nm. Different amounts of naphthol molecules (from 6 to 12) were then randomly placed in and out of the helices. The stable positions of naphthol in the structure were then searched. The generated structures were first minimized (amylose chains constrained, the naphthol molecules free to move). Then 10 cycles of a simulated annealing protocol was performed. During this procedure, the naphthol molecules and all the hydroxyl groups of the amylose chains were free to change their position. All other atoms from amylose were constrained to keep their original positions. The box cell was not allowed to vary in size and shape. At each cycle, the initial temperature was 300 K and the mid-cycle temperature, 700 K. A 50 K variation in temperature was performed at each 5 ps. After a fully completed cycle, an optimization step was performed and the structure was kept for further analysis. The results were not dependent on the initial orientation of the α-naphthol molecules.

Figure 47 shows a typical example of the dependence of the van der Walls energy on the number of α-naphthol molecules placed in the crystal structure. In the internal region of the helices, the van der Waals energy remains almost constant until the addition of the ninth naphthol molecule (**Figure 47a**). Above which, the energy considerably increases as a consequence of naphthol-naphthol and possibly α-naphthol-amylose unfavorable steric hindrance, due to overlaps of the molecules.

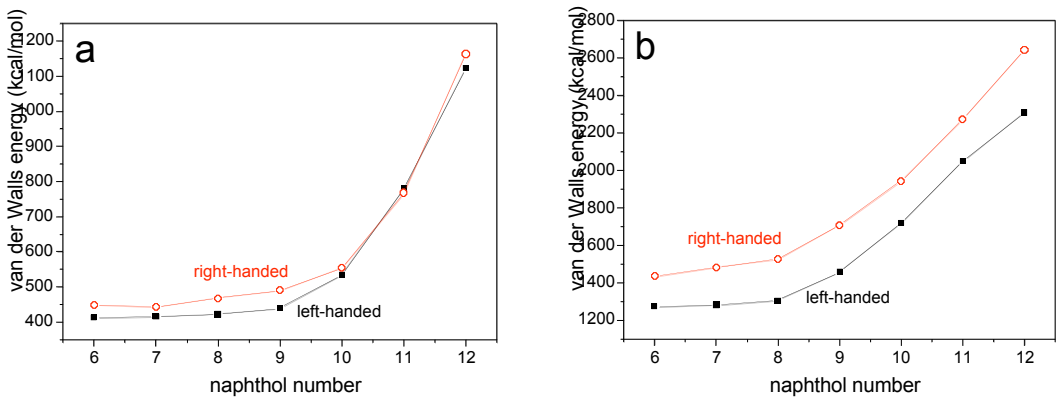

Figure 47. Variation of the van de Walls energy with the number of α-naphthol molecules inserted in (**a**) and in between (**b**) helices.

A similar trend is obtained when α-naphthol molecules are placed in the available space between the helices. The van der Walls energy starts to increase at 9 α-naphthol molecules (**Figure 47b**). Thus, the estimated optimal naphthol content per helical turn i.e. for the original lattice is thus 2.25 inside the helices and 2 between the helices. The exact density of these structures is 1.47894 g.cm^{-3} being in according to the literature data (**Cardoso et al., 2007b**).

α-naphthol molecules were placed in according to simulated annealing results and super-lattices were then generated containing 9 α-naphthol molecules in the helices and 8 between helices. The systems were minimized by allowing the movement of all the atoms within the system. **Table 11** shows the optimized energies of the crystal structures. The L_1 crystal structure is still the most stable and the intermolecular interaction remains the strongest in L_2. Φ and Ψ torsion angles together with τ bond angle are dispersed around the expected values. However, each glucose unit is independent and adjusts its orientation according to local environment. It is a consequence of the P_1 space group used. The striking result is that equilibrium orientations of the hydroxymethyl groups (torsion angle ω) are strongly affected by the presence of α-naphthol molecules. During the optimization process, a substantial amount of hydroxymethyl groups deviate from their original orientation (**Table 11**).

Table 11. Characteristics of minimized amylose/α-naphthol systems: total potential energy and interaction energy in kcal.mol^{-1}.glc^{-1}.α-naphthol^{-1} and number of *gg*, *gt* and *tg* conformations of the hydroxymethyl groups.

	L_1	L_2	L_3	R_1	R_2	R_3
energy	32.8	49.3	37.7	34.3	33.5	39.1
interaction energy	-11.9	-15.8	-12.2	-12.7	-13.6	-11.2
N*gg*	62	5	0	61	56	5
N*gt*	1	29	10	3	4	2
N*tg*	1	30	54	0	4	57

The hydrogen bonds in minimized structures reflect the hydrophilic/ hydrophobic character of the helices. In L_1 and R_1 helices no hydrogen bonds was observed between the amylose chain and the α-naphthol placed inside of the helix. This behavior can be explained from hydrophobic character produced by *gg* conformation.

However, this internal absence does not produce no influence since the α-naphthol placed outside of the helices were hydrogen bonded to the amylose helices in the final structure. All other structures presented hydrogen bonds between external and internal α-naphthol molecules and amylose chain. In addition, the hydrogen bons between neighboring amylose chains were verified in all minimized structures.

Figure 48 shows a L_1 minimized model in a perpendicular and parallel view to the *c* axis. The overall geometry of the helices was nicely maintained and the stereoregularity was kept (**Figure 48a**). Inside the helices (**Figure 48b**), the aromatic rings of the α-naphthol molecules are preferentially oriented perpendicularly to the *c* axis. However, all α-naphthol molecules have presented a small inclination being in according with the free available volume in the internal region of the helix.

The observed average distance between two α-naphthol molecules was 3.55 Å and it is in agreement with that found in the crystal structure of α-naphthol (**Robinson and Hargreaves, 1964**). In contrast, in the external space between the helices, the α-naphthol molecules were organized in pairs. These molecules were alternatively oriented parallel and perpendicular to the chain axis filling the volume available between the helices (**Figure 48c**).

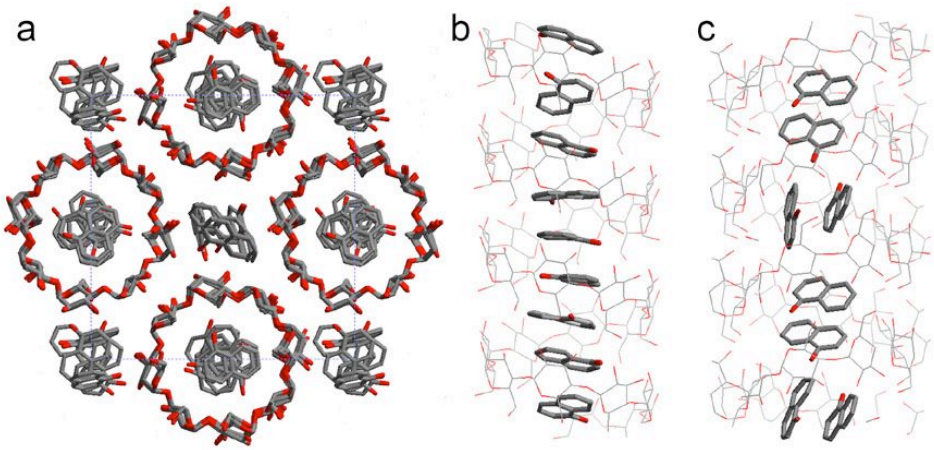

Figure 48. Molecular projections of the L_1 model: **a)** base plane viewed along the helix axes; **b,c)** views perpendicular to the helix axes showing the α-naphthol molecules inside (**b**) and in between (**c**) helices (drawn in light gray).

6.2.3.4. Simulation of diffraction data

The comparison between experimental electron diffraction patterns with those calculated using the molecular models is important to validate the obtained results. Electron diffraction patterns were simulated using Cerius[2]. **Figure 49** compares the simulated diffraction pattern of L_2 with the experimental one. Only the diffracted data corresponding to the base plane (*hk*0) were considered.

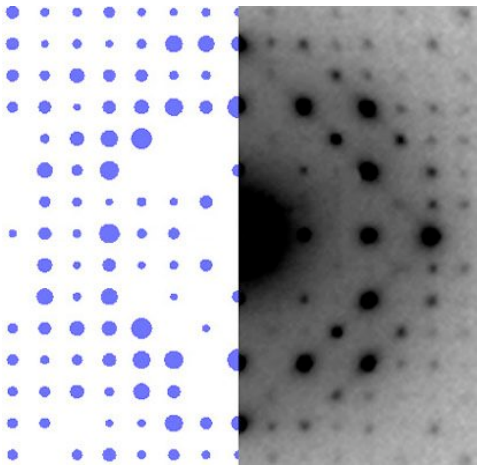

Figure 49. Simulated (left) and experimental (right) electron diffraction patterns of the L_2 crystal structure.

The agreement between predicted and experimental data is qualitatively good. The spots were divided in four groups according to their relative intensities: absent (-), weak (W), medium (M) and strong (S). Among the six tested models, the L_2 one reproduces the best experimental diffraction data. Within a resolution sphere of 3 Å, 15 diffraction spots over 31 are correctly predicted from L_2 model (**Annex 5**).

However, the difference between all tested models is very small, suggesting that this method is not discriminating to estimate the reliability of the models. However, the models were generated with the *P*1 space group and as a consequence, their diffraction patterns were not symmetric. Thus, another important considered parameter was the ability of the models to produce symmetric diffraction patterns. Intensities corresponding to the spots indexed *hk* and *kh* were compared. The total number of spots whose theoretical intensities correctly matched the experimental ones gives a rough estimate of the capability of a given model to reproduce the *p*4*g* experimental symmetry diffraction. The predicted diffraction patterns were tested according to the symmetry in the intensities of the *hk* and *kh* spots. The symmetry factor is defined as:

$$sym = \sum_{hk} \left(I_{hk} - \langle I_{hk} \rangle \right)^2 \tag{11}$$

where $<I_{hk}>$ is the average value given by the expression:

$$\langle I_{hk} \rangle = \frac{1}{n} \left(I_{hk} + I_{h\bar{k}} + I_{\bar{h}k} + I_{\bar{h}\bar{k}} + I_{kh} + I_{\bar{k}h} + I_{k\bar{h}} + I_{\bar{k}\bar{h}} \right) \tag{12}$$

The global symmetry factor (*gsf)* for each simulated diffraction pattern was obtained from the addition of the symmetry factor for each I_{hk} group. **Table 12** presents the symmetry factor for each I_{hk} group as well as the *gsf* values for the simulated diffraction patterns. Here again, model L_2 gives the lowest *gsf* which indicated that its corresponding diffraction pattern is the most symmetric one. It is important to observe that the model L_3 also corresponds to a low value of the *gsf*. The most noticeable feature of the two structures which reproduce the best the experimental data is that their hydroxymethyl groups have two dominant conformations *gt* and *tg*. The best model L_2 has almost the same amount of both

orientations. To summarize, the alternation between *gt* and *tg* hydroxymethyl configurations seems to have a good relationship with the symmetric diffraction reproduction.

Table 12. Symmetry factor for each I_{hk} group as well as the gsf values for the simulated diffraction patterns.

	L_1	L_2	L_3	R_1	R_2	R_3
$sym\ I_{10}$	3	0	1	0	1	4
$sym\ I_{11}$	18	30	36	10	41	28
$sym\ I_{20}$	18	25	7	27	74	14
$sym\ I_{21}$	8	8	8	8	8	8
$sym\ I_{22}$	33	3	2	55	83	4
$sym\ I_{30}$	10	5	2	4	14	5
$sym\ I_{31}$	25	10	108	18	25	5
$sym\ I_{32}$	16	2	29	34	58	11
$sym\ I_{33}$	410	219	93	389	770	416
$sym\ I_{40}$	697	233	311	778	1552	386
$sym\ I_{41}$	61	39	100	29	67	29
$sym\ I_{42}$	646	262	233	1127	2151	228
$sym\ I_{43}$	263	169	164	47	236	54
$sym\ I_{44}$	123	39	62	109	123	9
$sym\ I_{50}$	24	3	33	12	20	3
$sym\ I_{51}$	72	13	20	43	98	25
$sym\ I_{52}$	108	35	18	29	86	30
$sym\ I_{53}$	649	114	156	670	1186	316
$sym\ I_{54}$	56	29	34	18	35	192
$sym\ I_{55}$	140	53	116	384	545	2
$sym\ I_{60}$	65	42	45	80	294	119
$sym\ I_{61}$	185	94	88	81	101	90
$sym\ I_{62}$	783	195	135	1276	3549	400
$sym\ I_{63}$	23	30	28	11	60	96
$sym\ I_{64}$	33	24	26	50	73	43
$sym\ I_{65}$	20.	20	18	123	54	89
$sym\ I_{70}$	6	5	4	6	24	5
$sym\ I_{71}$	21	8	114	156	675	59
$sym\ I_{72}$	14	14	22	207	138	123
$sym\ I_{73}$	41	13	37	48	31	73
$sym\ I_{80}$	12	25	30	15	27	33
gsf	4596	1775	2092	5856	12214	2912

6.2.3.5. NPT molecular dynamics

The volume of the models obtained so far was constrained by keeping the experimental cell dimensions. The structures obtained by NVT molecular dynamics and minimization, while energetically stable as they correspond to minima of the potential energy surfaces, are not necessary in a mechanical equilibrium. As a matter of fact, the values of the components of the internal stress tensor, defined as the first derivatives of the potential energy per unit volume with respect to strains, are low but not minimal. **Annex 6** presents the optimized cell parameters, stress tensors and final energies of molecular models.

Molecular dynamics simulations in the NPT ensemble at 1 atm and 300 K, is needed in order to ensure a mechanical equilibrium state. Initial and optimized values of the stress tensors are given in **Annex 6**. As it was expected, all optimized stress tensors values have converged to zero. All the structures expand during NPT molecular dynamics which corresponds to a lowering of the density of 15% on average. Similar behavior has already been observed in the atomistic simulation of the native crystal structures of cellulose using different force fields; this seems to be a general trend (drawback) in the modeling methods. L_2 has the highest predicted equilibrium density of 1.3166 g.cm^{-3}; it is consequently the structure that reproduces the best the experiments. The expansion is anisotropic, a and b parameters of the cell differ and maximum variations are observed for the cell parameter *c*, which ranges from -0.8 Å (contraction) to +2.4 Å (expansion).

6.2.3.6. Refinement of crystal structure

The structures studied in section **6.2.3.4** were converted in their respective space group $P4_12_12$ or $P4_32_12$ for right and left-handed helices, respectively. Moreover, for each starting model, 8 models were produced presenting variations in the α-naphthol position and occupancy, totalizing 48 different models. Models were input to refinement in SHELX-97 (**Sheldrick and Schneider, 1997**), and completed over several rounds of iterative model building and refinement in SHELX. The SHELX calculations consist of conjugate

gradient least-squares minimization. The refinement procedure was conducted against data from non-saturating electron diffraction diagrams, after normalization of the intensity.

Using the average intensity of electron diffraction spots up to a resolution of 1.3 Å (**Annex 7**), no model converged on experimental diffraction intensities. The calculated R-factors were higher than 100% showing an unsatisfactory fit between the models and the experimental data. However, when the resolution was limited to 2.8 Å, the relative R-factor decreased, ranging from 52 to 87% for 47 models. A R-factor of 13% was obtained from a model built from left-handed 8-fold helices and containing hydroxymethyl groups with alternating *gt* and *tg* conformations. Occupancies of 0.50 and 0.56 were assigned to α-naphthol molecules located between and inside the helices, respectively.

The excessive difference between 1.3 and 2.8 Å in structure resolution does not seem to be related to final form of the structure. As the electron diffraction contains about 560 spots and the diagram extends up to a resolution of about 1.3 Å, probably this corresponds a deviation originated from double diffraction. This effect is the phenomenon whereby a diffracted beam traveling through a crystal is rediffracted either within the same crystal or when it passes into a second crystal. Reflections attributable to double diffraction are a common feature of electron diffraction patterns recorded from two-phase materials exhibiting an ordered crystalline growth on a monocrystalline substrate (**Tietz et al., 1995**). Thus, even using normalized and under-exposed diffractions, probably complicated patterns may be formed, making difficult to distinguish the “real” from the double-diffraction reflections when resolutions smaller than 2.8 Å are required. Due to their weak intensity, the spots corresponding to 1.3 and 2.8 Å spacings cannot be used since the treatment to distinguish the “real” contribution of the diffraction and its double diffraction artefact was not efficient. In order to avoid this effect, the adequate procedure should be use the X-ray diffraction results since from this technique the double diffraction effect is not observed.

Figure 50 shows the molecular projections of the V-amylose/α-naphthol complex model in the base plane viewed along the helix axes and views perpendicular to the helix axes showing the α-naphthol molecules inside and in-between helices.

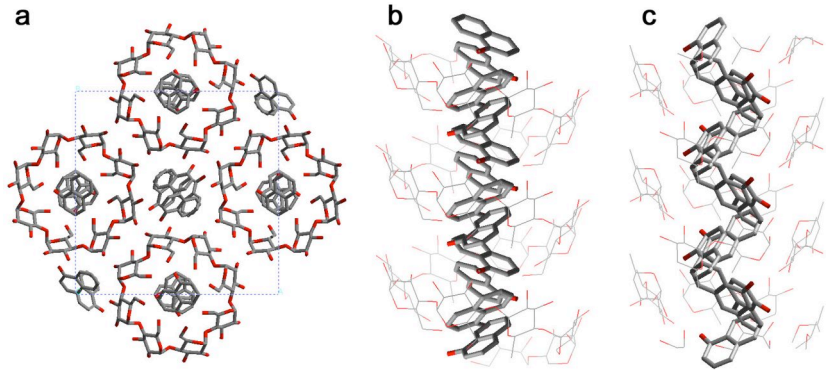

Figure 50. Molecular projections of the V-amylose/α-naphthol inclusion complex refined using the SHELX program: **a**) base plane viewed along the helix axes; **b**,**c)** views perpendicular to the helix axes showing the α-naphthol molecules inside (**b**) and in between (**c**) helices (drawn in light gray).

As an imposition of $P4_32_12$ space group (left-handed helix), the helices were arranged in an antiparallel fashion. Each amylose helix was positioned on a 4-fold screw axis, implicating that the independent repeat unit is a maltosyl residue. Amylose helices presented an external diameter of 1.62 nm and hydroxymethyl conformation alternated between *gt* and *tg*. As it was foreseen, the α-naphthol molecules were located, inside and in between helices, exactly in free available volume of the helices. **Figure 51** shows the α-naphthol placed in free available volume of the helix internal region.

The present structure represents a satisfactory model of untilted experimental diffractions. Nevertheless, during the refinement, the information obtained from X-ray or tilted electron diffraction was not used due to difficulty in the measurement of intensities. Thus, the exact position of α-naphthol molecules along to *c* axis could not be determined.

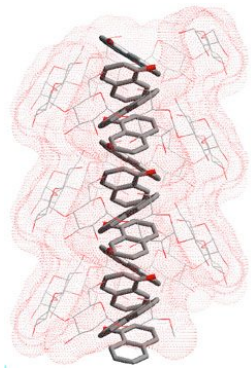

Figure 51. Longitudinal view showing the α-naphthol molecules located inside the helix.

Figure 52 shows experimental and simulated diffraction electron patterns obtained from refined model by SHELX program. Only the diffracted data corresponding to the base plane (*hk*0) were considered. A good correspondence between simulated and experimental electron diffraction patterns can be observed up to a resolution of 2.8 Å. However, some reflections present in theoretical or simulated diffraction are not present in the other one. Apparently, reflections 340 and 430 are absent from the experimental pattern whereas reflections 150 and 510, present in the experimental diffraction are absent in the simulated one. Even so, the general profile of the simulated and experimental reflections are comparable between them producing a satisfactory R-factor of 13%.

Figure 53 shows the refined model superimposed in the 4-fold rotational averaged image obtained by high resolution electron microscopy. Assuming that the atoms are black, the rings consist of 8 black oval dots corresponding to the projection of 8-fold amylose helices along direction *c*. Each dot is superimposed by a glycosyl unit. Black regions are also seen at the center of the helices and in between them. These regions correspond to columns of α-naphthol molecules, both inside the helical cavity and in the interstitial space between helices.

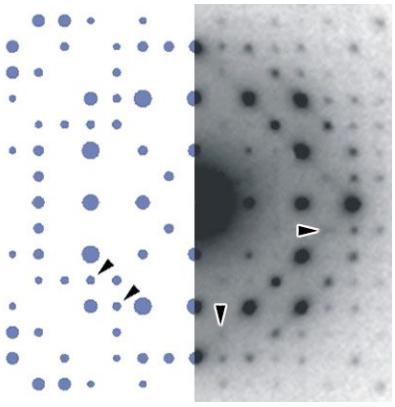

Figure 52. Experimental (right) and simulated (left) diffraction electron pattern obtained from refined model by SHELX program. The arrows indicate spots observed in a diffraction pattern but absent in the other one.

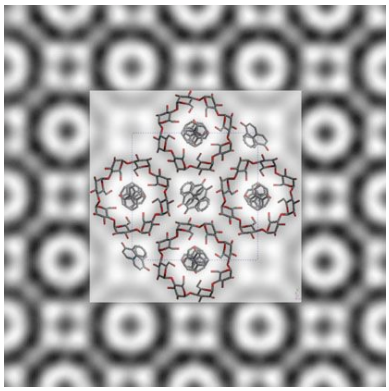

Figure 53. Refined model superimposed in the real-space averaged lattice image of the crystal.

6.3. Discussion

A polymer chain in very dilute solution can actually be regarded as isolated and its shape is governed by short an long range inter- and intra-molecular interactions. In the aggregated state, this is no longer true. The behavior of the chain is largely influenced by the proximity of the neighbouring chains and the attraction forces which act between them. In the concentrated state, these factors determine the orientation of chains relatively to each other. The equilibrium configuration essentially depends on the interplay between the entropy and internal energy of the system.

In dilute solution, polymers normally attain a state of maximum entropy consistent which a stable state of minimum free energy. Crystallization is a process involving the orderly arrangement of chains and is consequently associated with a large negative entropy of activation. If a change of favourable free energy is to be obtained for crystallite formation, the entropy term has to be offset by a large negative energy contribution. The alignment of polymer chains at specific distances from one another to form crystalline nuclei will be assisted when intermolecular forces are strong.

Among the V amylose crystals that have been prepared and investigated during this work, the $V_{\alpha\text{-naphthol}}$ single crystals stand out as being by far the most perfect in terms of crystalline organization if compared to the $V_{\text{isopropanol}}$ ones. The protocol of crystallization as well as the nature of the guest molecule seem to plays an important role in the structuration of the complex. The crystals obtained by complexation with linalool were

elongated lamellae, stable during room temperature observation in the electron microscope. They were longer than $V_{isopropanol}$ crystals. Individual lamellae were not observed for the $V_{linalool}$ crystals. We thus assume that the solubility of the guest molecule plays an important role during the crystallization. As the crystallization corresponds to the formation of a three-dimensional ordered phase from a disordered state, the solubility of the guest molecule probably influences the size, shape and crystallinity during the crystallization.

The first step in crystallite formation is the creation of a stable nucleus brought about by the ordering of chains in a parallel array. The chains are initially attracted between them by intermolecular forces followed by the stabilization of long range order into a three-dimensional ordered structure. The second stage is the growth of the crystalline region, the size of which is governed by the rate of addition of other chains to the nucleus. In this way, in the $V_{isopropanol}$ case, the soluble complexing agent seems to favour the first step of crystallization since the $V_{isopropanol}$ crystals had a size smaller than that of lamellae contained in flower-like aggregates than $V_{linalool}$. On another hand, for the crystallization performed with linalool, the second step of the crystal formation seems to be favoured. This fact can be evidenced since a small number of large aggregates can be observed by TEM. Thus, the solubility of the complexing agent probably influences the various steps of crystallization causing the differences between $V_{isopropanol}$ and $V_{linalool}$ crystals.

The crystallization mode of $V_{isopropanol}$ family does not seem to depend on the amylose size and type as well as the temperature heating during the polymer solubilization. On another hand, the quality of $V_{\alpha\text{-naphthol}}$ crystals seems to be favoured by long crystallization times and by the use of synthetic amylose of DP 100. Due to a high crystallinity, $V_{\alpha\text{-naphthol}}$ crystals yield highly resolved electron diffraction diagrams, extending to a resolution of around 0.1 nm. It is quite unusual for other types of V amylose crystals as well as other polysaccharides or even synthetic polymers. To our knowledge, such a resolution for polysaccharide crystals was only obtained with a few native fibrous crystals such as those of algal (**Sugiyama et al., 1985**) or animal (**Helbert et al., 1998a**) cellulose or chitin specimens such as in *Sagitta*'s grasping spines (**Saito et al., 1995**).

Concomitant with this perfection, the $V_{\alpha\text{-naphthol}}$ crystals are also quite stable when irradiated with an electron beam. This stability is reflected in the recording of high-resolution images such as that shown in **Figure 41A**, although it was recorded at room temperature. The lattice is readily revealed, thus indicating that the periodical information of the projected crystalline structure has been preserved to a resolution of a few angstroms.

Lattice images of polysaccharide crystals have generally been recorded perpendicular to the fiber axis of microfibrillar cellulose (**Sugiyama et al., 1985; Imai et al., 2003**) or chitin (**Revol et al., 1988; Saito et al., 1995**) and, more rarely, parallel to the fiber axis (**Helbert et al., 1998**). To our knowledge, only one paper reports lattice imaging of lamellar V amylose crystals (**Miller, Sugiyama, Brisson, Chanzy, 1990**). However, the images do not allow the unambiguous recognition of 6-fold helices. Our HREM images thus appear to be the first that clearly show the organization of V-amylose helices in the *(a,b)* base plane of the crystal.

Up to now, the structure determination of the various types of V amylose has led to some controversy. When surveying the unit cell parameters determined by various authors, one notices that the base plane dimensions vary depending on the crystal type. However, all types share a common repeat along the fiber axis, i.e., about 0.8 nm. Despite this common value, the authors have debated to know whether the amylose helices were 6-, 7-, or 8-fold depending on the complexing agent. The propositions to account for such a diversity are based on the similarity between helical amylose and α-, β-, and γ-cyclodextrins, composed of 6, 7, and 8 α-D-glucosyl units, respectively. These cyclic molecules have external diameters of 1.36, 1.47 and 1.64 nm, respectively (**Takeo and Kuge, 1969; Takeo and Kuge, 1970**). Since the V_H structure is described as a close-packed arrangement of 6-fold helices that also have an external diameter of 1.36 nm (**Zaslow et al., 1974; Rappenecker and Zugenmaier, 1981; Brisson et al., 1991; Mikus et al., 1946**), the diameters of V_H amylose helices and α-cyclodextrins perfectly match.

The situation of $V_{n\text{-butanol}}$ crystals is more complex, and it is believed that the amylose helices were separated by intercalated *n*-butanol molecules to account for the larger unit cell parameters of the base plane (**Booy et al., 1979; Helbert and Chanzy, 1994**). Since the removal of the *n*-butanol molecules invariably leads to the V_H structure without modification of the crystal shape (**Manley, 1964; Yamashita, 1965; Booy et al., 1979; Helbert and Chanzy, 1994**), it seems logical that $V_{n\text{-butanol}}$ crystals also contain 6-fold amylose helices with an external diameter of 1.36 nm.

The case of $V_{isopropanol}$ crystals is not clear at the moment. On the one hand, one can conceive that they are made of 7-fold helices. Such larger helices have first been considered to account for the large unit cell of crystals of V amylose complexed with tert-butyl alcohol (**Takeo and Kuge, 1969; Bear, 1944; Zaslow, 1963**), which have the same unit cell as $V_{isopropanol}$. This unit cell can accommodate a number of 7-fold helices in close contact, with helices having an external diameter of 1.47 nm, i.e., that of β-cyclodextrins. On the other hand and in opposition to this argument, the fact that Visopropanol single crystals can readily be converted into the 6-fold V_H structure without loosing their perfection (**Yamashita and Hirai, 1966; Buléon et al., 1990**) and that they can be colored with iodine (**Helbert, 1994**) is not in favour of the presence of 7-fold helices in these crystals. Thus, the $V_{isopropanol}$ structure could resemble that of $V_{n\text{-butanol}}$ and therefore could consist of 6-fold helices separated by isopropanol intercalates. In favor of this last assumption, the $V_{n\text{-butanol}}$ crystals can be converted into the $V_{isopropanol}$ crystalline type if they are soaked into cyclohexanone, and again they can do so without loosing their apparent perfection (**Helbert and Chanzy, 1994**). Taken together, these observations leave open the existence of 7-fold amylose helices in V amylose crystals.

The 8-fold amylose helices that are described in the present paper have an external diameter of 1.62 nm, which is very close to that of γ-cyclodextrins. The 8-fold helices markedly differ from those occurring in V_H, $V_{n\text{-butanol}}$ and $V_{isopropanol}$ crystals. Their helical structure appears to be quite stable as it was not possible to convert them into V_H by

removing the complexing agent. In the same manner, iodine, which could permeate the 6-fold helices in the crystals of V_H, $V_{n\text{-butanol}}$ or $V_{\text{isopropanol}}$, could not do so in the case of $V_{\alpha\text{-naphthol}}$ (**Helbert, 1994**). Thus, while the occurrence of the 7-fold helices in $V_{\text{isopropanol}}$ complexes is doubtful, we confirmed the 8-fold structure in the case of $V_{\alpha\text{-naphthol}}$ crystals. It is likely that if the electron crystallography treatment that was applied to the $V_{\alpha\text{-naphthol}}$ crystals could also be used for $V_{\text{isopropanol}}$ and the $V_{n\text{-butanol}}$ crystals, all ambiguities about the 7-fold helices would be removed.

One may wonder why the $V_{\alpha\text{-naphthol}}$ crystals presented in this study have a crystallinity substantially better than those of the other V amylose complexes despite crystallization procedures that are very similar. One of the reasons may be found in our use of synthetic amylose. Indeed, this amylose, which is perfectly linear, differs from the commercial fractions that were used earlier (**Helbert, 1994**). The amylose fractions extracted from starch are known to contain a certain degree of branching, a feature that is detrimental for the preparation of defect-free crystals. In addition to its linearity, the amylose we used has an average DP of 100. Assuming a rise per glucosyl monomer of about 0.1 nm, 8-fold helices formed with DP 100 amylose would have a length of roughly 10 nm. Consequently, there is no need for the amylose chains to fold back and forth to produce crystalline lamellae with a thickness of about 10 nm. Indeed, the chain-folding mechanism is easily observed with flexible synthetic polymers but is more difficult with semirigid polymers such as underivatized polysaccharides, for which the best crystals have systematically been obtained when the chains were short enough to avoid chain-folding (**Buléon et al., 1982**). Thus, even if in amylose, the possibility of chain flipping (**Jacob et al., 1998**) could favor a tight folding of the chains, we think that chains of DP 100 have an optimal length to form folding-free and therefore defect-less crystals.

In line with an experimental density of 1.48 g/cm^3 (**Cardoso et al., 2007b**), the unit cell of 8-fold amylose helices accommodates two amylose helices consisting of 16 glucosyl residues and 8.5 molecules of α-naphthol, assuming the absence of water molecules in the structure. As imperfections and amorphous regions can exist in the crystals,

the density measured experimentally is expected to be lower than the theoretical value estimated from a perfect crystal. Thus, the theoretical density of the molecular structure, 1.498 g/cm^3, is in agreement with experimental density result.

The final alternating hydroxymethyl configuration in the Vα-naphthol model in an interesting characteristic (**Figure 50**). In addition to refinement against electron diffraction data, this alternating configuration was also verified from energy minimization of the structure in P_1 symmetry. In the energy optimization process, a significant amount of hydroxymethyl groups changed their initial orientation. This changing was observed between *gt* and *tg* configurations. Thus, the alternating between *gt* and *tg* hydroxymethyl conformations results in an increase of stability in the crystal model.

To summarize, the model for Vα-naphthol proposed in **Figure 50** is in agreement with the number of glucosyl residues and molecules of α-naphthol expected by the combination of space group and experimental density results as well as by theoretical minimization procedures. Two α-naphthol molecules were found to lie in each helical turn in between helices while 2.25 molecules were located inside the helix. The model containing 8-fold left-handed single helices arranged in an antiparallel packing exhibited the lowest R-factor and, moreover, the proposed structure was superimposed onto HREM lattice image.

CHAPTER 7

CONCLUSION AND PERSPECTIVES

A study of the alkaline extraction of the Brazilian rice starch at a laboratory scale was presented. Regarding the protein detection, the biuret test showed limited sensitivity when compared to UV-vis and fluorescence spectroscopy, which were able to detect smaller amounts of residual proteins in the supernatant. Pyrene and isothiocyanate benzazole derivative, highly fluorescent when irradiated with UV-light, were successfully used as a molecular fluorescent probe to detect proteins during starch isolation. The isothiocyanate dye allows detecting proteins in solution even in the last extraction step of the alkaline extraction of rice starch. The intrinsic fluorescence results indicated that the proteins were not efficiently removed with NaOH concentrations lower than 0.15% w/v. SEM images as well as fluorescence, WAXS and DSC data concurred to show that the alkaline extraction was optimal using NaOH concentrations between 0.15 and 0.18% w/v. Using NaOH concentrations higher than 0.24% w/v results in a significant disruption of the granular morphology associated to a decrease of crystallinity and gelatinization enthalpy. This effect was attributed to the alkaline swelling of starch granules. In addition, SAXS analysis indicated a gradual disruption of crystalline lamellae of the granules during the starch-protein separation. This effect was attributed to the dissociation of hydrogen bonds inside the starch granule. Moreover, SEM showed that the general granular morphology of supercritically dried starch was preserved.

Thymol complexation followed by gel filtration chromatography was performed on rice starch in order to separate amylose from amylopectin. The hydrodynamic behavior of amylose in the fractions collected after gel filtration chromatography presented the polymer as a spherical particle. The deviation from the random coil structure is probably related to contamination with residual amylopectin or to the inefficient measurement of the radius of gyration by the dissymmetry method. Commercial amylose was used in order to study the polymer behavior in aqueous media with different ionic strength as well as storage time. Amylose random coils presented an increase of radius of gyration when the alkali concentrations were increased in opposite to the behavior when salt solutions were

analyzed. Moreover, the storage time appeared to be an important factor in the analysis of the amylose solutions. During storage, amylose presented a trend of radius reduction. This effect was not related to the depolymerization of the carbohydrate. In 1.2 M KCl solutions the effect of storage time was not observed. In this situation, amylose and solvent seem to be in an ideal condition for the polymer stabilization since during storage, the radius did not change.

Lamellar V amylose crystals were prepared by adding guest molecules to dilute metastable amylose solutions. Inclusion compounds of V amylose crystalline types were obtained, in particular, with isopropanol, linalool and α-naphthol. The characterization of $V_{isopropanol}$ and $V_{linalool}$ crystals was performed using electron diffraction analysis. These crystals were organized in flower-like aggregates, suggesting that several rectangular crystals initially outgrew from a unique nucleus. The corresponding electron diffraction diagram suggested an orthorhombic structure with cell parameters in agreement with literature. $V_{\alpha\text{-naphthol}}$ lamellar crystals presented a square shape with a lateral size ranging from 0.5 to 2 μm. Electron diffraction patterns recorded on untilted and tilted crystals suggested a tetragonal unit cell. The structural details of the crystalline structure of the $V_{\alpha\text{-naphthol}}$ complex were investigated by molecular modeling and refinement against diffraction data. The model exhibiting the lowest reliability factor was described by a lattice of antiparallel 8-fold left-handed single helices with alternating *gt* and *tg* hydroxymethyl conformations. Molecules of α-naphthol are included in the crystal lattice, both inside and in-between helices. The projection of the model along the helical axis was successfully superimposed onto high resolution lattice images of the crystals recorded at room temperature, providing the first evidence of an 8-fold single helical form of amylose.

The results of this work indicate that the extraction of the starch still presents some aspects to be explored, leading to an improvement of the methods nowadays used, as well as the proposal of new methodologies to be implemented in the control of the process on a large scale. Moreover, rice appears as a promising source to produce starch in the Brazilian industry. The use of broken rice flour, associated with the easy extraction becomes

attractive in a technological point of view. On the other hand, rice starch can be used to produce amylose and new methodologies should be tested in order to improve the efficiency in the amylose/amylopectin separation. It could be verified that the study of dilute starch solutions could lead to a better knowledge of the chains structuration in different dissolution conditions. The study of the physico-chemical properties of amylose in aqueous solutions is useful to understand the tendency of self-organization of the polymer. The helical structure obtained during the amylose crystallization presents a great potential for pharmacology and in the food industry since the trapped guest molecules can be released later. Finally, amylose structuration in the crystalline form presents a real possibility of an anisotropic chains organization having important molecular order. This area will have wide to be explored in the next years, mainly when related to the kinetic formation of these structures.

The alkaline extraction of starch was studied at a laboratory scale and adaptations can be made in order to extrapolate this method to an industrial scale. The obtained rice starch was duly characterized during this work. However, its application as an additive in the processed foods was not tested. The protocol of rice starch extraction can be tested using different alkaline solutions as well as a combination of different solvents in order to remove the residual prolamin amounts. The main procedure of alkaline extraction can be used to extract other starch sources if duly adapted. The spectroscopic characterization was performed. Therefore, the rheological properties of alkaline extracted starch need to be studied. The alkaline gelatinization was verified during the extraction procedures and this mechanism remains unknown.

In this work, the influence of storage time in NaOH and KCl solutions was studied. Therefore, it is necessary to understand what is the property that allows to increase or decrease the amylose radius during the storage. Beyond NaOH and KCl solutions, other alkaline and saline solutions should be tested in order to compare with our results. Another important topic to be studied is the mechanism of amylose dissolution since the polymer properties seem to be related to dissolution procedure. Moreover, as in 1.2M KCl solution

amylose remains with an invariable radius during the storage time, it is necessary to investigate the related property to this phenomenon. Other saline solutions should be tested in order to produce the same amylose effect than in 1.2M KCl solution. From the knowledge of the amylose properties in aqueous solutions, it can be tried to perform an amylose organization as a colloidal particle using different solvents and surfactants.

An important topic to be studied is the improvement of the crystallization method of $V_{isopropanol}$ crystals in order to obtain single isolated lamellae. Moreover, the modeling protocol used to determine the molecular structure of $V_{\alpha\text{-naphthol}}$ crystals can be used to determine that of other V-amylose complexes. During this work, we have shown that $V_{\alpha\text{-naphthol}}$ crystals exhibited a high quality. Therefore, it is necessary to understand what is the synthetic amylose effect in the quality of the crystals. The α-naphthol molecule induce the 8-fold helix formation but the molecular property responsible for this complexation is still unknown. We did not succeed in converting an 8-fold helix into a 6-fold helix by solvent exchange. However, studies need to be performed to verify if this conversion can be made in solid state. Other molecules should be tested in order to try the 8-fold helix formation. Finally, light scattering studies should be performed to solve the kinetic of crystallization of V-amylose complexes.

REFERENCES

A

Abe H., Harigaya M., Kikkawa Y., Tsuge T., Doi Y. (2005). Crystal growth and solid-state structure of poly(lactide) stereocopolymers. *Biomacromolecules* 6, 457-467.

Adebowale K.O., Lawal O.S. (2003). Functional properties and retrogradation behaviour of native and chemically modified starch of mucuna bean (Mucuna pruriens). *J. Sci. Food Agric.* 83, 1541–1546.

American Association of Cereal Chemists (2000). Approved Methods of the AACC, 10th edition, AACC, St. Paul, MN.

Agboola S., Ng D., Mills D. (2005). Characterisation and functional properties of Australian rice protein isolates. *J. Cereal Sci.* 41, 283-290.

Arnaut L.G., Formosinho S.J. (1993). Excited-state proton-transfer reactions. 1.Fundamentals and intermolecular reactions. *J. Photochem. Photobiol. A: Chem*.,75, 1-20.

Atwell W.A., Hood L.F., Lineback, D.R., Varriano-Marston E., Zobel H.F. (1988). The terminology and methodology associated with basic starch phenomena. *Cereal Foods World* 33, 306–311.

B

Banks W., Greenwood, C.T. (1972) Conformation of amylose in alkaline salt solution. *Carbohyd. Res.* 21, 229-234.

Banks W., Greenwood, C.T. (1975). *Starch and its Components*. Edinburgh: Edinburgh University Press.

Bear R.S. (1944). Complex Formation between starch and organic molecules. *J. Am. Chem. Soc. 66*, 2122-2123.

Bello-Perez L.A., Parades-Lopez O., Roger P., Colonna P. (1996). Molecular characterization of some amylopectins. *Cereal Chem*.73, 12-17.

Bello-Perez L.A., Roger P., Baud B., Colonna P. (1998a). Macromolecular features of starches determined by aqueous high-performance size exclusion chromatography. *J. Cereal Sci. 27*, 267-278.

Bello-Perez L.A., Roger P., Colonna P., Paredes-López O. (1998b). Laser light scattering of high amylose and high amylopectin materials, stability in water after microwave dispersion. *Carbohydr. Polym.* 37, 383-394.

Berne B.J., Pecora R. (1976). *Dynamic Light Scattering*, John Wiley & Sons, New York.

Bittiger H., Husemann E. (1969). Electron microscopy of crystals of amylose complexes and polyethylene. *Koll. Z. Z. Polym*. 232, 661-668.

Blanshard J., Bates D., Muhr A., Worcester D., Higgins J. (1984). Small-angle neutron-scattering studies of starch granule structure. *Carbohydr. Polym.* 4, 427-442.

Booy F.P., Chanzy H., Sarko A. (1979). Electron-diffraction study of single-crystals of amylose complexed with normal-butanol. *Biopolymers* 18, 2261-2266.

Borch J., Sarko A., Marchessault R.H. (1972). Light-scattering analysis of starch granules. *J. Coll. Int. Sci.* 41, 574-587.

Brisson J., Chanzy H., Winter W.T. (1991). The crystal and molecular-structure of vh amylose by electron-diffraction analysis. *Int. J. Biol. Macromol*. *13*, 31-39.

Buléon A., Chanzy H., Froment P. (1982). Single-crystals of cellulose-ivii - influence of the cellulose molecular-weight. *J. Polym. Sci. Polym. Phys.* 2, 1081-1088.

Buléon A., Colonna P., Planchot V., Ball S. (1998). Starch granules: structure and biosynthesis. *Int. J. Biol. Macromol*. 23, 85-112.

Buléon A., Delage M.M., Brisson J., Chanzy H. (1990). Single-crystals of V-amylose complexed with isopropanol and acetone. *Int. J. Biol. Macromol*. 12, 25-33.

Buléon A., Duprat F., Booy F.P., Chanzy H. (1984). Single-crystals of amylose with a low degree of polymerization. *Carbohydr. Polym. 4*, 161-173.

Buléon A., Pontoire B., Riekel C., Chanzy H., Helbert W., Vuong R. (1997). Crystalline ultrastructure of starch granules revealed by synchrotron radiation microdiffraction mapping. *Macromol. 30*, 3952-3954.

Burchard, W. (1994). Light Scattering Techniques. In Physical Techniques for the Study of Food Biopolymers; Ross-Murphy, S.B., Ed.; Blackie Academic and Professional: Glasgow, pp 151-213.

Burchard W., Richtering W. (1989). Dynamic light scattering from polymer solutions. *Progr. Colloid Polym. Sci.* 80, 151-163.

Burchard W., Thurn A. (1985). Heterogeneity in branching - mathematical treatment of the amylopectin structure. *Macromolecules* 18, 2072-2082.

C

Cameron R.E., Donald A.M. (1992). A small-angle X-ray scattering study of the annealing and gelatinization of starch. *Polymer* 33, 2628-2635.

Cameron R.E., Donald A.M. (1993). A small-angle X-ray scattering study of the absorption of water into the starch granule. *Carbohydr. Res.* 244, 225-236.

Cardoso M.B., Samios D., Silveira N.P. (2006). Study of protein detection and ultrastructure of brazilian rice starch during alkaline extraction. *Starch/Stärke* 58, 345-352.

Cardoso M.B., Samios D., Silveira N.P., Rodembusch F.S., Stefani V. (2007a). ESIPT-exhibiting protein probes: a sensitive method for rice proteins detection during starch extraction. *Photochem. Photobiol. Sci*. 6, 99-102.

Cardoso, M.B., Putaux, J.L., Nishiyama, Y., Helbert, W., Hÿtch, M., Silveira, N.P., Chanzy, H. (2007b). Single crystals of V-amylose complexed with α-naphthol. *Biomacromolecules*, in press.

Chinachoti P., White V.A., Lo L., Stengle, T.R. (1991). Application of high-resolution carbon-13, oxygen-17, and sodium-23 nuclear magnetic resonance to study the influence of water, sucrose, and sodium chloride on starch gelatinization. *Cereal Chem.* 68, 238–244.

Chiou H., Fellowsa C.M., Gilberta R.G., Fitzgerald M. A. (2005). Study of rice-starch structure by dynamic light scattering in aqueous solution. *Carbohydr. Polym.* 61, 61-71.

Chiou H., Martin M., Fitzgerald M. (2002). Effect of purification methods on rice starch structure. *Starch/Stärke* 54, 415-420.

Cho J., Heuzey M., Bérgin A., Carreau P. (2006). Viscoelastic properties of chitosan solutions: Effect of concentration and ionic strength *J. Food Eng.* 74, 500-515.

Choi S.G., Kerr W.L. (2004). Swelling characteristics of native and chemically modified wheat starches as a function of heating temperature and time. *Starch* 56, 181–189.

Christoff M., Silveira N.P., Samios D. (2001). Fluorescence and light scattering studies on the aggregation of sodium cholate in the presence of low molecular weight poly(ethylene oxide). *Langmuir* 17, 2885-2888.

Cooke D., Gidley M. J. (1992). Loss of crystalline and molecular order during starch gelatinization: origin of the enthalpic transition. *Carbohydr. Res.* 227, 103-112.

Cremer D., Pople J.A. (1975). General definition of ring puckering coordinates. *J. Am. Chem. Soc.* 97, 1354-1358.

D

Dang J.M.C., Copeland L. (2003). Imaging rice grains using atomic force microscopy. *J. Cereal Sci.* 37, 165-170.

Dimler R.J., Davis H.A., Rist C.E., Hilbert G.E. (1944). Production of starch from wheat and other cereal flours. *Cereal Chem.* 21, 430.

Donald A.M., Kato K.L., Perry P.A., Waigh T.A. (2001). Scattering studies of the internal structure of starch granules. *Starch/Stärke* 53, 504-512.

Donovan J. (1979). Phase transitions of the starch-water system. *Biopolymers*, *18*, 263-275.

E

Elias M.C., Dias A.R.G., Fagundes C.A.A. (2005). Manejo operacional para preservação da qualidade na pós-colheita dos grãos de arroz. In: Elias, M.C. (org) & Lorini, I. (org.). Qualidade de arroz na pós-colheita. Abrapós-UFPel, Pelotas, Capítulo 1, p. 31-60.

Erickson H.A., Klug A. (1971). Measurement and compensation of defocusing and aberrations by fourier processing of electron micrographs. *Phil. Trans. R. Soc. Lond. Biol*. 261, 105-118.

Evertsson H., Nilsson S., Holmberg C., Sundelöf L.O. (1996). Temperature effects on the interactions between EHEC and SDS in dilute aqueous solutions. Steady-state fluorescence quenching and equilibrium dialysis investigations. *Langmuir* 12, 5781-5789.

F

Fishman M.L., Hoagland P.D. (1994). Characterization of starches dissolved in water by microwave-heating in a high-pressure vessel. *Carbohydr. Polym*. 23, 175-183.

Formosinho S.J., Arnaut L.G. (1993). Excited-state proton-transfer reactions. 2. Intramolecular reactions. *J. Photochem. Photobiol. A: Chem*. 75, 21-48.

Foster J.F. (1965). In R. L. Whistler, & E. F. Paschall (Eds.), Starch: Chemistry and technology (pp. 1–349). New York: Academic Press.

Foster J.F., Hixon R.M. (1944). Relationship between solution viscosity and molecular weight in the amylose series. *J. Am. Chem. Soc.* 66, 557-560.

French, D. (1972). Fine structure of starch and its relationship to the organization of starch granules.*J. Jpn. Soc. Starch Sci.* 19, 8-25.

French D. (1984). Organization of starch granules. In *Starch: Chemistry and technology*, Whistler, R.L., Paschall, E. F., Bemiller, J. N. (Eds.), 2nd ed., New York, Academic Press, 183-247.

Fujita S., Lida T., Fujiyama G. (1992). Relationship between gelatinization temperature and enthalpy of starch from graminous crops by DSC. *Starch/Stärke* 44, 456-461.

G

Galinsky G., Burchard W. (1995). Starch fractions as examples for nonrandomly branched macromolecules .1. Dimensional properties. *Macromolecules* 28, 2363-2370.

Gallant D.J., Bouchet B., Baldwin P.M. (1997). Microscopy of starch: Evidence of a new level of granule organization. *Carbohydr. Polym. 32*, 177-191.

Gallant D.J., Bouchet B., Buléon A., Perez S. (1992). Physical characteristics of starch granules and susceptibility to enzymatic degradation. *Eur. J. Clin. Nutr.* 46, S3-S16.

Gallant D., Guilbot A. (1969). Application de l'oxydation periodique à l'étude de l'ultrastructure de l'amidon de pomme de terre. of periodate oxidation to ultrastructural study of potato starch granules. *J. Microscopie* 8, 549-568.

Gessler K., Uson I., Takaha T., Krauss N., Smith S.S., Okada S., Sheldrick G.M., Saenger W. (1999). V-amylose at atomic resolution: X-ray structure of a cycloamylose with 26 glucose residues (cyclomaltohexaicosaose). *Proc. Natl. Acad. Sci. USA* 96, 4246-4251.

Gidley M.J., Bulpin P.V. (1987). Crystallization of maltooligosaccharides as models of the crystalline forms of starch - minimum chain-length requirement for the formation of double helices. *Carbohydr. Res.* 161, 291-300.

Godet M.C., Buléon A., Tran V., Colonna P. (1993a). Structural features of fatty acid-amylose complexes. *Carbohydr. Polym.* 21, 91-95.

Godet M.C., Tran V., Delage M.M., Buléon A. (1993b). Molecular modeling of the specific interactions involved in the amylose complexation by fatty-acids. *Int. J. Biol. Macromol.* 15,11-16.

Grieser F., Drummond C.J. (1988). The physicochemical properties of self-assembled surfactant aggregates as determined by some molecular spectroscopic probe techniques. *J. Phys. Chem.* 92, 5580-5593.

H

Han J.A., Lim S.T. (2004). Structural changes in corn starches during alkaline dissolution by vortexing. *Carbohydr. Polym.* 64, 190–196.

Hanashiro I., Abe J., Hizukuri S. (1996). A periodic distribution of the chain length of amylopectin as revealed by high-performance anion-exchange chromatography. *Carbohydr. Res.* 283, 151-159.

Haworth W.N., Peat S., Sagrott P.E. (1946). A new method for the separation of the amylose and amylopectin components of starch. *Nature*, *3975*, 157.

Helbert, W. (1994). Doctoral dissertation, Joseph Fourier University of Grenoble, France,.

Helbert W., Chanzy H. (1994). Single-crystals of v-amylose complexed with n-butanol or n-pentanol - structural features and properties. *Int. J. Biol. Macromol*.,16, 207-213.

Helbert W., Nishiyama Y., Okano T., Sugiyama J. (1998a). Molecular imaging of *Halocynthia papillosa* cellulose. *J. Struct. Biol.*, *124*, 42-50.

Helbert W., Sugiyama J., Kimura S., Itoh T. (1998b). High-resolution electron microscopy on ultrathin sections of cellulose microfibrils generated by glomerulocytes in Polyzoa vesiculiphora. *Protoplasma* 203, 84-90.

Hellweg T., Eimer W. (1998). The micro-structures formed by Ni2+-AOT/cyclohexane/water microemulsions: a light scattering study. *Coll. Surf. A 136*, 97-107.

Hizukuri, S. (1985). Relationship between the distribution of the chain-length of amylopectin and the crystalline-structure of starch granules. *Carbohydr. Res.*141, 295-306.

Hizukuri S. (1986). Polymodal distribution of the chain lengths of amylopectins, and its significance. *Carbohydr. Res.*147, 342-347.

Hizukuri S., Takeda Y., Abe J., Hanashiro I., Matsunobu G., Kiyota H. (1997). In: Frazier P.J., Richmond P., Donald A.M., editors. *Starch: Structure and Functionality.* London:Royal Society of Chemistry.

Holler M.G., Campo L.F., Brandelli A., Stefani V. (2002). Synthesis and spectrocopic characterisation of 2-(2'-hydroxyphenyl) benzazole isothiocyanates as new fluorescent probes for proteins. *J. Photochem*. *Photobiol. A: Chem*. 149, 217-225.

Hoover R., Vasanthan T. (1994). The effect of annealing on the physicochemical properties of wheat, oat, potato and lentil starches. *J. Food Biochem.* 17, 303-325.

Huang R.M., Chang W.H., Chang Y.H., Lii C.Y. (1994). Phase transitions of rice starch and flour gels. *Cereal Chem.* 71, 202–207.

Hulleman S.H.D., Helbert W., Chanzy H. (1996). Single crystals of V amylose complexed with glycerol. *Int. J. Biol. Macromol*. 18, 115-122.

I

Imai T., Putaux J-L., Sugiyama J. (2003). Geometric phase analysis of lattice images from algal cellulose microfibrils. *Polymer* 44, 1871-1879.

Imberty A., Buléon A., Tran V., Perez S. (1991). Recent advances in knowledge of starch structure. *Starch/Staerke* 43, 375-384.

Imberty A., Chanzy H., Perez S., Buléon A., Tran V. (1988). The double-helical nature of the crystalline part of A-starch. *J. Mol. Biol.* 201, 365-378.

IUPAC-IUB (1983). Symbols for specifying the conformation of polysaccharide chains. Recommendations 1981. *Eur. J. Biochem.* 131, 5-7.

J

Jacob J., Gessler K., Hoffmann D., Sanbe H., Koizumi K., Smith S.M., Takaha T., Saenger W. (1998). Strain-induced "band flips" in cyclodecaamylose and higher homologues. *Angew. Chem. Int. Ed. 37*, 606-609.

Jakes J. (1995). Regularized positive exponential sum (REPES) program - A way of inverting laplace transform data obtained by dynamic light scattering. *Collec. Czechos. Chem. Commun*. 60, 1781-1797.

Juliano B.O. (1984). Rice starch: production, properties and uses. In *Starch: chemistry and technology*. R.L. Whistler, J.N. BeMiller & E. F. Paschall eds., Academic Press, NY, pp 507-528.

K

Kassenbeck, P. (1978). Contribution to knowledge on distribution of amylose and amylopectin in starch granules. *Starch* 30, 40-46.

Kaur L., Singh J., Singh N. (2005). Effect of glycerol monostearate on the physico-chemical, thermal, rheological and noodle making properties of corn and potato starches. *Food Hydrocoll.*, 19, 839–849.

Kaur L., Singh N., Singh, J. (2004). Factors influencing the properties of hydroxypropylated potato starches. *Carbohyd. Polym.* 55, 211–223.

Kaur L., Singh N., Sodhi, N. S. (2002). Some properties of potatoes and their starches II. Morphological, thermal and rheological properties of starches. *Food Chem.* 79, 183–192.

Koizumi K., Fukuda M., Hizukuri S. (1991). Estimation of the distributions of chain-length of amylopectins by high-performance liquid-chromatography with pulsed amperometric detection. *J. Chromatogr*. 585, 233-238.

Krueger B.R., Knutson C.A., Inglett G.E., Walker C.E. (1987). A differential scanning calorimetry study on the effect of annealing on gelatinization behaviour of corn starch. *J.Food Sci.* 52, 715–718.

L

l'Anson K.J., Miles M.J., Morris V.J., Ring, S.G. (1988). A study of amylose gelation using a synchrotron X-ray source. *Carbohyd. Polym.* 8, 45–53.

Lim S., Lee J., Shin D., Lim H.S. (1999). Comparison of protein extraction solutions for rice starch isolation and effects of residual protein content on starch pasting properties. *Starch/Stärke* 51, 120-125.

Liu H., Lelièvre J., Ayoung C.W. (1991). A study of starch gelatinization using differential scanning calorimetry, X-ray, and birefringence measurements. *Carbohydr. Res.* 210, 79-87.

Liu Q., Weber E., Currie V., Yada R. (2003). Physicochemical properties of starches during potato growth. *Carbohydr. Polym.* 51, 213–221.

Lugay C.J., Juliano B.O. (1965). Crystallinity of rice starch and its fractions in relation to gelatinization and pasting characteristics. *J. Appl. Polym. Sci.*, *9*, 3775-3780.

Lumdubwong N., Seib P.A. (2000). Rice starch isolation by alkaline protease digestion of wet-milled rice flour. *J. Cereal Sci.* 31, 63-74.

M

Manley R.S.J. (1964). Chain folding in amylose crystals. *J. Polym. Sci. Part A* 2, 4503-4515.

Marchant J.L., Blanshard J.M.V. (1978). Studies of the dynamics of the gelatinization of starch granules employing a small angle light scattering system. *Starch/Stärke* 30, 257–264.

Matsunaga N., Seib P.A. (1997). Extraction of wheat starch with aqueous sodium hydroxide.*Cereal Chem. 74*, 851-857.

Mikus F.F., Hixon R.M., Rundle R.E. (1946). The complexes of fatty acids with amylose. *J. Am. Chem Soc.* 68*,* 1115-1123.

Miller D., Sugiyama J., Brisson J., Chanzy H. (1990). in "Electron Crystallography of Organic Molecules", J. R. Fryer and D. L. Dorset eds., Kluwer Academic Publishers, pp 189-195.

Mistry A.H., Eckhoff S.R. (1992a). Characteristics of alkali-extracted starch obtained from corn flour.*Cereal Chem.* 69, 296-303.

Mistry A.H., Eckhoff S.R. (1992b). Alkali debranning of corn to obtain corn bran. *Cereal Chem.* 69, 202-205.

Morelon X., Battu S., Salesse C., Begaud-Grimaud G., Cledat D., Cardot P.J.P. (2005). Sedimentation field flow fractionation monitoring of rice starch amylolysis.*J. Chromatogr. A* 1093, 147-155.

Murphy V.G., Zaslow B., French A.D. (1975). Structure of v-amylose dehydrate - combined x-ray and stereochemical approach. *Biopolymers* 14, 1487-1501.

N

Nakanishi Y., Norisuye T., Teramoto A., Kitamura S. (1993). Conformation of amylose in dimethyl-sulfoxide. *Macromolecules* 26, 4220-4225.

Nakazawa F., Noguchi S., Takahashi J., Takeda M. (1984). Gelatinization and retrogradation of rice starch studied by differential scanning calorimetry. *Agric. Biologic. Chem.* 48, 201-203.

Nayouf M., Loisel C., Doublier J.L. (2003). Effect of thermomechanical treatment on the rheological properties of crosslinked waxy corn starch. *J. Food Eng.* 59, 209-219.

Nimz O., Gessler K., Uson I., Sheldrick G.M., Saenger W. (2004). Inclusion complexes of V-amylose with undecanoic acid and dodecanol at atomic resolution: X-ray structures with cycloamylose containing 26 D-glucoses (cyclohexalcosaose) as host. *Carbohydr. Res.* 339, 1427-1437.

Nishiyama Y., Langan P., Chanzy H. (2002). Crystal structure and hydrogen-bonding system in cellulose 1 beta from synchrotron X-ray and neutron fiber diffraction *J. Am. Chem. Soc.* 124, 9074-9082.

Noda T., Takahata Y., Sato T.T., Ikoma H., Mochinda H. (1996). Physicochemical properties of starches from purple and orange fleshed sweet potato roots at two levels of fertilizer. *Starch/Stärke* 48, 395-399.

Nosé S. (1984). A molecular-dynamics method for simulations in the canonical ensemble. *Mol. Phys.* 52, 255-268.

Nuessli J., Putaux J-L., Le Bail P., Buléon A. (2000). Crystal structure of amylose complexes with small ligands. *Int. J. Biol. Macromol.* 33, 227-234.

O

Ong M.H., Jumel K., Tokarczuk P.F., Blanshard J.M.V., Harding S.E. (1994). Simultaneous determinations of the molecular-weight distributions of amyloses and the fine-structures of amylopectins of native starches. *Carbohydr. Res.* 260, 99-117.

Oostergetel G.T, van Bruggen E.F. (1989). On the origin of a low-angle spacing in starch. *Starch/Staerke* 41, 331-335.

Oostergetel G.T, van Bruggen E.F. (1993). The crystalline domains in potato starch granules are arranged in a helical fashion. *Carbohydr. Polym.* 21, 7-12.

P

Paixao T.R.L.C., Matos R.C., Bertotti M. (2003). Development of a dual-band amperometric detector for determination of ascorbic acid and glucose. *Electroanalysis* 15, 1884-1889.

Perera C., Hoover R. (1999). Influence of hydroxypropylation on retrogradation properties of native, defatted and heat–moisture treated potato starches. *Food Chem.* 64, 361–375.

Perera C., Hoover R., Martin A.M. (1997). The effect of hydroxypropylation on the structure and physicochemical properties of native, defatted and heat- moisture treated potato starches. *Food Res. Internat.* 30, 235–247

Perez S., Mazeau K., du Penhoat C.H. (2000). The three-dimensional structures of the pectic polysaccharides. *Plant Physiol. Biochem. 38*, 37-55.

Pfannemüller B. (1987). Influence of chain-length of short monodisperse amyloses on the formation of A-type and B-type x-ray-diffraction patterns. *Int. J. Biol. Macromol*. 9, 105-108.

Popov D., Burghammer M., Buléon A., Montesanti N., Putaux J.-L., Riekel C. (2006). A-amylose single crystals: Unit cell refinement from synchrotron radiation microdiffraction data. *Macromolecules* 39, 3704-3706.

Puchongkavarin H., Varavinit S., Bergthaller W. (2005). Comparative study of pilot scale rice starch production by an alkaline and an enzymatic process. *Starch/Stärke* 57, 134-144.

Putaux J.L., Molina-Boisseau S., Momaur T., Dufresne A. (2003). Platelet nanocrystals resulting from the disruption of waxy maize starch granules by acid hydrolysis. *Biomacromolecules* 4, 1198-1202.

Q

Qi X., Tester R.F., Snape C.E., Ansell R. (2003). Molecular basis of the gelatinisation and swelling characteristics of waxy rice starches grown in the same location during the same season. *J. Cereal Sci*. 37, 363-376.

Quigley G.J., Sarko A. Marchess R.H. (1970). Crystal and molecular structure of maltose monohydrate. *J. Am. Chem. Soc.* 92, 5834-5839.

Quintino M.D.S.M., Winnischofer H., Nakamura M., Araki K., Toma H.E., Angnes L. (2005). Amperometric sensor for glucose based on electrochemically polymerized tetraruthenated nickel-porphyrin. *Anal. Chim. Acta* 539, 215-222.

R

Rappe A.K., Casewit C.J., Colwell K.S., Goddard W.A., Skiff W.M. (1992). Uff, a full periodic-table force-field for molecular mechanics and molecular-dynamics simulations. *J. Am. Chem. Soc.* 114, 10024-10035.

Rappe A.K., Goddard W.A. (1991). Charge equilibration for molecular-dynamics simulations. *J. Phys. Chem.* 95, 3358-3363.

Rappenecker G., Zugenmaier P. (1981). Conformation and packing analysis of polysaccharides and derivatives .8. Detailed refinement of the crystal-structure of vh-amylose. *Carbohydr. Res*. 89, 11-19.

Revol J.F., Gardner K.H., Chanzy H. (1988). Beta-chitin - molecular imaging at 0.35-nm resolution. *Biopolymers* 27, 345-350.

Ring S.G., l'anson K.J., Morris V.J. (1985). Static and dynamic light-scattering studies of amylose solutions. *Macromolecules* 18, 182-188.

Ríos M.A., Ríos M.C. (1998). Ab initio study of the hydrogen bond and proton transfer in 2-(2'-hydroxyphenyl)benzothiazole and 2-(2'-hydroxyphenyl) bezimidazole. *J. Phys. Chem. A* 102, 1560-1567.

Robin J.P., Mercier C., Charbonniere R., Guilbot A. (1974). Lintnerized starches gel-filtration and enzymatic studies of insoluble residues from prolonged acid treatment of potato starch. *Cereal Chem.* 51, 389-406.

Robin J.P., Mercier C., Duprat F., Charbonniere R., Guilbot A. (1975). Lintnerized starches - chromatographic and enzymatic studies of insoluble residues from acid-hydrolysis of various cereal starches, particularly waxy maize starch. *Starch/Staerke* 27, 36-45.

Robinson B., Hargreaves A. (1964). Crystal structure of alpha-naphthol. *Acta Cryst. 17*, 944-946.

Rodembusch F.S., Leusin F.P., Bordignon L.B., Gallas M.R., Stefani V. (2005a). New fluorescent monomers and polymers displaying an intramolecular proton-transfer mechanism in the electronically excited state (ESIPT). Part II. Synthesis, spectroscopic characterization and solvatochromism of new benzazolylvinylene derivatives. *J. Photochem. Photobiol A: Chem*. 173, 81-92.

Rodembusch F.S., Medina L.F.C., Brandelli A., Stefani V. (2005b). Synthesis and spectroscopic characterisation of new ESIPT fluorescent protein probes. *Photochem. Photobiol. Sci*. 4, 254-259.

Roger P., Bello-Perez L.A., Colonna P. (1999). Contribution of amylose and amylopectin to the light scattering behaviour of starches in aqueous solution. *Polymer* 40, 6897-6909.

Roger P., Colonna P. (1992). The influence of chain-length on the hydrodynamic behavior of amylose. *Carbohydr. Res.* 227, 73-83.

Roger P., Colonna P. (1996). Molecular weight distribution of amylose fractions obtained by aqueous leaching of corn starch. *Int. J. Biol. Macromol.* 19, 51-61.

Roger P., Tran, V., Lesec J, Colonna P. (1996). Isolation and Characterisation of Single Chain Amylose. *J. Cereal Sci. 24*, 247–262

Russel P.L., Oliver G. (1989). The effect of pH and Nacl content on starch gel ageing. A study by differential scanning calorimetery and rheology. *J. Cereal Sci.* 10, 123-138.

S

Saito Y., Okano T., Chanzy H., Sugiyama J. (1995). Structural study of alpha-chitin from the grasping spines of the arrow worm (sagitta spp). *J. Struct. Biol*. 114, 218-228.

Sarko A., Biloski A. (1980). Crystal structure of the KOH-amylose complex. *Carbohydr. Res.* 79, 11-21.

Saxton W.O., Baumeister W. (1982). The correlation averaging of a regularly arranged bacterial-cell envelope protein. *J. Microsc.* 127, 127-138.

Saxton W.O., Pitt T.J., Horner M. (1979). Digital image-processing - semper system. *Ultramicroscopy* 4, 343-353.

Seo J., Kim S., Park S., Park S.Y. (2005). Tailoring the excited-state intramolecular proton transfer (ESIPT) fluorescence of 2-(2'-hydroxyphenyl)benzoxazole derivatives. *Bull. Korean Chem. Soc*. 26, 1706-1710.

Seow C.C., Thevamalar K. (1993). Internal plasticization of granular rice starch by hydroxypropylation: Effects on phase transitions associated with gelatinization. *Starch* 45, 85-88.

Sevenou O., Hill S.E., Farhat I.A., Mitchell J.R. (2002). Organisation of the external region of the starch granule as determined by infrared spectroscopy. *Int. J. Biol. Macromol.* 31, 79-85.

Sheldrick G.M., Schneider T.R. (1997). SHELXL: High-resolution refinement. *Methods Enzymol.* 277, 319-343.

Shiotsubo T., Takahashi K. (1984). Differential thermal analysis of potato starch gelatinization. *Agric. Biologic. Chem.* 48, 9–17.

Singh N., Chawla D., Singh J. (2004). Influence of acetic anhydride on physicochemical, morphological and thermal properties of corn and potato starch. *Food Chem.* 86, 601–608.

Singh N., Kaur, L. (2004). Morphological, thermal and rheological properties of potato starch fractions varying in granule size. *J. Sci. Food Agric.* 84, 1241-1252.

Singh J., Kaur L., McCarthy O.J. (2007). Factors influencing the physico-chemical, morphological, thermal and rheological properties of some chemically modified starches for food applications - A review. *Food Hydrocoll.* 21, 1-22.

Singh J., Kaur L., Singh N. (2004). Effect of acetylation on some properties of corn and potato starches. *Starch/Stärke* 56, 586-601.

Singh J., Singh N. (2001). Studies on the morphological, thermal and rheological properties of starch from some Indian potato cultivars. *Food Chem.* 75, 67-77.

Singh J., Singh, N. (2003). Studies on the morphological and rheological properties of granular cold water soluble corn and potato starches. *Food Hydrocoll.* 17, 63–72.

Sirota E.B. (2007). Polymer crystallization: Metastable mesophases and morphology. *Macromolecules* 40, 1043-1048.

Sodhi N.S., Singh N. (2003). Morphological, thermal and rheological properties of starches separated from rice cultivars grown in India. *Food Chem.* 80, 99-108.

Sonneveld E.J., Visser J.W. (1975). Automatic collection of powder data from photographs. *J. Appl. Cryst.* 8, 1-7.

Sterling C. (1962). Low angle spacing in starch. *J. Polym. Sci.* 56, S10.

Stevens D.J., Elton G.A.H. (1971). Thermal properties of starch/water system. I. Measurement of heat of gelatinization by differential scanning calorimetry. *Starch/Stärke* 23, 8-11.

Sugiyama J., Harada H., Fujiyoshi Y., Uyeda N. (1985). Lattice images from ultrathin sections of cellulose microfibrils in the cell-wall of valonia-macrophysa kutz. *Planta* 166, 161-168.

Suortti Y., Gorenstein M.V., Roger P. (1998). Determination of the molecular mass of amylose. *J. Chromatogr. A.* 828, 515-521.

Svegmark K., Hermansson A.M. (1993). Microstructure and rheological properties of composites of potato starch granules and amylose - a comparison of observed and predicted structures. *Food Struct.* 12, 181-193.

T

Takeda Y., Hizukuri S., Takeda C., Suzuki A. (1987). Structures of branched molecules of amyloses of various origins, and molar fractions of branched and unbranched molecules. *Carbohydr. Res.* 165,139-145.

Takeo K., Kuge T. (1969). Complexes of starchy materials with organic compounds .3. X-ray studies on amylose and cyclodextrin complexes. *Agr. Biol. Chem. 33*, 1174-1180.

Takeo K., Kuge T. (1970). Conformation of peracetylated cyclodextrins. *Agr. Biol. Chem*. *34*, 1416-1419.

Tako M., Hizukuri S. (2002). Gelatinization mechanism of potato starch. *Carbohydr. Res.* 48, 397-401.

Tanaka Y., Sugimoto T., Ogawa M., Kasai Z. (1980). Isolation and characterization of two types of protein bodies in the rice endosperm. *Agric. Biol. Chem.* 44, 1633-1639.

Tester R.F., Morrison W.R. (1990). Swelling and gelatinization of cereal starches. *Cereal Chem.* 67, 558–563.

Tester R.F., Karkalas J., Qi X. (2004). Starch-composition, fine structure and architecture. *J. Cereal Sci.* 39, 151–165

Thirathumthavorn D., Charoenrein S. (2006). Thermal and pasting properties of native and acid-treated starches derivatized by 1-octenyl succinic anhydride. *Carbohydr. Polym.*66, 258-265.

Thon F. (1971). in "Electron Microscopy in Materials Science", U. Valdre ed., Academic Press, London, pp 571-625.

Thurn A., Burchard W. (1985). Heterogeneity in branching of amylopectin. *Carbohydr. Polym.* 5, 441-460.

Tietz L.A., Carter C. B., McKernan, S. (1995). Top-bottom effects in double diffraction. *Ultramicroscopy* 60, 241-246

Tomasik P., Schilling C.H. (1998a). Complexes of starch with inorganic guests. *Adv. Carbohydr. Chem. Biochem.* 53, 263-343.

Tomasik P., Schilling C.H. (1998b). Complexes of starch with organic guests. *Adv. Carbohydr. Chem. Biochem*. 53, 345-426.

V

Verlet L. (1967). Computer experiments on classical fluids. I. Thermodynamical properties of lennard-jones molecules. *Phys. Rev.* 159, 98-103.

Vollmer F., Rettig W., Birckner E. (1994). Photochemical mechanisms producing large fluorescence Stokes shifts. *J. Fluorescence* 4, 65-71.

W

Wada K., Takahashi K., Shirai K., Kawamura A. (1979). Differential thermal analysis (DTA) applied to examining gelatinization of starches in foods. *J. Food Sci.* 44, 1366–1368.

Wang S., Gao W., Chen H., Xiao P. (2005). New starches from *Fritillaria* species medicinal plants. *Carbohydr. Polym.* 61, 111-114.

Wang L., Wang Y.J. (2004). Application of high-intensity ultrasound and surfactants in rice starch isolation. *Cereal Chem.* 81, 104-144.

Welland E.L., Donald A.M. (1991). Single-crystals of V-amylose. *Int. J. Biol. Macromol.* 13, 69-72.

Whittam M.A., Oxford P.D., Ring S.C., Clark S.A., Parker M.L., Cairns P., Miles M. (1989). Aqueous dissolution of crystalline and amorphous amylose alcohol complexes. *Int. J. Biol. Macromolecules* 11, 339-344.

Winnik F.M., Winnik M.A., Takuze S. (1987). Interaction of hydroxypropylcellulose with aqueous surfactants: fluorescence probe studies and a look at pyrene-labeled polymer. *J. Phys. Chem.* 91, 594-597.

Winter W.T., Chanzy H., Putaux J-L., Helbert W. (1998). Inclusion compounds of amylose. *Polym. Prepr.* 39, 703.

Winter W.T., Sarko A. (1974). Crystal and molecular-structure of V-anhydrous amylose. *Biopolymers* 13, 1447-1460.

Wong K.S., Jane J. (1997). Quantitative analysis of debranched amylopectin by HPAEC-PAD with a postcolumn enzyme reactor. *J. Liquid. Chromatogr.* 20, 297-310.

Wu H.C.H., Sarko A. (1978a). Packing analysis of carbohydrates and polysaccharides .9. Double-helical molecular-structure of crystalline A-amylose. *Carbohydr. Res.* 61, 27-40.

Wu H.C.H., Sarko A. (1978b). Packing analysis of carbohydrates and polysaccharides .8. Double-helical molecular-structure of crystalline B-amylose. *Carbohydr. Res.* 61, 7-25.

Y

Yalpani, M. (1988). *Polysaccharides: Syntheses, Modifications and Structure–Properties Relations. Studies in Organic Chemistry*, vol. 36. Amsterdam: Elsevier.

Yamaguchi M., Kainuma K., French D. (1979). Electron-microscopic observations of waxy maize starch. *J. Ultrastruct. Res.* 69, 249-261.

Yamamoto H., Makita E., Oki Y., Otani M. (2006). Flow characteristics and gelatinization kinetics of rice starch under strong alkali conditions. *Food Hydrocoll.* 20, 9-20

Yamashita Y. (1965). Single crystals of amylose v complexes.*J. Polym. Sci. Part A 3*, 3251-3260.

Yamashita Y., Hirai N. (1966). Single crystals of amylose V complexes .2. Crystals with 71 helical configuration. *J. Polym. Sci. Part A-2* 4, 161-171.

Yamashita Y., Monobe K. (1971). Single crystals of amylose v complexes .3. Crystals with 81 helical configuration. *J. Polym. Sci. Part A-2* 9, 1471-1481.

Yamashita Y., Ryugo J., Monobe K. (1973). Electron-microscopic study on crystals of amylose v complexes. *J. Electron Microsc.* 22, 19-26.

Yang C.C., Lai H.M., Lii C.Y. (1984). The modified alkaline steeping method for the isolation of rice starch. *Food Sci.* 11, 158-162.

Yang C., Meng B., Chen M.Q., Liu X., Hua Y., Ni Z.. (2006). Laser-light-scattering study of structure and dynamics of waxy com amylopectin in dilute aqueous solution. *Carbohydr. Polym.* 64, 190-196.

Yeh A.I., Yeh S.L. (1993). Property differences between cross-linked and hydroxypropylated rice starches. *Cereal Chem.* 70, 596.

Yook C., Pek U.H., Park K.H. (1993). Gelatinization and retrogradation characteristics of hydroxypropylated cross-linked rices. *J. Food Sci.* 58, 405–407.

Yu L.P., Rollings J.E. (1987). Low-angle laser-light scattering-aqueous size exclusion chromatography of polysaccharides - molecular-weight distribution and polymer branching determination. *J. Appl. Polym. Sci*. 33, 1909-1921.

Yu L.P., Rollings J.E. (1988). Quantitative branching of linear and branched polysaccharide mixtures by size exclusion chromatography and online low-angle laser-light scattering detection. *J. Appl. Polym. Sci.* 35, 1085-1102.

Yu X.C., Houtman C., Atalla R.H. (1996). The complex of amylose and iodine. *Carbohydr. Res.* 292,129-141.

Yuan R.C., Thompson D.B., Boyer C.D. (1993). Fine-structure of amylopectin in relation to gelatinization and retrogradation behavior of maize starches from 3 wx-containing genotypes in 2 inbred lines. *Cereal Chem.* 70, 81-89.

Z

Zaslow B. (1963). Characterization of a 2nd helical amylose modification. *Biopolymers*, 1, 165-169.

Zaslow B., Murphy V.G., French A.D. (1974). V amylose-H_2O system - structural-changes resulting from hydration. *Biopolymers 13*, 779-790.

Zobel H.F., Young S.N., Rocca, L.A. (1988). Starch gelatinization. An X-ray diffraction study. *Cereal Chem.* 66, 443-446.

ANNEX 1

d-spacings corresponding to *hk*0 reflections from electron diffraction patterns recorded at room temperature on untilted $V_{isopropanol}$ single crystals. The experimental *d*-spacings (d_{obs}) are compared with the values (d_{cal}) calculated from the parameters of the refined unit cell.

h k l	d_{obs} **(nm)**	d_{cal} **(nm)**	$\lvert d_{obs}-d_{cal} \rvert$ **(nm)**
1 1 0	1.973	2.045	0.072
2 1 0	1.285	1.309	0.024
1 2 0	1.285	1.309	0.024
2 2 0	1.023	1.022	0.001
0 2 0	1.473	1.475	0.002
2 0 0	1.404	1.418	0.014
1 3 0	0.921	0.929	0.008
2 3 0	0.807	0.808	0.001
3 3 0	0.685	0.681	0.004
3 2 0	0.796	0.796	0.000
3 1 0	0.901	0.900	0.001
4 1 0	0.692	0.689	0.003
3 4 0	0.579	0.581	0.002
1 4 0	0.712	0.714	0.002
1 5 0	0.575	0.578	0.003
2 5 0	0.547	0.545	0.002
3 5 0	0.498	0.500	0.002
4 5 0	0.453	0.453	0.000
5 1 0	0.556	0.557	0.001
5 2 0	0.530	0.529	0.001
5 3 0	0.491	0.491	0.000
5 4 0	0.452	0.498	0.004
6 0 0	0.472	0.472	0.000
6 1 0	0.467	0.466	0.001
6 2 0	0.449	0.450	0.001
0 6 0	0.492	0.491	0.001
1 6 0	0.482	0.484	0.002
2 6 0	0.468	0.464	0.004
3 6 0	0.437	0.436	0.001

ANNEX 2

d-spacings corresponding to *hkl* reflections from electron diffraction patterns recorded at room temperature on $V_{\alpha\text{-naphthol}}$ single crystals. The experimental *d*-spacings (d_{obs}) are compared with the values (d_{cal}) calculated from the parameters of the refined unit cell.

h k l	d_{obs} (nm)	d_{cal} (nm)	$\lvert d_{obs}-d_{cal} \rvert$ (nm)
2 0 0	1.157	1.161	0.004
2 1 0	1.042	1.039	0.003
2 2 0	0.824	0.822	0.002
3 1 0	0.736	0.735	0.001
3 2 0	0.646	0.645	0.001
4 0 0	0.582	0.581	0.001
2 2 1	0.570	0.569	0.001
4 1 0	0.565	0.563	0.002
3 3 0	0.546	0.548	0.002
3 1 1	0.538	0.538	0.000
4 2 0	0.520	0.520	0.000
3 2 1	0.500	0.499	0.001
4 3 0	0.466	0.465	0.001
4 1 1	0.459	0.458	0.001
5 1 0	0.456	0.455	0.001
4 2 1	0.436	0.434	0.002
5 2 0	0.432	0.431	0.001
4 4 0	0.409	0.411	0.002
5 3 0	0.396	0.399	0.003
5 1 1	0.395	0.395	0.000
6 0 0	0.390	0.391	0.001
6 1 0	0.383	0.382	0.001
6 2 0	0.369	0.368	0.001
5 4 0	0.362	0.362	0.000
6 0 1	0.349	0.348	0.001
6 3 0	0.348	0.347	0.001
6 1 1	0.337	0.344	0.007
6 2 1	0.333	0.333	0.000
5 5 0	0.329	0.329	0.000
7 1 0	0.328	0.329	0.001
6 4 0	0.323	0.322	0.001
7 2 0	0.320	0.319	0.001
7 3 0	0.306	0.305	0.001
6 4 1	0.299	0.298	0.001

6 5 0	0.298	0.298	0.000
7 2 1	0.296	0.296	0.000
8 0 0	0.292	0.291	0.001
7 4 0	0.289	0.288	0.001
8 1 0	0.289	0.288	0.001
4 4 2	0.287	0.284	0.003
7 3 1	0.285	0.285	0.000
5 3 2	0.280	0.280	0.000
8 2 0	0.278	0.282	0.004
6 5 1	0.278	0.278	0.000
6 6 0	0.273	0.274	0.001
8 3 0	0.272	0.272	0.000
7 5 0	0.271	0.270	0.001
6 2 2	0.269	0.269	0.000
8 4 0	0.260	0.260	0.000
6 6 1	0.260	0.259	0.001
8 3 1	0.257	0.257	0.000
9 1 0	0.257	0.256	0.001
5 5 2	0.253	0.253	0.000
7 1 2	0.253	0.256	0.003
7 6 0	0.252	0.252	0.000
9 2 0	0.250	0.252	0.002
6 4 2	0.250	0.249	0.001
8 5 0	0.246	0.246	0.000
9 3 0	0.245	0.245	0.000
7 7 0	0.235	0.235	0.000
8 6 0	0.233	0.232	0.001
10 0 0	0.232	0.232	0.000
8 2 2	0.229	0.229	0.000
10 2 0	0.225	0.228	0.003
10 5 0	0.208	0.208	0.000
10 2 2	0.197	0.197	0.000
12 0 0	0.192	0.193	0.001
14 0 0	0.168	0.166	0.002
14 6 0	0.153	0.153	0.000

ANNEX 3

d-spacings corresponding to *hkl* reflections from in synchrotron X-ray diffraction diagrams recorded on dry mats of V$_{\alpha\text{-naphthol}}$ crystals. The experimental *d*-spacings (d_{obs}) are compared with the values (d_{cal}) calculated from the parameters of the refined unit cell.

h k l	d_{obs} **(nm)**	d_{cal} **(nm)**	$\lvert d_{obs}-d_{cal} \rvert$ **(nm)**
2 0 0	1.1359	1.1359	0.0000
3 2 0	0.6301	0.6339	0.0.038
1 0 1	0.7382	0.7360	0.0022
1 1 1	0.7021	0.7019	0.0002
2 0 1	0.6433	0.6446	0.0013
2 1 1	0.6190	0.6193	0.0003

ANNEX 4

Conformational parameters of the isolated right and left-handed helices. Angles are expressed in °, puckering amplitudes in Å.

helix	Φ	Ψ	ω	τ	Q	ϕ	Θ
L_1	91	-134	-69	112.1	0.574	7.02	60
	111	-108	-73	113.0	0.585	6.99	296
L_2	104	-121	59	113.7	0.599	1.49	162
L_3	98	-121	138	113.1	0.596	5.77	305
R_1	110	-169	-55	113.5	0.597	4.80	301
R_2	109	-109	55	113.8	0.574	6.92	326
R_3	106	-109	133	113.6	0.595	9.14	307

ANNEX 5

Experimental (exp) and simulated diffracted intensities (L_1, L_2, L_3, R_1, R_2 and R_3 models). The spots were represented in according to their relative intensities: absent (-), weak (W), medium (M) and strong (S). The total number of spots in accordance between experimental and simulated diffracted intensities are given in the last line as agreement.

hkl	**exp**	L_1	L_2	L_3	R_1	R_2	R_3
100	-	-	-	-	-	-	-
110	W	W	M	M	W	M	M
200	M	W	M	-	M	M	M
210	W	W	W	-	W	-	-
220	M	M	-	-	M	M	W
300	-	W	W	-	no	W	-
310	-	W	-	M	W	W	-
320	-	-	-	-	W	-	-
330	S	S	S	M	S	S	S
400	S	S	S	S	S	S	S
410	-	M	M	M	M	-	-
420	S	S	S	M	S	S	S
430	-	M	M	M	M	M	M
440	S	S	M	M	M	M	M
500	-	M	W	M	-	W	-
510	-	M	-	-	-	W	-
520	-	-	-	-	M	M	M
530	M	S	M	M	S	S	S
540	W	W	W	W	-	W	M
550	-	M	M	M	S	S	-
600	S	M	M	M	M	M	M
610	W	M	M	M	W	-	S
620	M	S	M	M	M	S	S
630	W	-	M	W	W	W	M
640	W	M	M	W	no	W	M
650	-	M	M	-	M	-	M
700	-	-	-	-	W	-	-
710	W	W	-	M	M	M	M
720	-	W	-	-	M	M	M
730	W	M	M	M	-	-	M
740	W	M	M	M	-	M	W
agreement		13	15	14	14	12	14

ANNEX 6

Cell parameters, stress tensor components, final energy and density of initial (ini) and optimized (opt) helices in NVT molecular dinamics.

helix	*a* (nm)	*b* (nm)	*c* (nm)	α (°)	β (°)	γ (°)	XX (GPa)	YY (GPa)	ZZ (GPa)	YZ (GPa)	XZ (GPa)	XY (GPa)	energy (kcal/mol)	density (g/cm^3)
L_1 ini	23.3	23.3	31.6	90.0	90.0	90.0	2.47	2.73	3.60	0.11	-0.19	0.09	3084	1.47894
L_1 opt	24.7	23.8	34.	89.4	87.9	90.6	-0.00	-0.01	0.00	0.00	0.00	0.00	2178	1.23826
L_2 ini	23.3	23.3	31.6	90.0	90.0	90.0	4.07	3.59	1.32	-0.47	-0.42	-0.31	4837	1.47894
L_2 opt	25.3	22.8	33.25	90.8	92.1	89.8	-0.02	-0.04	-0.01	0.00	0.00	0.00	3611	1.31663
L_3 ini	23.3	23.3	31.6	90.0	90.0	90.0	3.50	3.35	3.18	-0.35	0.22	0.24	3701	1.47894
L_3 opt	25.1	23.0	35.6	96.4	91.4	87.0	-0.01	0.00	0.00	0.00	0.00	0.00	2493	1.23528
R_1 ini	23.3	23.3	31.6	90.0	90.0	90.0	3.50	3.92	2.52	-0.41	-0.21	0.33	3366	1.47894
R_1 opt	23.8	25.2	34.8	95.2	92.8	88.5	0.00	0.00	0.00	0.00	0.00	0.00	2246	1.21668
R_2 ini	23.3	23.3	31.6	90.0	90.0	90.0	2.21	2.22	3.54	-0.35	0.24	-0.24	3286	1.47894
R_2 opt	23.2	24.9	35.3	91.9	90.7	89.5	-0.01	-0.01	0.00	0.00	0.00	0.00	2377	1.24143
R_3 ini	23.3	23.3	31.6	90.0	90.0	90.0	3.23	2.61	3.62	-0.20	0.05	-0.21	3834	1.47894
R_3 opt	24.6	23.2	34.8	91.2	91.4	91.6	0.00	0.01	0.00	0.00	0.00	0.00	2456	1.27087

ANNEX 7

List of experimental normalized intensity averages measured from *hk*0 reflections in electron diffraction patterns recorded at room temperature on untilted V$_{\alpha\text{-naphthol}}$ single crystals.

h	*k*	intensity (a.u.)
1	1	52.05
2	0	1261.58
2	1	16.48
2	2	137.27
3	0	1.20
3	1	38.36
3	2	15.59
3	3	1000.00
4	0	3177.50
4	1	13.36
4	2	5019.37
4	3	8.76
4	4	2403.49
5	0	18.54
5	1	56.71
5	2	4.47
5	3	450.72
5	4	87.30
5	5	12.01
6	0	3222.32
6	1	194.78
6	2	292.59
6	3	85.70
6	4	70.13
6	5	10.88
6	6	81.05
7	0	3.17
7	1	77.79
7	2	22.62
7	3	36.00
7	4	12.22
7	5	23.46
7	6	7.35
7	7	57.97
8	0	130.36

8	1	10.68
8	2	40.24
8	3	11.48
8	4	68.49
8	5	23.60
8	6	87.68
8	7	5.07
8	8	15.36
9	0	1.17
9	1	7.46
9	2	33.66
9	3	36.81
9	4	4.27
9	5	11.43
9	6	25.10
9	7	8.08
9	8	10.18
9	9	13.09
10	0	33.30
10	1	8.32
10	2	70.93
10	3	9.59
10	4	22.20
10	5	25.41
10	6	5689.77
10	7	6.03
10	8	5.68
10	9	5.28
10	10	6.04
11	0	2.13
11	1	8.53
11	2	11.39
11	3	6.10
11	4	9.89
11	5	14.42
11	6	4.44
11	7	5.95
11	8	2.48
11	9	5618.99
11	10	3.60
11	11	5.93

ANNEX 8 - SCIENTIFIC PRODUCTION

Articles related to doctoral degree work

1. ***CARDOSO, M. B.*** ; Putaux, J.-L. ; Nishiyama, Y. ; Helbert, W. ; Hÿtch, M. ; Silveira, N.P.; Chanzy, H.
Single crystals of V-amylose complexed with α-naphthol.
Biomacromolecules, v.8, p. 1319-1326, 2007.

2. ***CARDOSO, M. B.*** ; Samios, D. ; Silveira, N.P. ; Rodembusch, F.S. ; Stefani, V.
ESIPT-exhibiting protein probes: a sensitive method for rice proteins detection during starch extraction.
Photochemical & Photobiological Sciences, v.6, p. 99-102, 2007.

3. ***CARDOSO, M. B.*** ; Putaux, J.-L. ; Samios, D. ; Silveira, N.P.
Influence of alkali concentration on the deproteinization and/or gelatinization of rice starch.
Carbohydrate Polymers. 2007, *in press*.

4. ***CARDOSO, M. B.*** ; Samios, D. ; Silveira, N.P.
Study of protein detection and ultrastructure of Brazilian rice starch during alkaline extraction.
Starch/Stärke, v. 58, p. 345-352, 2006.

Articles unrelated to doctoral degree work

1. Monteiro, K.M. ; Scapin, S.M.N. ; Navarro, M.V.A.S. ; Zanchin, N.I.T. ; ***CARDOSO, M.B.*** ; Silveira, N.P. ; Gonçalves, P.F.B. ; Stassen, H.K. ; Zaha, A. ; Ferrerira, H.B.
Self-assembly and structural characterization of Echinococcus granulosus antigen B recombinant subunit oligomers.
BBA. Proteins and Proteomics, v. 1774, p. 278-285, 2007.

2. Mertins, O. ; ***CARDOSO, M. B.*** ; Pohlmann, A.R. ; Silveira, N.P.
Structural evaluation of phospholipidic nanovesicles containing small amounts of chitosan.
Journal of Nanoscience and Nanotechnology, v. 6, p. 2425-2431, 2006.

Summarized works published in events

1. ***CARDOSO, M. B.*** ; Putaux, J.L. ; Nishiyama, Y. ; Mazeau, K. ; Chanzy, H. ; Helbert, W. ; Hytch, M. ; Samios, D. ; Silveira, N.P.
Crystal and molecular structure of 8-fold V-amylose complexed with α-naphthol. In: XIth International Macromolecular Colloquium / 6th International Symposium on Natural Polymers and Composites, 2007, Gramado.
Anais do Evento. 2007.

2. Heineck, M. ; ***CARDOSO, M. B.*** ; Giacomelli, F.C. ; Samios, D. ; Silveira, N.P.
Amylose behavior in alkaline and neutral ionic solutions: a combined static and dynamic light scattering study In: XIth International Macromolecular Colloquium / 6th International Symposium on Natural Polymers and Composites, 2007, Gramado.
Anais do Evento. 2007.

3. ***CARDOSO, M. B.*** ; Silveira, N.P. ; Putaux, J.-L.
Influence study of NaOH concentration in the alkaline extraction of rice starch. In: 9th European Training Course on Carbohydrates, 2006, Wageningen.
Anais do Evento. 2006.

4. ***CARDOSO, M. B.*** ; Jaeger, M.K. ; Heineck, M. ; Riegel, I.C. ; Samios, D. ; Silveira, N.P.
Aqueous solution behavior of native rice glutelin: a light scattering study. In: 41st International Symposium on Macromolecules, 2006, Rio de Janeiro.
Anais do Evento. 2006.

5. ***CARDOSO, M. B.*** ; Heineck, M. ; Samios, D. ; Carlini, C. ; Silveira, N.P.
Rice amylose full characterization by means of light scattering. In: 1st French-Brazilian Meeting on Polymers, 2005, Florianópolis.
Anais do Evento. 2005. C17.

6. Mertins, O. ; ***CARDOSO, M. B.*** ; Pohlmann, A.R. ; Silveira, N.P.
Chitosan applied to the structural modification of liposomes. In: 1st French-Brasilian Meeting on Polymers, 2005, Florianópolis.
Anais do Evento. 2005. A15.

7. Mertins, O. ; ***CARDOSO, M. B.*** ; Sebben, M. ; Pohlmann, A.R. ; Silveira, N.P.
Investigação através de SAXS das alterações estruturais em lipossomas provocadas pela adição de quitosana *(SAXS investigations of structural alterations in lipossomes provoked by chitosan addition)*. In: XV Reunião Anual de Usuários do Laboratório Nacional de Luz Síncrotron, 2005, Campinas.
Anais do Evento. 2005. v.1. p.35. (In Portuguese)

8. ***CARDOSO, M. B.*** ; Samios, D. ; Silveira, N.P.
Investigação da extração alcalina de amido de arroz através de SAXS *(Investigation of rice starch alkali extraction by SAXS).* In: XV Reunião Anual de Usuário do Laboratório Nacional de Luz Síncrotron, 2005, Campinas.
Anais do Evento. 2005. v.1. p.39. (In Portuguese)

9. Mertins, O. ; ***CARDOSO, M. B.*** ; Pohlmann, A.R. ; Silveira, N.P.
Natural polymers applied to the structural modification of phosphatidyl choline nanovesicles. In: Xth International Macromolecular Colloquium, 2005, Gramado.
Anais do Evento. 2005. v.1. p.22.

10. ***CARDOSO, M. B.*** ; Samios, D. ; Silveira, N.P.
Rice starch extraction and characterization: optimizing some procedures. In: Xth International Macromolecular Colloquium, 2005, Gramado.
Anais do Evento. 2005. v.1. p.21.